UNIVERSITÀ DEGLI STUDI DI PADOVA
DEPARTMENT OF INDUSTRIAL ENGINEERING

Master's Degree in Electrical Energy Engineering

Multiparametric optimization
for DTT NBI beam source

Supervisor:

Prof. Sonato Piergiorgio

Advisor:

Doct. Eng. Agostinetti Piero
(Consorzio RFX)

Student:

Veronese Fabio

Mat. 1171760

10 September 2019

Academic Year 2018/2019

Contents

Summary

The Divertor Test Tokamak (DTT) will be new experimental facility, expected to be built in Italy in the near future, and part of a greater research plan envisioned by EFDA in 2012, that devised a Roadmap in 8 steps towards the generation of electrical power by a Demonstration Fusion Power Plant (DEMO) by 2050. This one in particular aims to cover with on-field experience the gap in Plasma Facing Components knowledge during the complex extrapolation process from proof-of-principle devices to actual full-power experiments like ITER and future DEMO-like reactors, that cannot simply be filled with numerical simulations. Its main objectives are:

- Development of Plasma Facing Components (PFCs) able to cope with very large power fluxes $\left(\approx 5 \div 10 \frac{MW}{m^2}\right)$;
- Selection of the divertor geometry and of the magnetic flux expansion to reduce the normal heat flux on the target, i.e. by distributing the heat over a larger surface;
- Removal of plasma energy before it reaches the target via impurity radiation by increasing edge plasma density and injecting impurities in the SOL region, as to decrease the fraction of the heating power that impinges on the divertor, up to a level compatible with the materials technology;
- Recycling and increase of density lowering the temperature close to the target, with consequent detachment (the temperature drops below that required for ionization; therefore, the particles are neutralized and there is no direct plasma flux or power to the divertor targets).

This DTT tokamak will need to be flexible enough in its working conditions to study, test and propose a solution then to be used directly where needed; consequently, it must be able to realize scaled experiments integrating most of the possible aspects of the DEMO power and particle exhaust. In order to obtain this ambitious objective, auxiliary heating from NBI has been estimated in the order of 10 to 15 MW of power; to that end, two injectors of 5 to 8 MW each have been proposed, with an extracted total current of about 40 A of D^- using a 400 keV electrostatic acceleration system. These systems, albeit simple in the concept of using grids to accelerate particles,

present a manifold of complications, non-linearities and critical issues that call for accurate simulation in each physical aspect that is encompassed within:

- Particle beam optics
- Electrostatics
- Magnetostatics
- Physical reactions (elastic, charge-exchange, etc. collisions)
- Heat transfer (from ill-focused impinging particles)
- Solid mechanics (deformations due to temperature variation)

Each one of these aspects contributes to another to some degree, hence the importance of accurate evaluation. At this moment, the commercial Finite Element Method (FEM) multi-physics simulation code COMSOL® has been used to simulate the thermal behavior of the electrostatic accelerator of the particle injector for DTT. This thesis work focuses first on verification through multi-physics simulations in the COMSOL environment and data post-processing using MATLAB® code, if preexisting designs for the DTT beam source will be enough to satisfy various project criteria, similar to those in ITER and in pre-conceptual works for DEMO. The criteria considered here regard aspects of beam optics, thermo-mechanical resistance and surface temperature, following the choices made previously by the DTT team and other researchers mostly on term of grid geometry, materials, extracted power, gas background density, and such. To do this, during this thesis framework a self-contained multi-physics model has been created, able to evaluate localized thermal heat loads due to beam losses and electron co-extraction and to model the cooling channels dedicated to dissipate the deposited power on the acceleration grids, all in a single code. Following, fully aware with the problems regarding the current design, the following chapter is dedicated to the functional optimization of the project of the accelerator and its cooling channels. Some novel concepts and configuration tweaks have been investigated and then verified their performances with respect to the actual setup, in order to improve its operativity.

Riassunto

Il Divertor Test Tokamak (DTT) sarà un nuovo centro sperimentale, previsto di essere costruito in Italia tra pochi anni, e parte di un piano di ricerca più grande programmato dall'EFDA nel 2012, che ha immaginato una Mappa in 8 passi verso la generazione di potenza elettrica da un Demonstration Fusion Power Plant (DEMO) entro il 2050. Questa struttura in particolare mira a coprire con esperienza sul campo una lacuna sulla conoscenza dei Plasma Facing Components durante il complesso processo di estrapolazione da macchine sperimentali ad esperimenti a piena potenza come ITER o futuri reattori di tipo DEMO, non colmabile semplicemente con sufficienti simulazioni numeriche. I suoi obiettivi principali sono:

- Sviluppo di Plasma Facing Components (PFCs) in grado di sopportare flussi di potenza molto grandi $\left(\approx 5 \div 10\, \frac{MW}{m^2}\right)$;
- Selezione della geometria di divertore e dell'espansione di flusso magnetico per ridurre il flusso normale sul target, per esempio ridistribuendo il calore su una superficie più larga;
- Rimozione dell'energia di plasma prima che raggiunga il target tramite radiazioni da impurità aumentando la densità di plasma di confine e iniettando impurità nella regione di SOL, per ridurre la frazione di potenza riscaldante che si deposita sul divertore, almeno fino ad un livello compatibile con la tecnologia dei materiali;
- Riciclo ed aumento della densità con abbassamento della temperatura vicino ai punti di contatto, con conseguente "distacco" (la temperatura scende al di sotto quella richiesta per la ionizzazione; perciò la particelle si neutralizzano e non c'è flusso diretto di plasma o potenza sui bersagli del divertore).

Questo DTT tokamak dovrà possedere una certa flessibilità nelle condizioni di lavoro per studiare, testare e proporre una soluzione da poter usare poi ovunque necessario; di conseguenza, deve essere in grado di realizzare esperimenti in scala integrando il maggior numero possibile degli aspetti propri delle potenze in gioco e scarico particelle (simili a DEMO). Per ottenere questo obiettivo ambizioso, è stato stimata la necessità di riscaldamenti ausiliari da iniettori di neutri (NBI) nell'ordine di 10, 15 MW di potenza circa; a tal fine, due iniettori da 5 a 8 MW ognuno sono stati

proposti, con una corrente estratta totale di circa 40 A di D^- usando un sistema di accelerazione elettrostatica di 400 keV. Questi sistemi, seppur semplici nel concetto di usare griglie cariche per accelerare particelle, presentano un grande numero di complessità, non linearità e problemi critici che richiedono simulazioni accurate in ogni aspetto fisico che le interessa:

- Ottica del fascio di particelle
- Elettrostatica
- Magnetostatica
- Reazioni di tipo fisico (elastiche, scambio carica, ecc., collisioni)
- Scambio di calore (da particelle mal focalizzate in collisione)
- Meccanica dei solidi (deformazioni dovute alla variazione di temperatura)

Ognuno di questi aspetti contribuisce all'altro ad un certo livello, da cui l'importanza di una simulazione accurata. In questo periodo, il codice commerciale agli elementi finiti (FEM) multifisico COMSOL® è stato usato per simulare il comportamento termico dell'acceleratore elettrostatico dell'iniettore di neutri di DTT. Questo lavoro di tesi si focalizza in primo luogo sulla verifica tramite simulazioni multifisiche in ambiente COMSOL e post-processing utilizzando il codice MATLAB®, se schemi preesistenti per la sorgente di fascio di DTT siano sufficienti a soddisfare alcuni vari criteri di progetto, simili a quelli di ITER o di lavori pre-concettuali per DEMO. I criteri qui considerati riguardano aspetti di ottica del fascio, resistenza termomeccanica e temperatura superficiale, seguendo scelte fatte in passato dal team di DTT ed altri ricercatori perlopiù in termini di geometria di griglia, materiali, potenza estratta, densità del gas di sottofondo, e simili. Per portare a termine il lavoro, durante il periodo di questa tesi è stato creato un modello auto-contenuto multifisico, capace di valutare carichi termici localizzati dovuti a perdite di fascio e co-estrazione di elettroni ed anche modellizzare i canali di raffreddamento dedicati a dissipare la potenza depositata sulle griglie d'accelerazione, tutto in un unico codice. In seguito, conoscendo nel dettaglio i problemi dei design correnti, il capitolo seguente è dedicato alla ottimizzazione funzionale del progetto dell'acceleratore e dei suoi canali di raffreddamento. Alcuni concetti inediti e modifiche di configurazione sono state investigate e poi verificate in performance rispetto alle disposizioni attuali, in modo da migliorarne l'operatività.

Chapter 1

Fusion energy

SUMMARY - Fusion energy is a important topic in our day and age, and is often hailed as one of the possible main way of production of renewable electrical energy in humanity near future. This chapter deals with a general overlook on the principles behind magnetically confined thermonuclear fusion, as well as details on key experiments as ITER.

1.1 Introduction

Never like at this point and age in the history of humanity, there has been such a need for power: the power to shape mountains with bores, travel to space, operate a pump, go to work in an electric train after turning off the electric heater back at home, charging the latest battery-eating phone; as humans grow, the demand for energy naturally grows with them. To satisfy it though we are disposed to destroy the very planet that host the small lives that we seek to improve, waging both literal and economical wars against anything that does not goes our way. This is the basis of the great "energy problem", that the scientific community set to resolve before long, and with one of the possibilities being to inquire further into the use of fusion power plants as a definitive solution to the issue.
In these next paragraphs a little summary of the expected pros and cons will be listed, trying to point out the reasons for this choice and the know-how that will have to be developed to bring to fruition what could be mankind greatest accomplishment of this century, a future controlled thermonuclear fusion power plant; secondly referring explicitly to one of the greatest international projects regarding techno-scientific progress in said context: the ITER (International Thermonuclear Experimental Reactor) project.
This thesis is the result of a six-month stage at Consorzio RFX, one of the most important contributors to the worldwide scientific effort on fusion and home to the MITICA and SPIDER experiments, as well as to the greatest RFP tokamak in the world.

1.2 Energy outlook

As of today, electrical power production still greatly relies on generation by traditional thermal plants burning fossil fuels such as coal, natural gas, oil and petroleum distillates, releasing in the atmosphere large amounts of carbon dioxide, nitrous and sulfurous oxides, extremely dangerous to the environment if not recaptured (e.g. coal combustion generates anhydrides that by reacting with water are the main responsible of the *acid rain* phenomenon). A number of other more politics-centered problematics ride on how energy is generated and distributed, such as delicate geopolitical equilibria or the dependence from foreign and unstable regions for fuel supply.
Moreover, these conventional energy sources are not inesaurible: estimations projects that, at the current rate of production and use, reserves are expected to last up to 132 years for coal, 50.9 for natural gas and 50.0 for oil [1]. Even supposing to have reserves for another 200 years, the problem would be just slightly postponed onto the next generations, rushing them to find a solution in our stead. This without even considering that the global energy request is constantly increasing by the year.
"Alternatives" are plenty to the fossil fuels for power production: fission plants, hydroelectric, photovoltaic, eolic, geothermic, and a lot more; nevertheless, there is an important distinction to be made between alternative and integrative energy sources: very often people talking about alternative energy sources include all the aforementioned. That, is a mistake: as a matter of fact, the only real alternative in the list is the nuclear fission plant, the others being mere integratives. The distinction is as simple as significant: alternative sources are potentially up to the challenge of satisfying the global need of energy, while the others are not, by sheer difference in TWh production. A reliable alternative could then be fission power plants: theoretically, building enough of these high-tech reactors (especially latest-gen versions) to cover the needs of the entire planet would be possible. Some countries are already producing enough (and more) than their internal energy request by main fission power plants use, but there are many a reason (since their first appearance) as to why governments are looking for other solutions:

1. Fission plants need radioactive "fuels" such as ^{238}U, ^{239}Pu, ^{233}U, with elevate contamination hazard, not easily obtainable and not equally distributed along the world.

2. These plants produce as byproducts radioactive elements such as ^{141}Ba and ^{137}Cs, the second being very dangerous because soluble in water. Moreover, the problem of radioactive waste disposal remains, again with high contamination hazard and logistic problems: as an example, the ^{239}Pu has a halving time of 24200 years and needs a storage time of about 300000 years.

3. Recent incidents (the Fukushima incident in Japan, or the forced shutdown of many plants for safety reasons in France) or more historic ones (Chernobyl)

showed to the world how problematic these plants can be in case of faults, natural disasters or human mistakes.

4. The problem of the finite availability of ^{235}U still stands.

As a focus on the last point made, a several-hundred years' worth of ^{235}U has been esteemed [2] to be available in nature, and as a plus last-gen plants can use ^{233}U and ^{239}Pu, which are in an even larger availability. However, the other three points are reason enough to make this power source a constant threat. If dividing nuclei has a lot of issues, it is advisable to try to start from the bottom, by fusing light nuclei together: what happens every day in the Sun.

1.3 Nuclear fusion

The fundamental concept of nuclear fusion is to collide two (or more) light nuclei, obtaining a new nucleus with a total mass that is lower than the sum of the starting nuclei. This mass difference is transformed into energy flowing out of the system in the form of radiation or particle kinetic energy, as expected by the well-known Einstein's equation $E = \Delta mc^2$. This happens because, for nuclei with mass number $A < 56$, the binding energy defined as:

$$B = \left(N_{m_n} + Z_{m_z} - m(N,Z)\right) c^2 \tag{1.1}$$

where N is the number of neutrons and Z the number of protons, increases with the number of nucleons. It is then possible to convert such energy through alternators in electric energy to power up transmission, distribution lines and utencies.
From a physical point of view, the phenomenon is very well established and simply verified by observing what happens every day in the Sun and in the other stars in the Universe; from a technological point of view though the circumstances of obtaining fusion are obviously way more complex. The principal nuclear reactions that are being contemplated as solutions in a future thermonuclear reactor involve some of the lightest particles in the universe, namely Deuterium (D), Tritium (T) (both hydrogen isotopes) and helium-3. These are [2]:

$$\begin{aligned} D + T &\longrightarrow {}^4He\,(3.5\,MeV) + n\,(14.1\,MeV) \\ D + D &\longrightarrow T\,(1.01\,MeV) + p\,(3.02\,MeV) \\ D + D &\longrightarrow {}^3He\,(0.82\,MeV) + n\,(2.45\,MeV) \\ D + {}^3He &\longrightarrow {}^4He\,(3.6\,MeV) + p\,(14.7\,MeV) \end{aligned} \tag{1.2}$$

The values in brackets indicate the kinetic energy associated with each particle produces by the reaction; and each one is characterized by its own "probability", or cross-section, expressed in m^2: it carries the meaning of an area surrounding the target particle such as if the incident particle traverses it, the reaction is initiated.

Out of all reactions, the most desirable one would be a deuterium-only fusion: this because the availability would be virtually infinite fuel-wise, since deuterium is easily obtained from heavy water, that is present in fixed quantity in seawater (about 1 part out of 6000). The helium-3 reaction instead has the highest net energy gain, and also all of its byproducts are electrically charged, making them possible to confine longer inside the bulk plasma and help maintain the fusion temperature. In the end though, cross-section is the actual decisive criterion that need to be considered: figure 1.1 reports the experimental cross-section data for fusion reaction in function of the incident particle, and it is easy to see how the $D-T$ reaction dominates the other two in the relevant range of energies. The difference is such that at this moment in history the deuterium-tritium reaction is the only one being researched for power production purposes. This reaction though does not come without drawbacks:

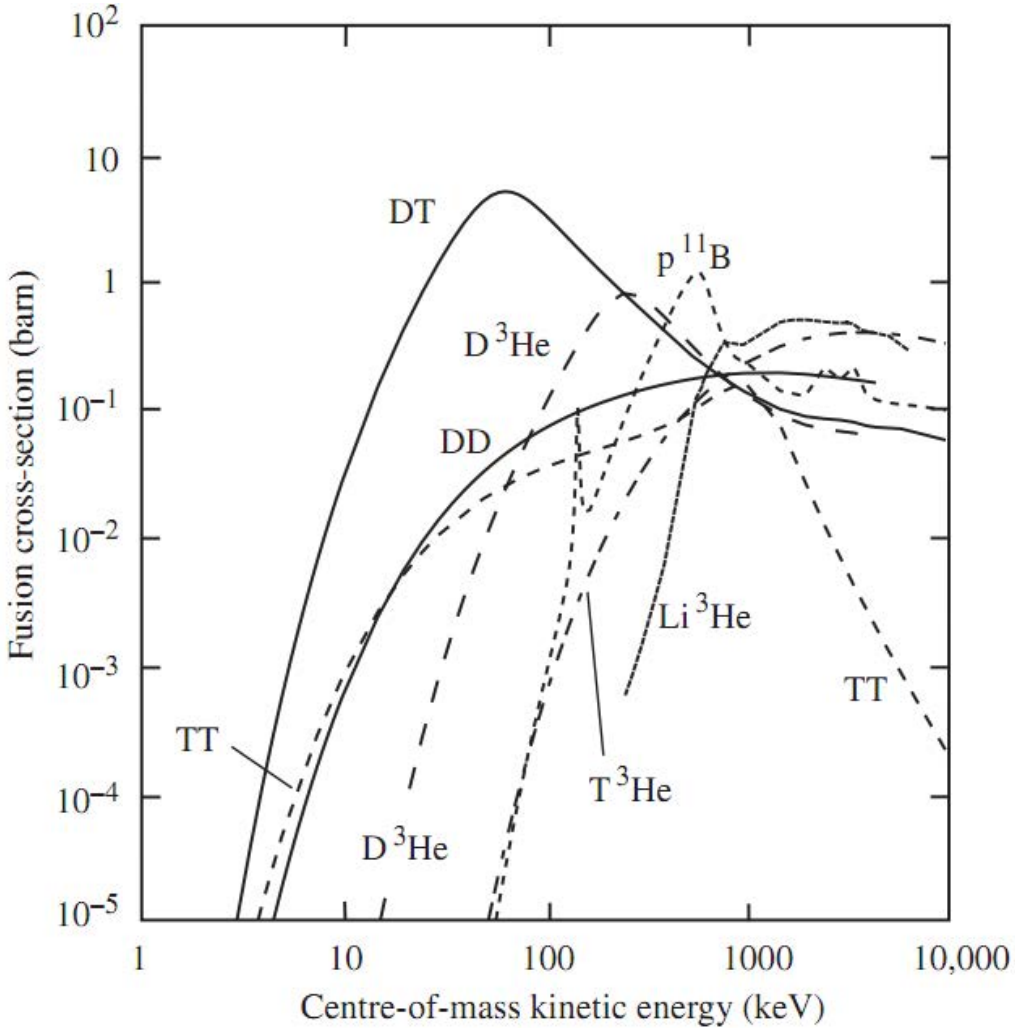

Figure 1.1: Cross-section of some typical nuclear reactions as a function of the energy of the incident particle. One barn equals 10^{-28} m^2. [2]

tritium is naturally radioactive, with a half-life of 12.3 years; this means that it is not present in nature, and must be produced ad hoc. The most common reactions to produce tritium involve Lithium atoms and fast neutrons:

$$\begin{aligned} {}^6Li + n &\longrightarrow He + T + 4.8\,MeV \\ {}^7Li + n &\longrightarrow He + T - 2.5\,MeV \end{aligned} \tag{1.3}$$

One reaction is exothermic, hence desirable in a fusion plasma; the problem is that the fraction of ${}^6Li$ available is extremely smaller than the other option. The actual design choice for use into fusion reactors is to produce tritium through these reactions directly inside the vacuum vessel, by coating particular zones with lithium, called Breeding Blankets, and exploiting the fast neutrals generated by the fusion reactions. This shifts the problem of availability from tritium to lithium, that can boast a relatively high diffusion over Earth's upper crust.

1.4 Plasma definition

Given the range of energies (and hence temperatures) in which fusion cross-sections are meaningful (easily in the 10 keV range), it is easy to see how they can happen only between elements in plasma condition. Plasma, usually hailed as the fourth state of matter, is defined as a quasi-neutral ionized gas characterized by high temperatures, electric conductivity and displaying collective behavior. There are a number of criteria that distinguish a simple ionized gas from a fully developed plasma:

- One of the criteria involves the conductivity and hence the ability to shield external electric fields. In plasma, positive and negative charges are free to move independently, and over a certain spatial length charge imbalance due to fields disappears. The parameter that gives the order of magnitude of said distance is called Debye length:

$$\lambda_D = \sqrt{\frac{\epsilon_0 T_e}{n_e e^2}} \tag{1.4}$$

  where T_e and n_e are the electron temperature and density. This means that in order to have plasma, the macroscopic length of its main dimension L must verify that $L \gg \lambda_D$: with this condition it is ensured that there is no macroscopic charge concentration, making the ionic and electronic densities equal in average.

- The number of particles contained in a sphere of radius λ_D must be far greater than one:

$$N_D = \frac{4}{3}\pi\lambda_D^3 n \gg 1 \tag{1.5}$$

  This ensures that the particles are numerous enough to make averages and integral quantities meaningful, and describable with distribution functions.

- Another criterion regards the role of collective effects compared to internal collisions. To describe this ratio, it is possible to use the plasma frequency ω_p, indicating the time scale for the plasma to shield inhomogeneities, and the collision frequency ν_c indicating the average time between collisions for particles. The ratio of these two quantities ω_p/ν_c is thus an index of how much collisions have influence in the particle behavior. In a plasma, this parameter has to be far greater than one, indicating a prevalence of ranged collective effects on local collisionality. What it also entails is the need when describing the system of considering not only conventional fluid dynamics, but also electromagnetism: magnetohydrodynamics (MHD).

1.5 Plasma confinement

To create the right conditions for fusion, particles must be confined close to each other: plasma can be confined gravitationally, magnetically or inertially.
Gravitational confinement is the phenomenon that is proper of stars: particles are held extremely close to each other by the centripetal pull of gravity, and the fusion reaction that results generates an opposing force as to compensate and reach equilibrium. Given the scale at which gravitational effects become relevant, it is obviously impractical to reproduce said condition on Earth.
Experiment on inertial confinement for fusion relies on extreme heating and compression of a target pellet of deuterium and tritium by high power laser beams. There is interest on the research field, but production of energy from said source would result impractical, due to the extremely pulsed nature of the fusion reaction.
The main focus is then on magnetic confinement: its concept is based on the behavior of charged particles in electromagnetic fields, in particular the Lorentz force.

$$\mathbf{F} = q(\mathbf{E} + \mathbf{v} \times \mathbf{B}) \tag{1.6}$$

Solving the motion differential equation yields a gyrating motion around the magnetic field lines, at a distance and a frequency:

$$\begin{aligned} r_L &= \frac{m|v_\perp|}{q|B|} \quad \textit{Larmor radius} \\ \omega_c &= \frac{q|B|}{m} \quad \textit{cyclotron frequency} \end{aligned} \tag{1.7}$$

where $|v_\perp|$ is the module of the component of the velocity perpendicular to the $\mathbf{B}$ vector. The best and easiest topological choice to confine the plasma is to close the magnetic field lines on themselves in a toroidal shape. Due to the manifestation of destabilizing forces, mainly related to the toroidal form and MHD instabilities, it is necessary to twist the magnetic field lines, by adding a poloidal component to the already present toroidal confining one. Three possible methods to obtain the

needed field configuration have been developed: the Reversed-Field Pinch (RFP), the Stellarator and the Tokamak. All of them have notable pros and cons, but the most researched and the most diffused technology at the moment is indeed the Tokamak, for its relative simplicity and versatility; as such a brief explanation for it will be reported.

1.6 The Tokamak configuration

The tokamak configuration has been invented in 1952, named after a Russian acronym for *toroidal'naya kamera s magnitnymi katushkami*, "toroidal chamber with magnetic coils". Since then it has been the most promising axisymmetric toroidal configuration for high temperature plasma confinement. The system is constituted by:

- The toroidal magnetic coils, consisting in a elevated number of radially symmetrical "D"-shaped coils, usually superconductive, due to the extremely high currents needed to maintain the desired magnetic fields. Their shape is accurately optimized to resist electromechanical stresses and provide large space to the fusion plasma within. Magnetically they are the main source of the confinement field, compensating part of the outward kinetic pressure of the traveling particles.

- The poloidal magnetic coils, divided into central solenoid and position control coils; and similarly to the toroidal ones they can be superconductive. The central solenoid concatenates the whole vacuum vessel, behaving as the primary of a transformer with respect to the ionized gas within as the secondary, hence able to transfer energy through ohmic dissipation; the other poloidal coils run around the tokamak, and they provide the field necessary to maintain shape and position of the plasma volume.

- The Heating and Current Drive auxiliary systems, indicating a set of devices dedicated to helping maintain the power balance inside the plasma volume and thus the fusion conditions by injecting power through various methods, for example Neutral Beam Injection of Radio-Frequency Antennas, and also helping to drive the overall plasma current. The neutral beam injection techniques will be treated in detail in chapter 2.

- Radial saddle coils, mainly dedicated to fine-tuned control of MHD instabilities.

- Power supply and control systems, as well as the vacuum and cooling subsystems, and everything else dedicated to the accurate operation of the tokamak.

Before a discharge the central coil is charged to its nominal current and shorted, the vacuum vessel is filled with the initial charge of plasma gas and the position control coils are powered, ready to contain the plasma that is about to form. At the

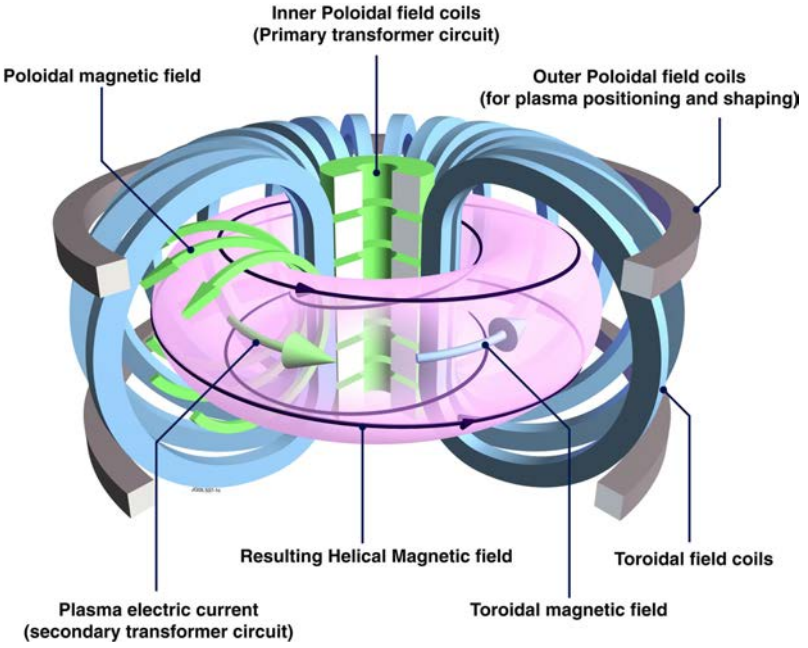

Figure 1.2: Scheme of the tokamak configuration and positioning of the magnetic system.

start of the pulse operation, a massive Inductively-Coupled discharge in the gas is provoked by the flux swing generated by the switching of the main central coil on a discharge resistor, in a great equivalent L/R circuit fashion. The discharge is then maintained through the help of additive heating systems, for the whole so-called flat-top phase. At the end of the available flux swing, it is necessary to stop the discharge in a controlled way, to avoid the quenching of the plasma current, that could cause extreme electromagnetic stresses on the vessel components.
The plasma is contained within the volume intercepted by toroidally closed magnetic flux lines, but all of those particles that migrate outside of the confinement (because of collisions, neutralization, diffusion mechanisms or even the fusion reaction itself) are bound to intercept the walls of the vessel, potentially causing great thermal loads in small area sections and damage. To avoid this, the walls are actively cooled, for those neutral particles that can no longer be confined (e.g. neutrons from the fusion reaction), whereas the outer envelope surface of the plasma volume that encloses all of the closed flux lines (called Last Closed Flux Surface) is modified in shape, in order to direct at least the charged stray particles away from the burning plasma and into a part dedicated to thermalization and dispersion of the particle energy. This component presents itself in both *limiter* and *divertor* configuration, each with its pros and cons, and illustrated in figure 1.3: most of the actual designs makes use of a divertor, due to its ability to dissipate higher thermal fluxes and its greater distance from the burning plasma, diminishing the impurities within. The component itself is very critical to a good operation of the tokamak, but its behavior

is strongly dependent on the plasma and its dynamics, that are quite hard to model in a simulation. This is one of the reasons behind the need of a dedicated facility to the accurate study of this delicate component and plasma-wall interactions in reactor-like environments, without risking to lose years of research because of a wrong extrapolation of a low-power design: that facility, DTT, and its auxiliary heating systems are the main scopes of this thesis, and will be explored in detail in chapter 3.

As demonstrated through the Lawson criterion, in which a simple zero-dimensional

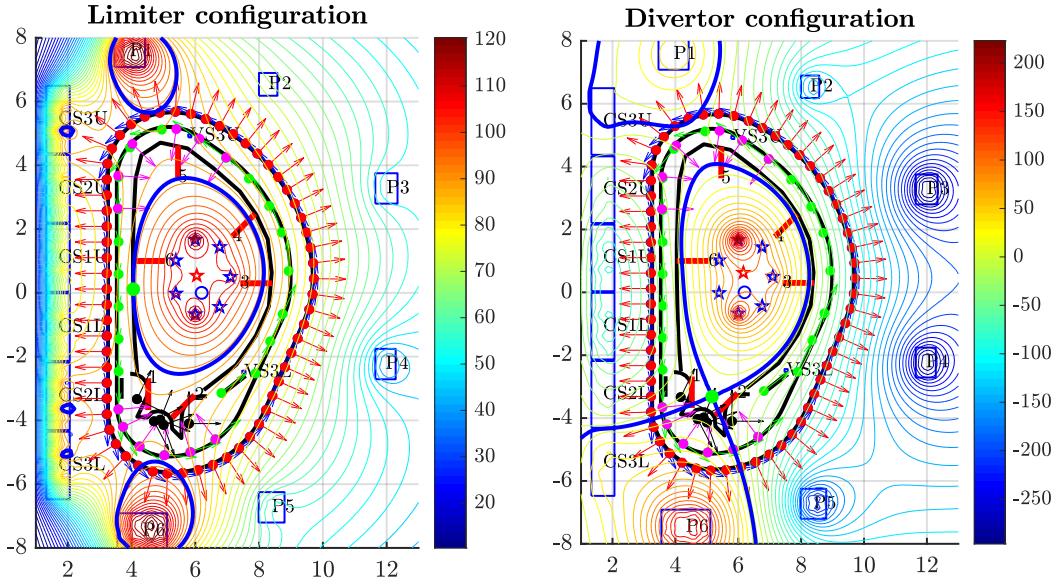

Figure 1.3: Results of a simulation on a poloidal section of ITER. Evident for the two configurations are the magnetic flux lines, as well as the Last Closed Flux Surface in blue.

power balance is carried between power intake of the reactor and various losses from plasma, it can be shown that in order to obtain a self-sustaining reaction, some key parameters such as the particle density n, the average confinement time τ_E and the plasma temperature T can be combined to form a parameter called *triple product* $n\tau_E T$. This value must be met by the tokamak specifics to be able to reach the so-called *break-even* condition, in which the power generated by the fusion reaction is equal to the power lost and the auxiliary heating used to maintain optimal fusion conditions. In particular the most desired type of power balance, called *ignition*, and defined as the condition in which the heating of the plasma due to the fusion reaction itself is sufficient to cover the other power losses without the need of auxiliary heating can be obtained if the triple product verifies the disequation:

$$n\tau_E T \ \geq 5 \cdot 10^2 1[\mathrm{m}^{-3}\mathrm{keV\ s}] \tag{1.8}$$

As plasma confinement technologies progress, it is possible to reach higher confinement time scales, and consequently increasing density and temperature; in over fifty years the steps made in that sense have been giant leaps towards the objective of reactor-like and ignition power gain, as can be seen in figure 1.4. The next important step in this path (and dot in the figure) will be the reaching of the break-even condition in the largest international scientific effort in the field of thermonuclear fusion, ITER.

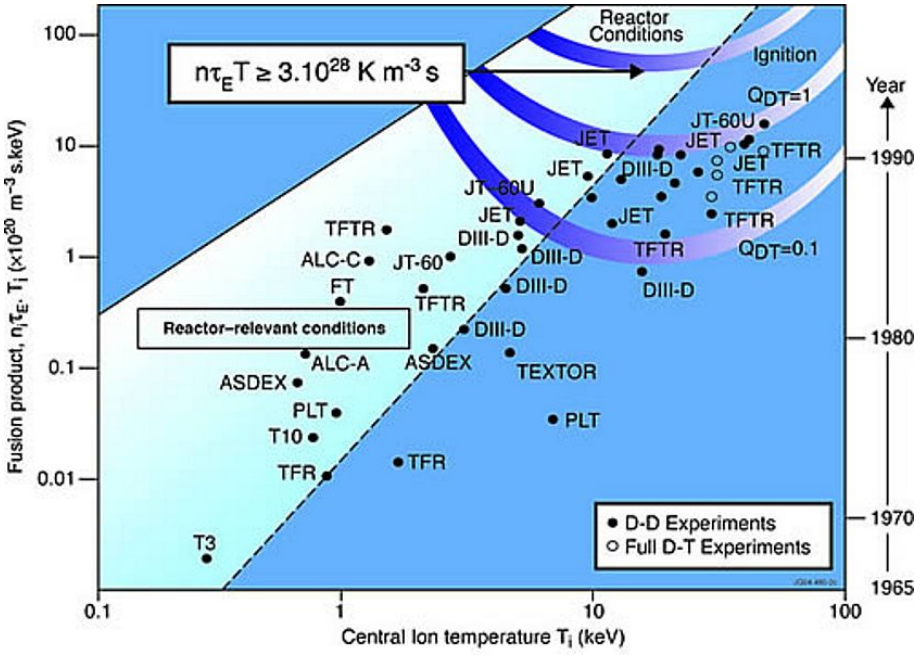

Figure 1.4: History of experimental tokamaks' triple products, reported as a function of the core temperature. It can be seen how the Lawson curves present a minimum at around $T \approx 15$ keV.

1.7 ITER

The International Thermonuclear Experimental Reactor (ITER) is the focus of all of the international scientific community effort revolving around nuclear fusion, involving the European Union, United States, China, India, Japan, South Korea, Russia, etc. for a total of 35 countries that are working together towards the realization of the world's largest experiment on fusion. The building site of the experimental reactor has been chosen to be Cadarache, in France; it will be designed to prove the feasibility of reactor-like power gain (to generate over 10 times the auxiliary power used) and maintain the fusion reaction for long periods of time. A glance to the main parameters of ITER can be found in table 1.1, and the cutaway in figure 1.5 shows the inherent inner complexity of such a machine. With its considerable size (about ten times the plasma volume of the largest device in operation) and overall power, diagnostic

ITER parameters	Unit	Value
Power by fusion	[MW]	500
Gain factor Q		≥ 10
Pulse duration	[s]	3600
Plasma type		$D-T$
Maximum plasma radius	[m]	6.2
Minimum plasma radius	[m]	2.0
Plasma current	[MA]	15
Toroidal magnetic field	[T]	5.3
Auxiliary heating:		
- Neutral Injectors	[MW]	33
- RF Antennas	[MW]	40
Plasma volume	[m^3]	830
Device height	[m]	26
Device diameter	[m]	29

Table 1.1: Iter experimental reactor main properties. [2].

availability and operating range, ITER will also permit the investigation of an array of new physical regimes and technological issues that up to now were impossible to explore, due the reduced dimensions: for the first time, there will be tests on the production of tritium directly during the discharge through in-vessel breeding blankets, as well as important data on the divertor component. These finds will be key in developing the next step of the research towards the demonstration of the technological and economic feasibility of a nuclear fusion power plant, what is known as the DEMO project.

1.8 DEMO

The DEMO (DEMOnstration Fusion Power Plant) is a term for a class of proposed thermonuclear fusion power plants, intended to follow the trail of the ITER experimental reactor. The objectives of DEMO are usually intended to lie somewhere those of ITER (purely experimental) and a "first of a kind" commercial plant. In fact, while in ITER the goal is to demonstrate the possibility to obtain a plasma able to sustain the fusion nuclear reaction on acceptable level of confinement and power exhaust, in DEMO the main objective is to prove the industrial feasibility of fusion by exploring the electricity production from the fusion reaction, the safety aspects and the tritium self-sufficiency. Consequently, in DEMO the issues related to efficiency and reliability, availability, maintainability and inspectability (RAMI) are among the most important drivers for the design. In fact, the cost of the electricity

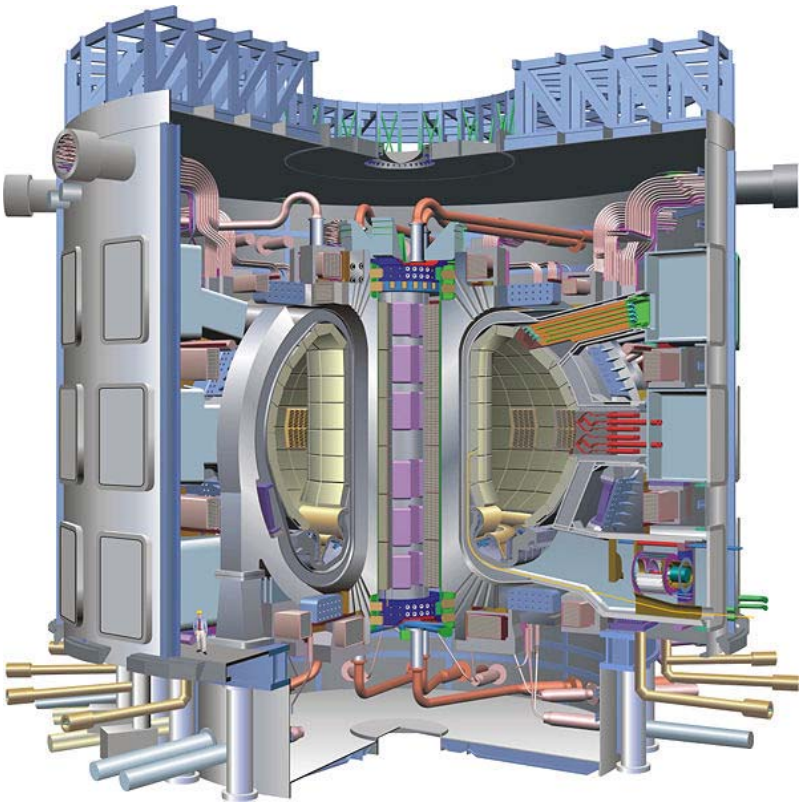

Figure 1.5: 3D cutaway of ITER configuration. The size can be perceived by the human figure in the picture.

produced by this power plant will strongly depend on these issues, and also on how the know-how on component production will evolve. As of now, the whole project is still in an early pre-conceptual R&D phase, due to the lack of experiments and data on the full-scale fusion process and, in the specific, on the lack of experimentation on the 1 MeV particle acceleration range and knowledge on reactor-like divertors; ITER and the PRIMA facility test-bed (currently in assembly process), where the MITICA (a prototype for ITER NBI) will be tested, as well as the future DTT facility will prove invaluable source of data to define the final blueprints of the DEMO project. Following in ITER footsteps, one of the main tools to heat the plasma up to fusion conditions in DEMO will be several Neutral Beam Injectors (NBI), for which a conceptual design has already been carried out by Consorzio RFX [3], featuring many differences and possible improvements (based on present or soon-to-be technologies) aimed to improve the efficiency and RAMI, which will become key aspects for future industrial diffusion.

Chapter 2

Neutral beam heating overview

SUMMARY - Neutral beam heating is considered nowadays the most important method to supply additional power in many fusion experiments around the world. The concept is straightforward: neutral atoms penetrate through the confining magnetic field and are ionized in the plasma via Coulomb collisions with electron and ions. The fast ions generated in this way are then confined by the magnetic field as well. If their kinetic energy is large compared with the plasma temperature, they deliver their energy to ions and electrons by collisions, heating up the plasma. Fast neutral atom beams are generated via charge exchange neutralization of ion beams. This chapter sums up the physical basis of generation and neutralization of an ion beam, with a focus on the losses mechanisms.

2.1 Introduction

High power neutral beams for heating high temperature plasma are a requirement for realization of controlled thermonuclear fusion as an energy source, leading the group of so-called Heating and Current Drive (H&CD) systems. These devices will be key in sustaining the plasma discharge in the energy gap between the *fast-rise* phase (the start of a discharge in Tokamak configuration) and the *ignition* phase (self-sustaining fusion reaction). The sources used for such Neutral Beam Injection (NBI) systems are characterized by high acceleration voltages (several hundred keV) and high current (several tens of A), and consequently by high power (tens of MW). The term ion beam source in this thesis indicates the assembly of:

1. A plasma source, where the plasma is generated.
2. An extractor, where the ions formed in the plasma are extracted by means of an applied electric potential, forming an ion beam.
3. An accelerator, where the ion beam is accelerated to the maximum potential.

The injected beam energy E_{NBI} with which choose the acceleration voltages is determined by the expected penetration depth in the target plasma. Beam energy has increased from about 20 keV for the first experiments on injection into magnetically confined plasmas in 1974 up to about 400 keV at present, as the target plasma size has become larger: future fusion reactors will need NBIs of energy up to 2 MeV. The neutral particle is then created by charge-exchange (CX) conversion from an ion beam; at higher energies, above 100 keV per nucleon, the neutralization efficiency for positive ions decreases drastically while maintaining at around 60% for negative ions. Thus large scale, positive ion sources were developed in the 70s and 80s when the required beam energy was below 80 keV per nucleon, whereas nowadays negative ion source development for the high energy NBI system aimed at reactor-sized fusion machines is in full development.
There are several circumstances that make the principle of neutral injection work [4]:

- The CX cross sections are just adequate for an efficient neutralization (at least for beam energies of several tens of keV, typical for ignited fusion plasma).
- The size of the ionization cross sections in the plasma are just adequate to trap the neutral beam efficiently (at least for medium size plasmas).
- The collision rates in the plasma are just adequate to slow the fast ions down and distribute the resulting heat between plasma ions and electrons.

However, the characteristics of neutralization and trapping also define the limitations of neutral beam heating: following short descriptions of the theory backgrounds will be given.
The interaction of fast neutral atoms with a plasma as they cross the Vacuum Vessel comprises the following physical processes [5], the last three of which occur simultaneously:

- Ionization of the fast neutral atoms by elastic or Coulomb collisions with plasma electrons and ions;
- The drift motion of the fast ions in the magnetic field;
- The collisions of fast ions with plasma ions and electrons, giving rise to slowing-down and scattering;
- The charge exchange collisions of the fast ions with background neutral atoms.

All of these processes are related to certain losses: for example, due to the neutral beam not entirely ionized (*shine-through*), or the fast ion orbits intersecting the Scrape-Off Layer (SOL) before the complete thermalization of the ions (orbit losses).

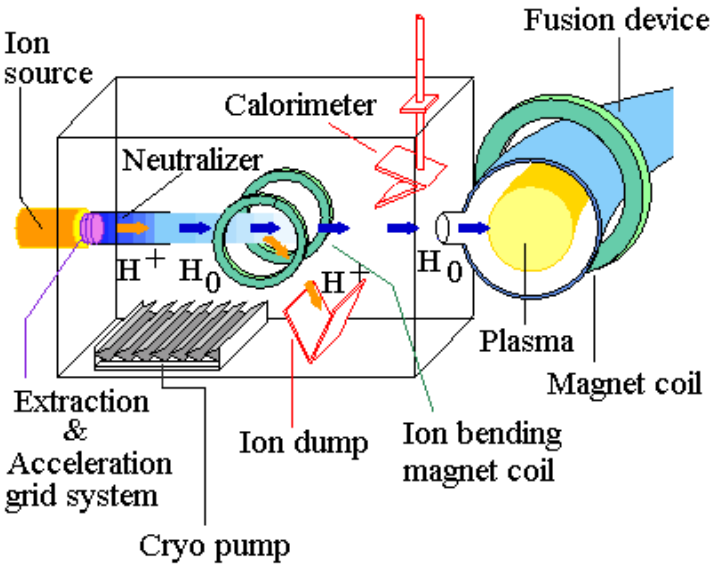

Figure 2.1: Neutral beam generation scheme.

2.2 Neutral beam generation

The characteristics of an ion beam are determined by the precursor plasma and the accelerator. Thus, for example, the ion beam current is determined by the plasma density, the plasma electron temperature, the extraction voltage and the extractor geometry; the beam emittance is determined by the plasma density distribution, the plasma ion temperature and the extractor geometry; and finally, the beam composition is clearly determined by the composition of the plasma. The physics of the ion source is thus largely plasma physics.
The generation of a neutral beam and its transport are best understood by subdividing the process into its successive steps, as shown in figure 2.1:

- *Generation* of a powerful ion beam.
- *Neutralization* of the ion beam.
- *Transport* of the neutral beam to the plasma vessel.

The physics behind the creation of ion beams is generally very well known, from experience of accelerators in atomic and nuclear physics: positive or negative hydrogen ions are extracted through electrostatic fields from a suitable plasma source and accelerated to energies of several tens of keV.
The essential difference from laboratory beams is the much higher beam current (tens of A) necessary to achieve the required power (several MW) and consequently the much larger beam cross sections (several hundreds of cm^2). This extension from the level of milliamperes to tens of amperes, while maintaining a reasonable beam quality.

The work in these past few years focused on a number of distinct achievements:

- The generation of large-area, uniform, quiescent plasmas for ion extraction (arc and RF sources).
- The idea of subdividing the beam into many beamlets by using electrodes with multiple apertures.
- The discovery of simple ways of controlling the direction of individual beamlets in order to yield the desired overall beam focal properties.
- The development of technical devices to cool from heat loads and protect the delicate electrodes against voltage breakdowns.

Charge neutralization of the ions occurs in charge-exchanging collisions of the fast ions with neutral hydrogen (or else) molecules present in the background gas in the neutralizer. Cold gas is used to create a certain gas target density inside the neutralizer for conversion of the ions into neutrals.
In the last stretch from the neutralizer, the transport of the neutral beam into the plasma vessel faces the problems of:

- Limited acceptance due to the finite size of the apertures (portholes) in the plasma machine.
- Removal of the not-neutralized fast ions in the beam which, depending on energy, may represent a significant fraction of the total beam power, and thermalization at suitable surfaces (Residual Ion Dumps).
- Removal of the cold gas out-streaming on the one hand out of the neutralizer or generated on the other hand by stray residual ions.

2.3 Positive and negative ions

Positive ion beams, neutralized by charge-exchange on gas targets, have been used in many early experiments to produce the required high power neutral beams; this is limited though to energies below 80-100 keV per nucleon, due to the rapid drop of the charge exchange cross section with energy. Early estimates though foresee beam energies in the 200-1000 keV per nucleon range for larger fusion devices (i.e. ITER): for this reason, the next generation of neutral beam systems will be based on negative ions. The motivation lies in betwixt the low binding energy of the additional electron (0.75 eV), meaning that it can be easily detached, yielding neutralization efficiencies of about 60% [6]. More information is reported in section 2.8.

2.4 Negative ions production

The development of negative ion-based systems for fusion is steadily progressing, year after year with renewed confidence: in 1992 the first complete negative ion-based beamline produced 100 kW of 100 keV D_0 beams in the framework of a collaboration between JEARI and CEA, 16 A of H^- were produced at Nagoya in 1994, and 40 mA H^- beams were accelerated to 700 keV at JEARI in 1995 [4]. After these successful small power injectors, large negative ion-based systems have been installed at JT60-U and LHD with achieved maximum parameters of 400 keV, 17.4 A and 180 keV, 34.5 A, respectively [7].
A negative ion-based system with two 400 MeV, 7.5 MW beamlines is actually proposed for DTT [14], a downsized system with respect to the future 1 MeV ITER NBI source. These projects use (and will use) large negative ion sources of 40 A with 200 A/mm^2 D^- current densities, high performance electrostatic accelerators and efficient neutralizers to convert the D^- beam into D_0.
Negative beams though do not come without drawbacks: it will be seen that the attractive feature in the neutralization of negative ions, its low electron affinity, constitutes a problem when ion production or acceleration is considered: in the first place it is difficult to attach this additional electron; secondly a considerable fraction of negative ions are destroyed ("stripped") by collisions with plasma or neutral particles before being extracted from the sources or accelerated to the final energy. This makes negative ion production and acceleration a difficult though fascinating subject.
The present high performances have been obtained in particular from large cesium-seeded sources. The fundamental processes which lead to this kind of negative ion production are well known: wall formation and dissociative attachment. Nevertheless, their relative weight and combination in sources are still not completely understood and object of research.

2.4.1 Two concepts for an NBI Ion Source

The generation of a powerful ion beam first requires a suitable deuterium plasma source, which should possess the following characteristics:

- An ion flux density of typically a few hundreds of amperes per mm^2 over a total area of several hundreds of cm^2 in order to provide the required tens of A per source.
- Sufficient uniformity in space ($< 10\%$).
- Sufficient uniformity on long pulses (tens of minutes range).
- As high a content of atomic ions as possible (more than 80%, see this section).

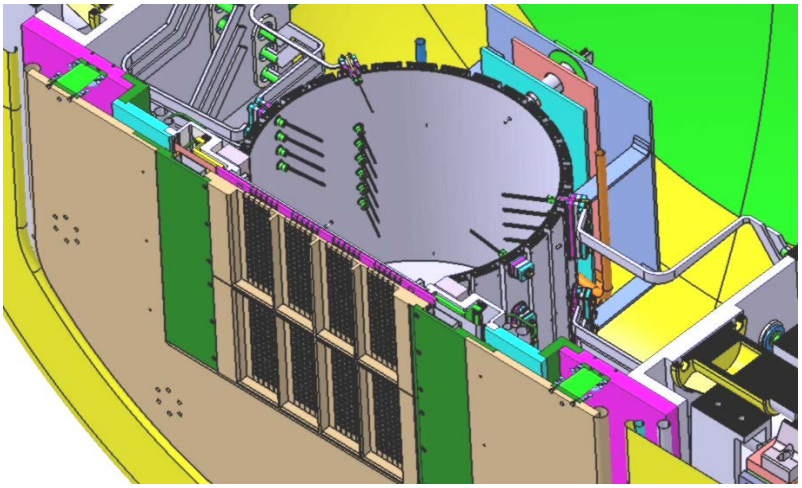

Figure 2.2: Arc driven source overview.

- A sufficiently low content of impurity ions.
- A reasonable efficiency for the consumption of electrical energy and precursor gas.

There are basically two different concepts that are used: Arc-driven and Radio Frequency (RF) sources.

- Arc Sources: in an arc discharge source electrons are emitted from a hot cathode and accelerated by a DC voltage of typically 100 V into the source, where ionization due to breakdown of the gas molecules leads to the desired arc plasma. Numerous configurations, differing in the way of optimizing the ionization efficiency of the fast electrons (for example by utilizing magnetic fields, biasing the source walls etc.) have evolved over the last 25 years. The development of these sources is based mostly on empirical methods, theoretical work being of a more accompanying nature and addressing singular topics only like ionization efficiency, composition of atomic and molecular species, etc.
- RF Sources: the RF source generates an azimuthal high-frequency electric field, generally induced by a RF coil, for the necessary acceleration of electrons in order to create the source plasma. A typical frequency for RF sources is 1 MHz, and typical RF powers 100 kW. RF sources have many advantages over the arc sources, such as:
  - Long lifetime due to the absence of filaments having a limited thermal cycle time;
  - Low costs due to the possibility of disconnect the RF generators electrically from the high potential of the plasma source;

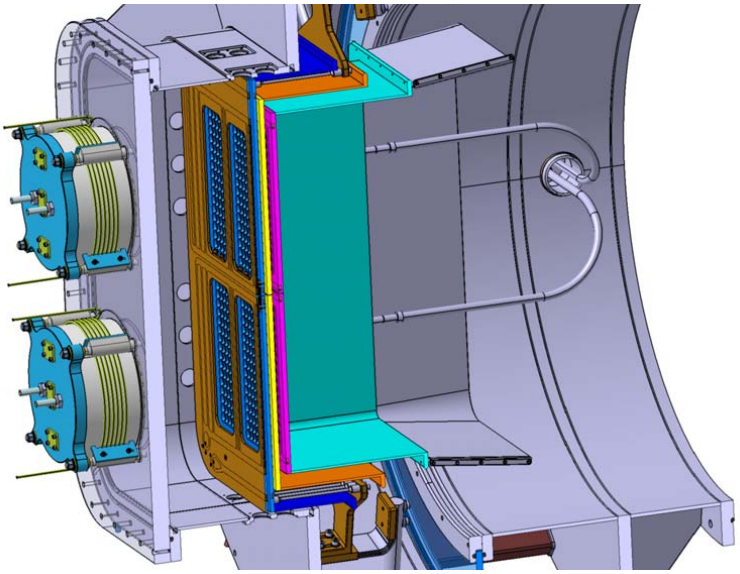

Figure 2.3: Radio Frequency ion source overview.

- Better control, during beam modulation, of the extracted ion current due to the direct response of the ion density in the source to changes of the RF input power, making active beam current control possible;
- Simpler source (less electrical connections compared to arc sources), making remote handling easier.

Due to these advantages, RF sources are a promising alternative to the Arc sources for the 1 MeV negative ion injectors of ITER. A picture of a RF ion source is shown in figure 2.3.

2.4.2 Cesium seeding

One of the biggest breakthroughs that have interested the negative ion generation has been the discovery of the influence of cesium as a catalyst for the reaction: in fact, when cesium is seeded into the ion sources, the work function of the open surfaces is dramatically lowered, leading to an increased reaction rate [8]:

- The negative ion yield increases by a factor of 3÷5.
- The operating pressure decreases.
- The stray electron current co-extracted ratio drops from 10÷100 in pure sources to 1÷5.
- The production of negative ions in Cs seeded ion sources increases linearly with increasing arc or RF power, and no experiment has yet revealed saturation.

It is not yet completely clear whether the improvement results predominantly from surface production or simultaneously benefits from an enhancement of volume production. In favor of the first explanation is a strong dependence of the negative ion yield on the temperature of the plasma grid in the extraction region, which can be experimentally related to a decrease of the work function. On the other hand, Cs lowers the electron temperature; this might be favorable to dissociative attachment, and, in any case, reduces the destruction rates.

2.5 Beam optics calculations

The formation of the ion beam occurs through electrostatic extraction and acceleration to the desired energy. The geometry plays an important role in the performance of the injection system, because there is no way of controlling the beam along his trajectory once left the source. Hence, in contrast to nuclear physics accelerators, the primary ion beam must receive its final status at the the extraction level.
Although the physics of ion beam optics is better understood than the field of plasma sources, the situation is not quite satisfactory. There is a lot of analytical and numerical description available but in varying agreement with experiments. Hence there is not yet a sufficiently solid basis for the designer. The main physics topics in this field are: perveance, divergence and steering.

2.5.1 Perveance

The current that can be extracted from a single aperture between two charged electrodes is not infinite: it is determined by space-charge of the particles, that locally modify the electrostatic field until the pull is no longer in effect. It is a common phenomenon in electron guns and has already been detailed, leading to the well-known Langmuir-Child law for non-relativistic charged particles:

$$I = C \cdot V^{\frac{3}{2}} \sqrt{\frac{Z}{M}} \left(\frac{a}{d+h} \right)^2 \tag{2.1}$$

where C is a constant, I the extracted ion current, V the applied electrostatic potential, Z and M the charge and mass number of the extracted ion, a the aperture radius and d the gap size between plasma and extraction electrodes. $d + h$ is the length of the region in which the ions feel the electrostatic accelerating potential. The ratio

$$P = \frac{I}{V^{3/2}} \tag{2.2}$$

is called *perveance*.
The optimization of the current per aperture is limited by various constraints: the geometrical dimensions are constrained by breakdown (for given voltage, there is

a minimum gap) and the presence of aberrations. This explains why a large beam cannot be extracted from a single aperture, but instead the electrodes must be subdivided into many apertures of smaller dimensions.

2.5.2 Divergence

The ions are emitted from a curved surface, whose radius is determined by the self-consistent space-charge of ions (called *meniscus*). For a given extraction geometry there is an optimum match between the ion flux density delivered by the plasma generator and the electrostatic potential V.

Because the matching condition for optimum beam divergence has to be met in

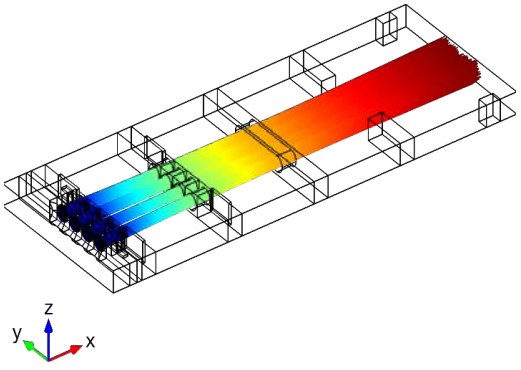

(a) Analysis of a beamlet row with the code COMSOL.

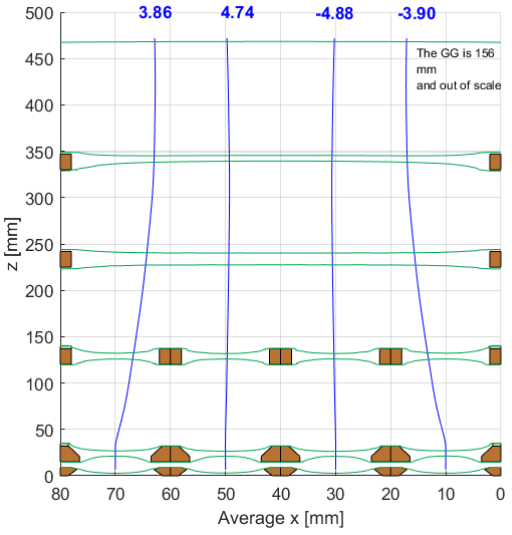

(b) Equivalent trajectories.

Figure 2.4: Divergence calculation example (values in blue are in millirad) [21].

every single aperture, the plasma generator has to produce an ion flux density which is reasonable uniform in space and time. Non-uniformities larger than 10% usually lead to a degradation of beam divergence.

Other than that, a number of devices and design modifications devoted to aid on the correction of trajectory have been devised, such as plates placed at the sides of the acceleration grids to locally deform inward the electrostatic lenses (*kerbs*) or enlarged grid apertures to flatten the isopotential curves in the center [3]. Their disposition is accurately studied in order to obtain (in some cases even control) a desired value of deflection at the muzzle of the accelerator.

2.5.3 Beamlets Steering

As mentioned before, the direction of the beamlets cannot be controlled once the ions leave the source assembly. These ions have all the same space-charge: a potential well is hence formed, deforming locally the electric field and causing them to diverge indefinitely, if left unchecked. The simplest way to deal with this issue is to allow for a certain background density of neutral particles in the zone between accelerator and neutralizer, obtaining the phenomenon called Space-Charge Compensation (SCC). The fast ions, colliding with target neutrals, generate opposite charge ions up to almost complete compensation of space-charge, and therefore to unmodified divergence. The phenomenon appears for both positive and negative ion beams, but is more evident for negative beams: this is because the generated positive ions are comparable in mass with the traveling negative ions, whereas the positive counterparts have electrons for compensating, which are far more mobile and tend to escape the potential well.

This mechanism is supposed to work so efficiently to effectively omit divergences

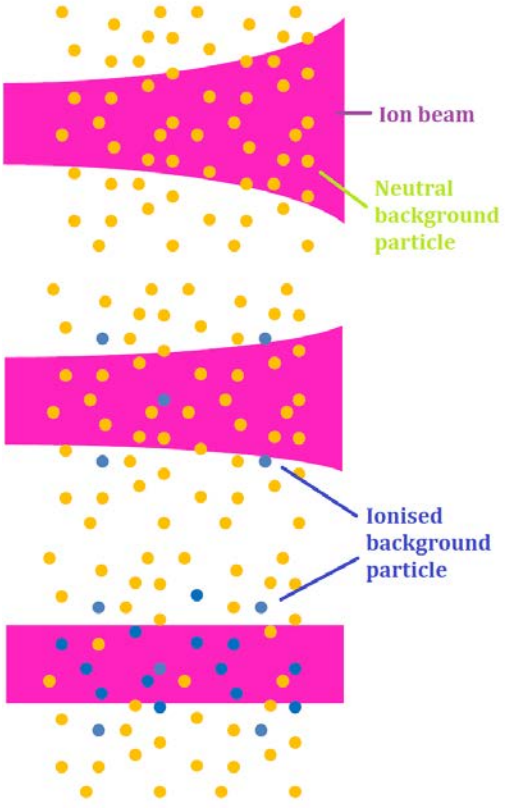

(a) Conceptual schematic of SCC.

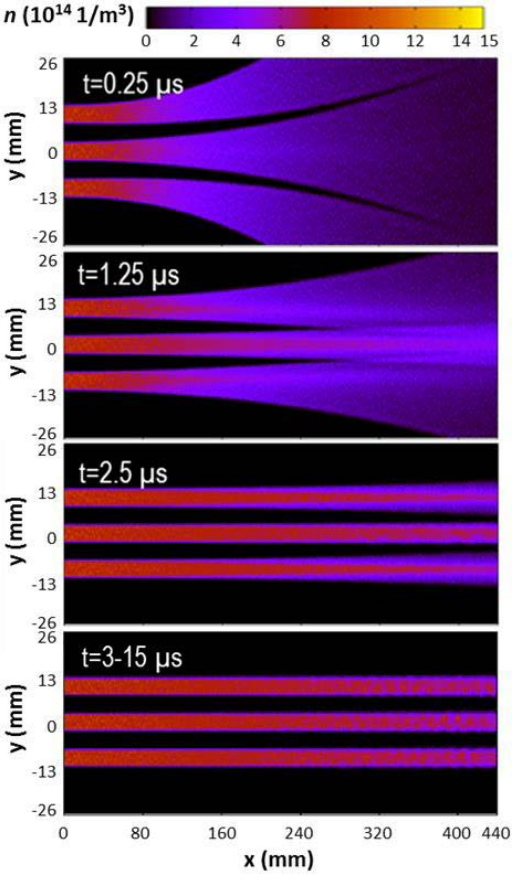

(b) Experimental images of negative SCC.

Figure 2.5: Example of Space-Charge Compensation.

effects after the accelerator, as can be seen in experimental images for negative ions (figure 2.5). The beam dimensions at some distance from the ion source (e.g.for example at the porthole of the plasma device) are determined as said before by the divergence of the single beamlets and on the other hand by the finite dimensions of the plasma grid. The latter effect can be made negligible by mechanically aiming or steering the individual beamlets or groups of beamlets onto a common focal point or line.

2.6 Negative ions extraction and acceleration

Due to power efficiency reasons, the large ion current required for fusion can only be achieved via electrostatic acceleration. This technique has been developed at up to some keVs for large positive ion beams, but the 1 MeV domain has yet to be fully investigated, and proof-of-principle experiments are operating in Japan and Europe (namely MITICA, the full size NBI assembly foreseen for ITER and being built in Padova). Besides the difficulties expected with high voltages, in particular electrical breakdowns with high capacitive energy dissipation, the negative ion extraction and acceleration require many features which make the design much more complex than that of positive ions. This is due to two fundamental facts:

- The negatively charged ions are accompanied by co-accelerated stray electrons originating mainly from the source plasma.
- The already few fragile negative ions may be "stripped", i.e. neutralized or positively charged, during the acceleration.

Three steps in acceleration can be distinguished:

1. Electrostatic extraction of the ions from the source;
2. Pre-acceleration, typically to 50÷100 kV;
3. Full energy acceleration (up to 400 keV as foreseen for DTT).

Numerical simulations were performed in order to optimize the electrical and magnetic fields in the extraction area, obtaining an optimal configuration shared by many pre-conceptual designs.

2.6.1 Negative ion beam extractor and pre-accelerator

As explained before, ion beams are typically composed of several beamlets, each of which is extracted from the ion source separately from the others. This is achieved by assembling a set of carefully aligned grids, in which cylindrical or conical apertures are drilled. These grids are polarized at various voltages, to achieve the desired beam

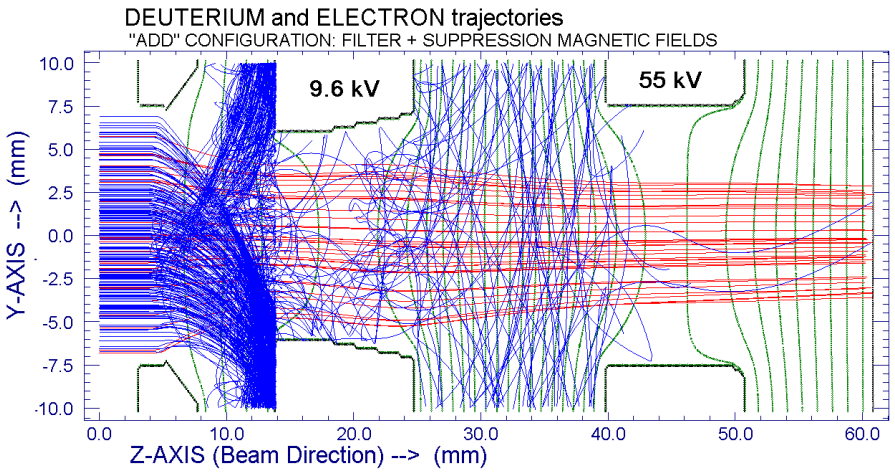

Figure 2.6: Examples of electrons (blue) and ions (red) trajectories for the ITER NBI beam source, calculated with TRACK code [9].

energy. The geometry of the accelerating channels and the gap between grids are carefully designed to control beam optics.
The first grid separates the source plasma from the accelerator (Plasma Grid, PG). In the second grid, often named "Extraction Grid" (EG), permanent magnets are inserted in order to deflect the stray electrons and to prevent them from being further accelerated (Co-extracted Electron Suppressing Magnets, CESM). This magnetic field breaks the axial symmetry of the acceleration channel. Therefore, exact calculations require 3-D codes, whereas 2-D codes were sufficient for calculating positive ions beam optics. Furthermore this magnetic field has to be compensated by opposite fields, created by an other set of magnets, the Asymmetric Deflection Compensation Magnets (ADCM): in order to prevent any deflection of the D^-/H^- beam, one must ensure that

$$\int B dx = 0$$

along the beam path.
An example of D^- beam and electrons trajectories calculation is given in figure 2.6.

2.6.2 Overview of negative ion extraction and acceleration physics

The codes which are used to simulate the extraction and acceleration of negative ions are generally derived from codes used for positive ions. These codes numerically solve, in multi-step iterative process the following intertwined equations:

- Electrostatic equations, solved for the scalar electrostatic potential V:

$$\begin{aligned} \nabla^2 V &= -\frac{\rho}{\varepsilon_0} \\ \mathbf{E} &= -\nabla V \end{aligned} \tag{2.3}$$

- Magnetostatic equations, in the no-current case, solved for the scalar magnetostatic potential V_m:

$$\begin{aligned} \nabla^2 V_m &= 0 \\ \mathbf{H} &= -\nabla V_m \\ \nabla \cdot \mathbf{B} &= 0 \\ \mathbf{B} &= \mu_0 \mu_{rel}\, \mathbf{H} + \mathbf{B}_r \end{aligned} \tag{2.4}$$

- Dynamic equations, solved for the trajectory $\mathbf{x}_i$ of the i-th particle:

$$m_i \frac{\partial^2 \mathbf{x}_i}{\partial t^2} = q_i \left(\nabla V + \frac{\partial \mathbf{x}_i}{\partial t} \times \mathbf{B} \right) \tag{2.5}$$

where m_i and q_i are the mass and the charge state of the traveling particle, $\mathbf{B}$ the magnetic deflection field, and $\mathbf{x}_i$ the particle spatial position. The boundary conditions of the problem correspond:

1. to the voltages on the electrodes;
2. to the plasma sheath (meniscus);
3. to the magnets embedded in the grids.

In the case of negative ions, the simulation of the plasma sheath is particularly complex because:

- Positive and negative ion beam optics are not merely mirror problems with respect to the electric charge; five species have now to be considered in the plasma: e, H^-, H^+, H_2^+ and H_3^+.
- The non-axial symmetry of the magnetic field makes it a 3-D problem.
- Large electron currents can be extracted; typically $\frac{I(e)}{I(H^-)}$ is in the $1 \div 20$ range.
- A significant fraction of the negative ions can be stripped in the accelerator, losing their second electron by collisions with the neutral gas. The cross section is large: $10 \div 15$ cm^2 at E(H^-) < 20 keV, while the gas density in the pre-accelerator is in the $10^{13} \div 10^{14}$ cm^{-3} range.

A complete simulation of the plasma boundary requires a treatment based on kinetic theory, but proper beam optics simulation requires all the aforementioned physical effects to be taken into account, in particular the electronic contribution to the space charge in the extraction gap and the stripping which modifies the space charge during acceleration.
Most codes include the dominant physical effects mentioned above, allowing the major accelerating parameters to be predicted confidently. This is particularly important for the new generation of accelerators in the MeV range which are under design. However, progress is still required in the plasma boundary simulation. This could enable controlling secondary phenomena, such as beam halo or aberrating particle trajectories, which may have an impact on the detailed design of high power accelerators. A testament to that will be this very thesis, trying to evaluate stray trajectories of stripped particles.

2.6.3 Co-extracted electrons suppression

The main source of stray electrons in a negative ion accelerator is the source plasma. Since large electron currents can be extracted (in the worst case at least of the same order of magnitude), it is essential to stop these electrons as early as possible. This is the role of the transverse magnetic field. Experiments conducted at JAERI showed that a significant fraction of the electrons, in spite of being forced to impact onto the extraction grid surface, could leak out and be further accelerated. JAERI tried and inserted a third grid just after the extraction grid, which could be negatively biased to $1 \div 2$ kV with respect to the extraction grid in order to repel stray electrons. This system was very efficient, but increased the grid complexity and the decelerating potential of the electron suppression grid degraded the ion optics.
The electron leakage was explained after the development of a 3-D Monte-Carlo code, which took into account the secondary emission and the backscattering of electrons. It was demonstrated that the stray electrons originate from backscattering; in the relevant energy range, $5 \div 10$ keV, the probability of electron backscattering on a metallic surface can be as high as 30%. If the magnetic configuration of the suppression system is not appropriate, an electron can escape after one or two reflections and can be accelerated downstream. On the other hand, the low energy secondary electrons (a few tens of eV), in spite of being numerous, have a small Larmor radius which prevents them from progressing far into the accelerator before being dumped on the electrodes.
Actual designs for the magnetic suppressing system provides a square array of two counter-polarized Co-extracted Electron Suppression Magnets, generating a lateral pull on the upside of the grid; plus a couple of Alternate Deflection Compensation Magnets on the sides to eliminate the undesired persisting deflection effect on the ion beam downstream. All magnets are made in Sm_2Co_{10}, known for its ability to maintain high remanence even at high temperatures. Other sources of stray electrons

are those generated by charge-stripping reaction during the acceleration, impinging on the grids downstream and contributing to heat loads: to stop them early on, some other magnets called Secondary Electron Suppression Magnets (SESM) can be embedded in the successive grids, repeating the design of the EG.

2.7 Concepts for the MeV acceleration

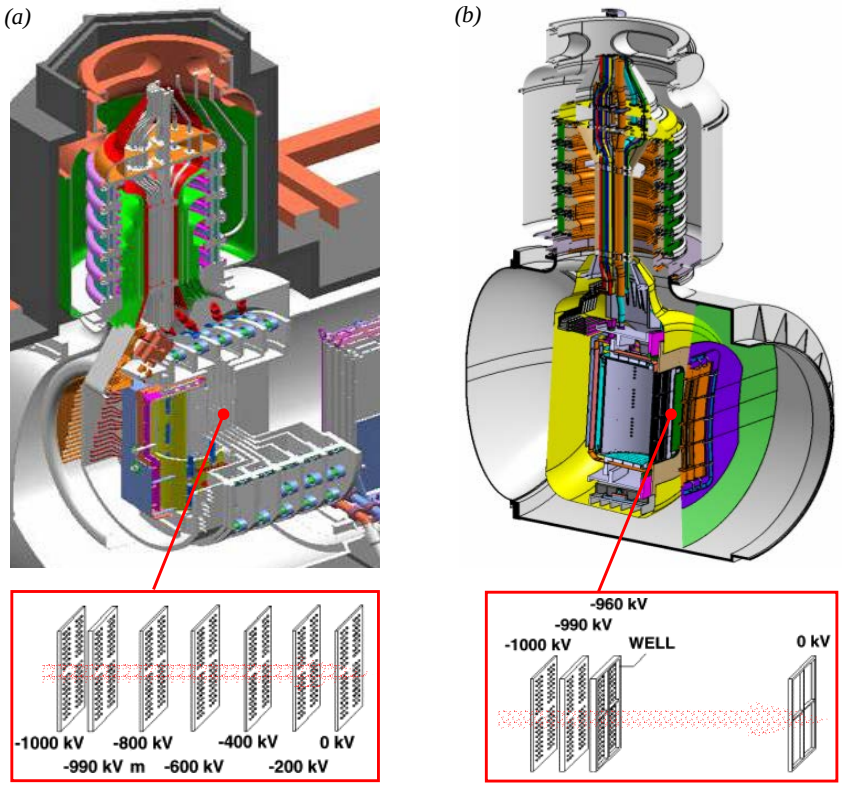

Figure 2.7: Overview of the two concepts for the ITER Neutral Beam Injector: (a) MAMuG; (b) SINGAP.

The problem of development for the accelerator of the ion beam up to energies in the MeV magnitude has a mostly technological nature; it is certainly the major issue today. Some concepts are considered at the moment:

- The reference concept, the "Multi Aperture-MUlti Grid" (MAMuG) accelerator (see figure 2.7a), accelerates the ions to high voltage in several intermediate steps, each having more or less the same aperture pattern as the plasma and extraction grids. This requires several multi aperture grids at intermediate potentials, the power supplies to feed them and water cooling to each grid. This system is extrapolated from positive ion accelerator concepts and features

long and narrow acceleration channels from the source to the last acceleration stage [10]. At the moment, it is the system of choice for the pre-conceptual design for DEMO and designated for DTT[14].

- The European alternative concept, the "SINGle Aperture-SINgle GAP" (SINGAP) accelerator (see figure 2.7b), pre-accelerates the beamlets to 20-50 keV, then accelerates to the final energy in one single step through large apertures in the final (ground potential) electrode [11]. SINGAP would enable reducing the gas load in the accelerator and greatly simplifying the design of accelerator, power supplies, and HV transmission lines, but some difficult issues will have to be faced, such as the acceleration of stray electrons to full energy.

Another relatively recent proposal concerns the possibility of creating the sources in a *modular* fashion, separating the big chambers described in section 2.4.1 into separate, self-contained sources, in combination with one of the concepts above. Its advantages are manifold:

- Enhanced possibility of controlled pulse, by switching on and off part of the modules thus controlling the NBI power in an almost continuous fashion;
- Possibility to skew each source separately, aiming them effectively towards the Breeding Blanket;
- Easier maintenance and replacement of defective modules, instead of operating on the whole source.

2.8 Negative ions neutralization

Negative ion neutralization is relatively easy due to the low affinity of the additional electron of only 0.75 eV. A neutralizer is required to:

- Provide a high neutralization efficiency.
- Operate with the lowest possible gas input, in order to limit the stripping losses of the negative ion beam in the accelerator as well as the reionization losses of the neutralized beam.
- Prevent injection of additional impurities into the tokamak.
- Require the lowest possible additional power.
- Have a long service life and a high reliability.

All negative ion-based neutral beam projects are based at present on the use of gas neutralizers. Anyway, the always created positive ions and those particles that did

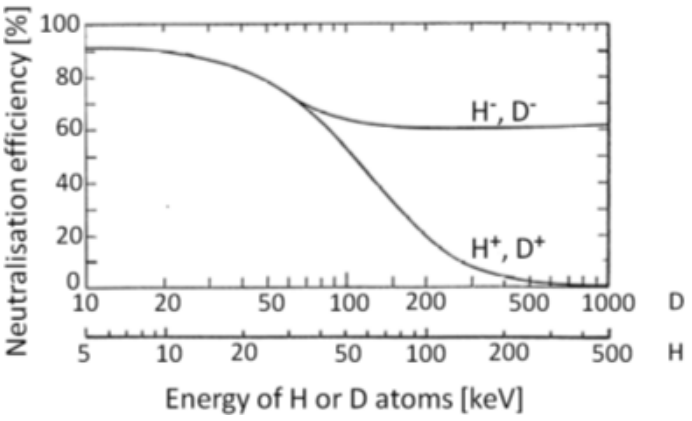

Figure 2.8: Optimum neutralization efficiency for positive and negative hydrogen ions against beam energy per nucleon.

not react in the neutralizers require a residual ion dump system in negative ion based neutral beam injectors. The gas neutralizer is based on collisional detachment:

$$\underline{D}^- + D_2 \longrightarrow \underline{D}^0 + D_2^- \tag{2.6}$$

(the fast particles are underlined). Unfortunately, several reactions compete with that. The main competitor is the ionization of the fast neutrals:

$$\underline{D}^0 + D_2 \longrightarrow \underline{D}^+ + e^- \tag{2.7}$$

The optimum neutralization rate η_{MAX} is, in first approximation, a function of $r = \frac{\sigma_{-0}}{\sigma_{0+}}$, the ratio of the cross sections of the dominant reactions above:

$$\eta_{MAX} \;=\; \left(\frac{1}{r}\right)^{\frac{1}{r-1}} \tag{2.8}$$

Since the both dominant reactions correspond to the same physical phenomenon (electron detachment), r and η_{MAX} are practically independent of the beam energy for energies above several 10 keV (see figure 2.8).

A gas neutralizer is a technically simple and passive system with a reasonable high efficiency. It has a major drawback: the required high additional gas load which increases the pumping requirements in large beamlines by a factor of 2 or more. At the moment, R&D is ongoing on a possible alternative to gas neutralizers, with potentially far higher efficiency: photoneutralizers. These neutralizers would make use of high powered lasers in a reflective chamber to relay the ionization energy ot the ion particles, hence requiring no additional background density and theoretically reaching 100% of efficiency.

2.9 Overview on losses mechanisms

To conclude this short NBI overview and beginning to focus the attention on the main problems treated in this thesis, here is a short description of the internal mechanisms that are cause of the enormous heat fluxes (up to 10 MW/m^2) present in particular sections of the accelerating grids. Those also are the main input to devise an apt cooling subsystem to keep the grid system in working condition for the whole pulse operation. As such, they will need to be accurately computed using multi-physics FEM code, accounting for possible charge-exchange reactions.

2.9.1 Co-extracted electrons thermal fluxes

As mentioned before, the co-extracted electrons that flow out of the plasma source together with the negative ions are effectively deviated by dedicated magnets on the grids. This concentrated flux of electrons on very small surfaces makes them easily the most critical heat flux component that the cooling system will have to dissipate. To evaluate them, a self-contained FEM model has been constructed, simulating the flux of electrons exiting the source at a fixed current density and integrating the deposited power over the grid surface.

2.9.2 Stripping losses

In negative NBIs, the stripping losses in the acceleration system are due to the background gas, both flowing out of the source or composed by now-neutralized particles. These losses generate both fast neutrals and secondary electrons, that impinge on the grids and contribute to the overall thermal load. The principal stripping reactions that happen along the accelerator are:

$$\begin{aligned} D^- + D_2 &\longrightarrow D^0 + D_2 + e^- \quad \text{Single stripping reaction;} \\ D^- + D_2 &\longrightarrow D^+ + D_2 + 2e^- \quad \text{Double stripping reaction.} \end{aligned} \tag{2.9}$$

From collisional theory, the flux of charged particles able to cross the accelerator can be estimated thanks to the reactions' *cross-section* σ and the formula:

$$\Gamma_i = \Gamma_0 \exp^{-\frac{x}{\lambda}}, \tag{2.10}$$

where $\lambda = \frac{1}{n_{bg}\sigma}$ is the mean free path for incident particles, combining the background gas density n_{bg} and the cross-sections for each reaction (figures 2.9, 2.10). The stripping cross-section changes with the kinetic energy of the incident particle: since particles are accelerating, also the frequency of collision changes along the beam source. Given the shape for the curve of both single and double stripping reactions, it is easy to see how the frequency of collisions reaches a maximum value relatively early in the accelerator, then gradually decreases as kinetic energy continues to increase:

this aspect entails strong neutral particle loads in the early sections of the accelerator.

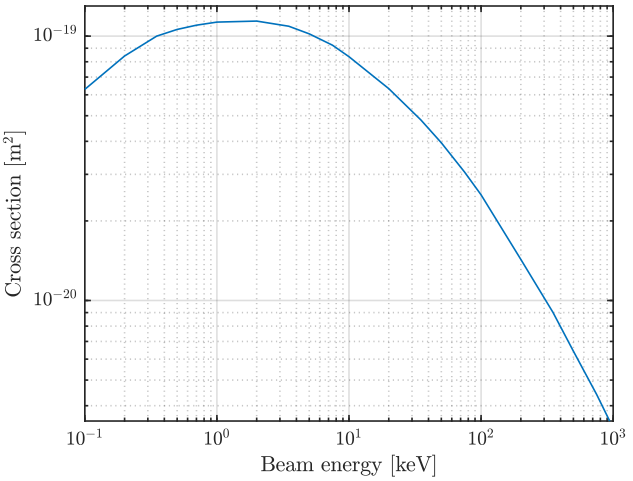

Figure 2.9: Cross-section for single stripping reactions [12].

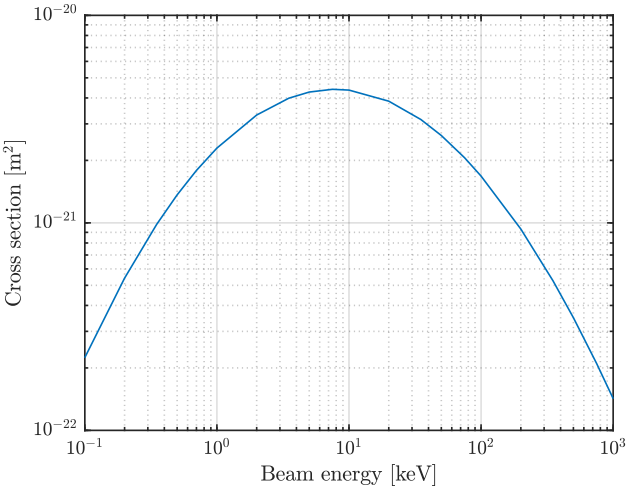

Figure 2.10: Cross-section for double stripping reactions [12].

Beam-wise, these losses can be as high as 20÷40% of the total current depending on the hypothesized density profile, and degrade the overall performance of the system; from the thermic point of view, they can constitute a significant contribution to the heating of the acceleration grids. It is therefore important to reduce the source operating pressure as much as possible. This drives low pressure source (< 1 Pa) development and experimentation on pumping systems and vessel components.

Chapter 3

Divertor Test Tokamak NBI design and materials

SUMMARY - The Divertor Test Tokamak (DTT) as a experimental facility will require both power and control to replicate fusion-like heat deposition conditions to test new Plasma Facing Components and divertor. A consistent part will be delivered through NBIs, which actual design is very similar to the latest pre-conceptual one for DEMO, downsized to 400 keV, in two separated injectors accounting for about 18 MW of heating power. Still, some differences are present, such as the decision to not use a vacuum insulated source, or the possibility of manufacturing acceleration grids through additive manufacturing.

3.1 Introduction

In 2012, the European Fusion Development Assembly published 'Fusion electricity - a roadmap to the realization of fusion energy' [13], devising a strategic vision towards the ambitious objective of attaining generation of electrical power by a Demonstration Fusion Power Plant (DEMO) by 2050. One of these missions portraits the need in the near future of defining and designing a particular experimental facility, denominated Divertor Test Tokamak (DTT), dedicated to aggressive R&D in the matter of power exhaust and Plasma Facing Components. In fact, as described in the article, whereas in ITER some choices in the matter have already been made and will be thoroughly tested once the experiment effectively starts, there is no guarantee that the the ITER baseline strategy (for what it is, an experiment) will be able to be extrapolated in what are the DEMO requirements (a full-power reactor). The lack of alternative solutions would delay the realization of fusion by 10-20 years. By building a separate facility to work in parallel with ITER, the aim is to cover with on-field experience the gap in Plasma Facing Components knowledge during the design process from proof-of-principle devices to actual full-power experiments like ITER and future DEMO-like reactors, that cannot simply be filled with numerical simulations.

More in detail, some of the most evident problems in the analysis of fusion exhaust:

- Available experiments operate in Scrape-Off Layer (SOL) and plasma bulk conditions very different from those expected in DEMO-like reactors;
- As a consequence, simulations too are based on SOL models that are not reliable in extrapolating to DEMO;
- The impact of different configurations for a key component like the *divertor* is something to be evaluated accurately by experimentation;
- Other problems might arise from integration of a possible solution with other key tokamak subsystems, as in vacuum pumping, etc.

It is also a great opportunity of collaboration between all of the nations participating in the project, each one with its own part to handle; and also on occasion to shine the spotlight of fusion research on Italy, with such an important project.

3.2 DTT test facility

DTT will be a new experimental fusion facility, expected to be built in Italy near Frascati, Rome, during the next few years. The location already hosts an ENEA research center and the FTU Tokamak experiment, easing authorizations and licensing procedures. Overall budget has been fixed at about 500 M€; and based on that amount with direct experience on several other similar devices, the complex of vessel, magnetic coils, cooling/pumping, Heating & Current Drive, power supply and diagnostics have already been evaluated by a dedicated DTT team, composed of ENEA, CNR, INFN, RFX and other European Universities, listing and justifying all of their choices in the latest Interim Report [14]. Some of the main parameters for DTT are listed in table 3.1.

Parameter	**Unit**	**Value**
R	[m]	2.11
a	[m]	0.64
$\frac{R}{a}$	[-]	3.3
Volume	[m^3]	29
I_p	[MA]	5.5
B_T	[T]	6
Pulse length	[s]	90

Table 3.1: Main DTT parameters (for Single Null configuration) [14].

Since the DTT experiment is finalized to study the power exhaust in a fusion reactor-like environment, the first parameters that are desired to be maintained are those

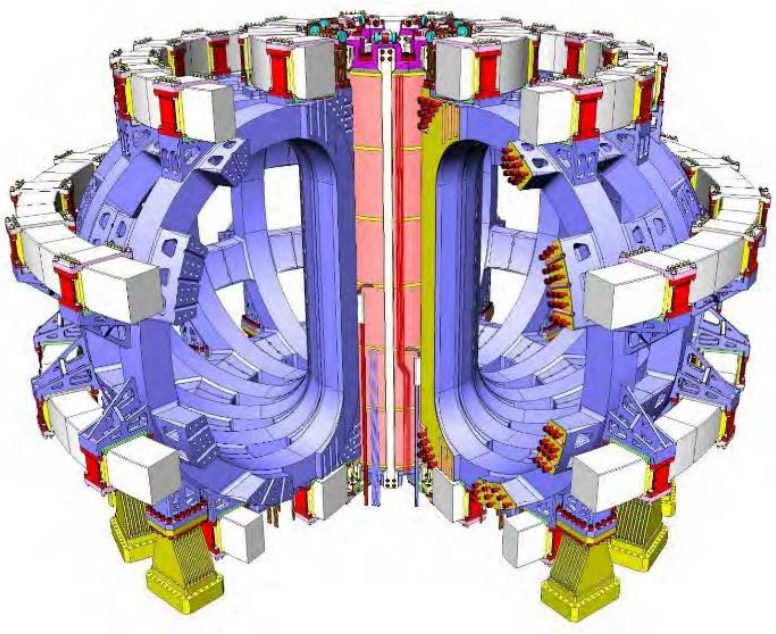

Figure 3.1: DTT toroidal, poloidal and Central Solenoid superconducting coil assembly [14].

connected with bulk plasma, the divertor and the SOL regions: in order to do so, a total amount of 45 MW in additional power will be installed in successive phases (as described in figure 3.2) after the completion of main vessel and coil systems, subdivided in different H&CD devices. The additional heating will be covered for about 15 MW with Ion Cyclotron Resonance Heating (ICRH) and 10 MW with Electron Cyclotron Resonance Heating (ECRH), both using antennas to couple EM waves with particles in the plasma, at frequencies that are close to the resonance cyclotronic frequency of each. In doing so, particles are continuously accelerated in resonance during their alternate revolving motion, increasing their kinetic energy and thus their temperature.
The rest of the power (about 15 MW) will be appointed to a Negative NBI system, to reliably accelerate high energy neutral beams able to cross the plasma bulk and heat its center.

3.3 DTT NBI overview

Following an overall detailing of the structure will be presented, with a more in-depth look at the NBI heating and cooling systems that are going to be adopted in DTT.

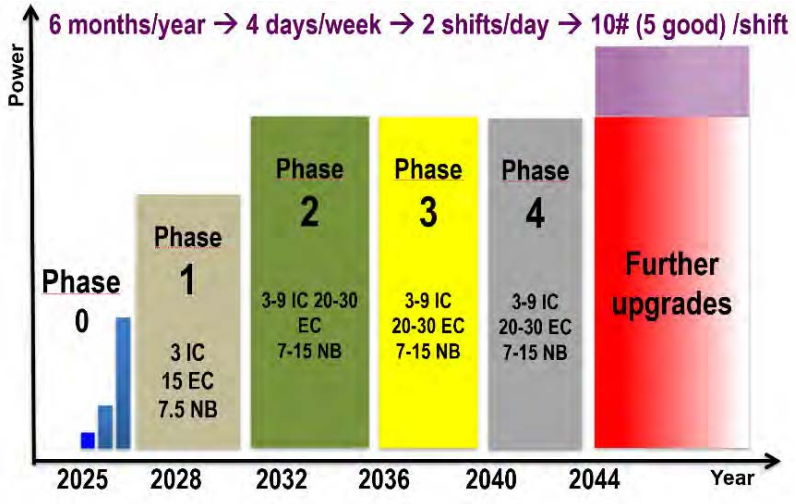

Figure 3.2: Schematic planning of the DTT H&CD operations. [14]

3.3.1 Energy and injection parameters

An NBI system based on the acceleration of positive ions would inject efficiently particles into the plasma with energies in the order of 80-120 keV. This energy would lead to a too peripheral power deposition for DTT. In order to heat particles in the core at the density that is expected to be reached, a negative-ion-based NBI system at higher energies ($E \geq 300$ keV) is then proposed. Presently a 400 keV beam energy is considered as the most interesting value, a good compromise among costs, size and performances. Moreover, the adoption of two acceleration stages would give the same voltage gap per acceleration stage (200 kV) of the ITER NBI thus allowing to exploit the advanced R&D carried out during the last years for the ITER NBI and MITICA. In order then to reduce the shine-through, magnetic ripple losses and help the current drive, an accurate assessment of the injection angle α_{inj} has been carried out, using existing codes ORBIT and METIS. This simulation showed good heating footprint and reduced losses for angles of injection of $\alpha_{inj} \geq 40$ °at the first wall, as shown in figure 3.4.

3.3.2 Beamline conceptual design

The conceptual design follows from the above physics requirements, and considers as main guidelines the maximization of flexibility, RAMI (Reliability, Availability, Maintainability, Inspectability) and efficiency, also minimizing cost and weight. The definitive version of the design will provide, as has been mentioned, 400 keV of beam energy, through the acceleration 40 A of D^- from 1280 grid apertures; the grids will be four in total, of which one for extraction and two for acceleration. The cooling and pumping will be hybrid, featuring both Non-Evaporable Getter (NEG) pumps

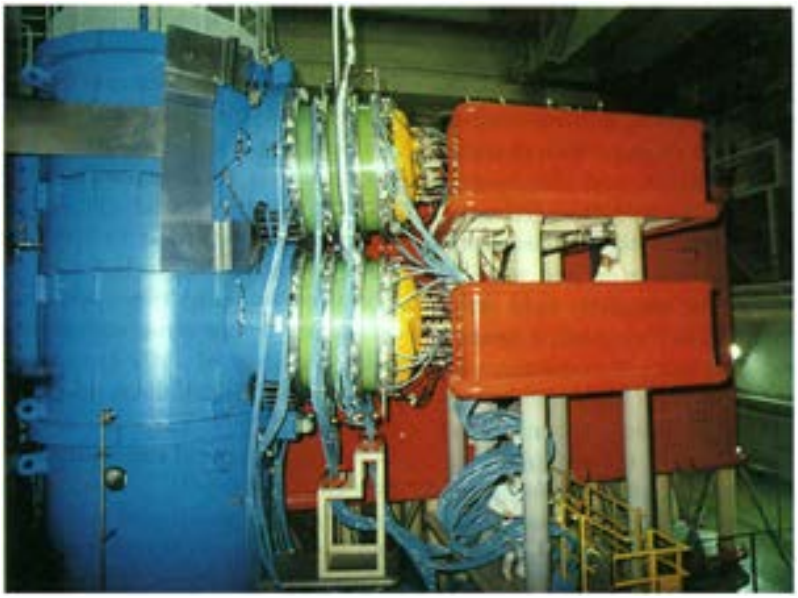

Figure 3.3: Detail of the JT-60 NBI system, showing the beam sources and the FRP rings [15].

and cryopumps. The overall beam will be divided into four separate vertical blades: such a choice permits to minimize the minimum length of the neutralizer to have an acceptable reaction ratio, and also allow for better deflection control. For this device, the target wall plug efficiency is $\approx 45\%$, meaning that improvements must be made as to transfer successfully at least 45% of the absorbed electric power into the plasma bulk, without problems during the pulse.
The main components of the injector assembly, shown in figure 3.4, recuperate some different concepts from other existing NBIs from around the world: similarly to the NBIs of JT-60 [15], a design with an air-insulated beam source is proposed, to reduce the vacuum volume, increase the source accessibility and avoid the need of a complex air-to-vacuum bushing to connect the SF_6 insulated Transmission Line to the vacuum vessel. A drawback of this solution is the required clearance between the ion source and the surrounding structures (at least 2 m, to avoid electrical discharges).

The DTT design differs though from the Japanese scheme in the choice of ion source: in fact, it is proposed to use the same Radio Frequency source concept adopted for ITER, developed by IPP Garching [16] in Germany, creating plasma through Induction Coupling. Other Beam Line Components (BLC) will be ITER-like too, while the vacuum vessel will be without large flanges (differently from ITER) to reduce cost and weight: only small flanges are foreseen for pumping, diagnostics and BLC supplies, while the BLC maintenance is planned to be from behind, by removing the beam source and setting the components on rails.

The accelerator grids, situated in the beam source, are the main argument of this Thesis: they represent a critical component, as they have a rather complex design,

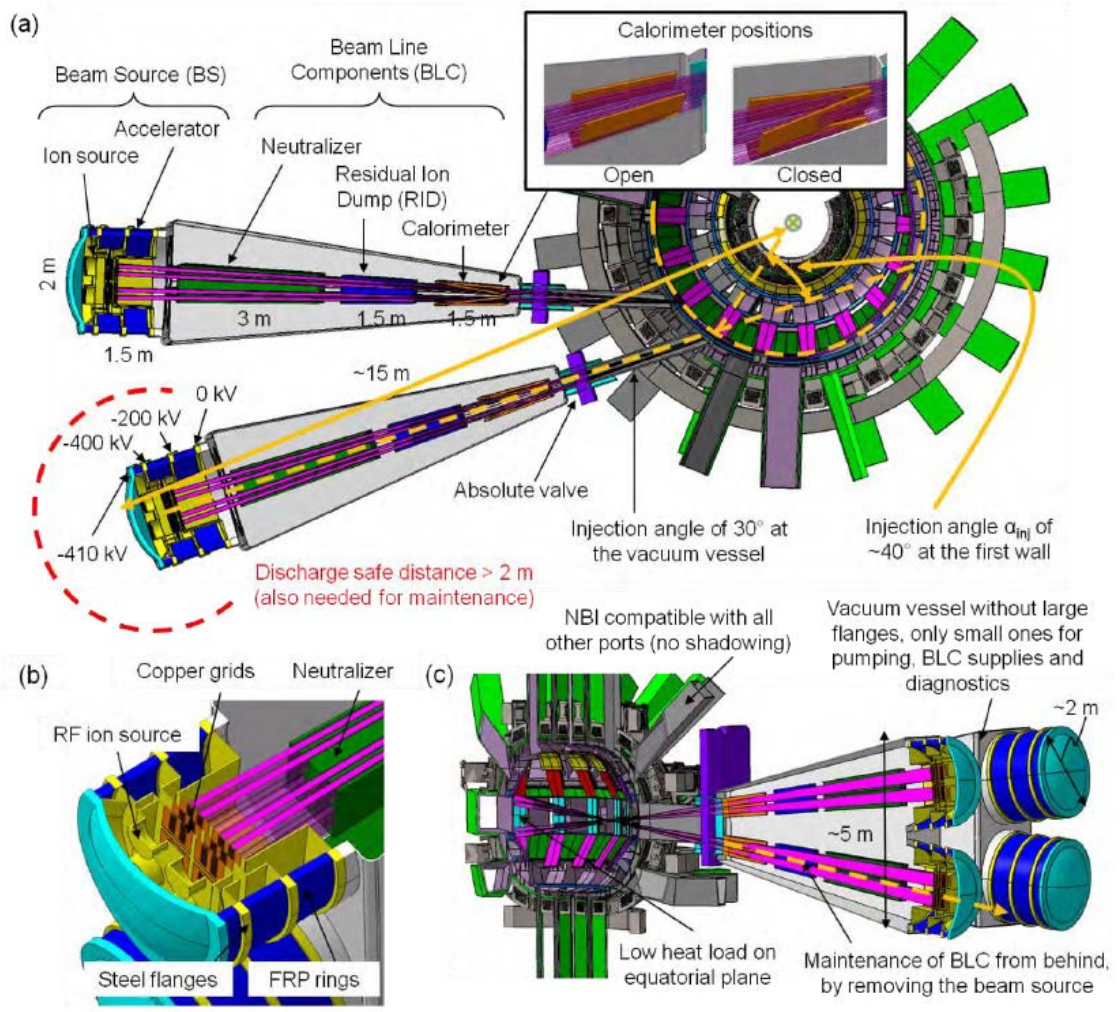

Figure 3.4: Design of the DTT NBI with main parameters: (a) top view; (b) horizontal section view; (c) vertical section view. [14]

with very small cooling channels, apertures for the negative ions and grooves for the electron deflection embedded magnets. The possibility of manufacturing by means of copper electrodeposition on a milled base plate made of pure copper has already been proven in recent works from Consorzio RFX [17].
As this is a rather complex manufacturing process, the possibility to manufacture the grids by additive manufacturing is currently being investigated. The printing process requires though the use of particular materials, that at even the state-of-the-art show rather low thermal conductivity. A presentation is given in section 3.3.3.
Another future critical R&D program will be carried out to develop and validate a manufacturing process for a rather unusual component, the Fiber-Reinforced Polymer (FRP) rings of the accelerator. These rings are interposed between the acceleration grids; by that, these rings must be quite large (diameter of 2 m and length of 0.5 m)

and must fulfill several important functions, i.e. to maintain the electrical insulation between the acceleration stages, and to support the beam source while being perfectly leak tight and having a vacuum compatible surface on the internal side. This kind of technology still has not explored here in Italy, whereas a solution has been found with the Japanese JT-60 air-insulated NBI; their experience may prove valuable to devise such components for DTT.

3.3.3 Additive manufacturing material properties

Over the past decades, Fast Prototyping using polymers powders heated on deposited on successive layers has become well known and established as the "3D printing" widely known to the public. What is of recent availability is the technology behind electron beams and power lasers, able to locally melt metal powders deposited by a nozzle. That, coupled with computer-aided design (CAD), poses the prospect for layer-by-layer fabrication of complex, custom metal or alloy products impossible to achieve by more conventional processing of wrought or cast precursors, also reducing manufacturing time and costs. These components include simple geometries, including various sizes of cylindrical and rectangular block products as well as more complex mesh and foam components which are especially novel because they can be fabricated in complex systems with high specific strength and stiffness [18]. More in detail, the main available techniques are:

- In a Electron Beam Melting system (EBM) electrons are generated in a gun and accelerated up to 60 kV, focused by electrostatic lenses and scanned by a CAD program, with speeds $\approx 10^4$ mm/s and beam current $\approx$30 mA for the preheating phase, slower and with lower current for the actual melt production; scanning is $x - y$, rising in z direction, with gravity-fed powder and under vacuum operation.

- In a Selective Laser Melting system (SLM) melting is achieved through a focused laser beam (e.g. 0.2 kW Ytterbium 100 μm laser): the laser is scanned by a CAD driven mirror and focused onto the powder bed, recoated mechanically to form the successive layers; scanning can be selective along both x or y direction, the atmosphere is Argon or Nitrogen and scanning speeds comparable with EBM.

As for DTT case in particular, the main problems of printed components are the high porosity for some materials (making it a poor choice for water-cooled grids in a vacuum environment) and the impossibility of effectively melting some metal powders, including copper, without the appropriate wavelength lasers. This is a major drawback, because copper is the best choice for the acceleration grids, with its mechanical strength, high thermal and electric conductivity: the most promising alternatives that are proficiently printable have been identified in mixed copper powder alloys, namely $CuSn_{10}$ and $CuNi_2SiCr$. Basing on datasheets values for these

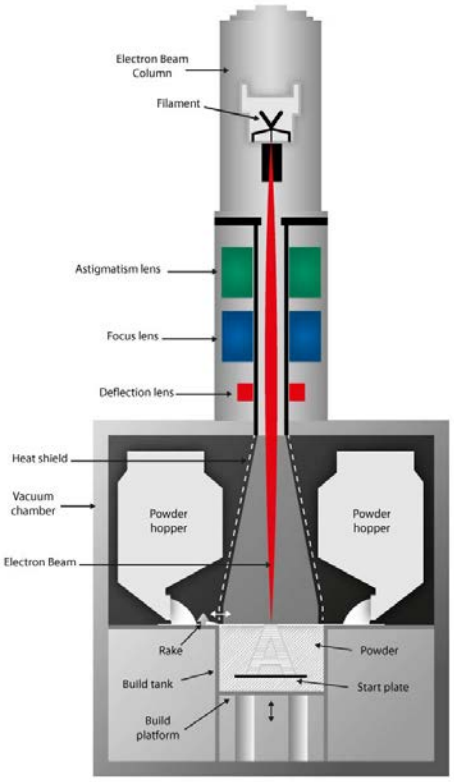

(a) EBM system.

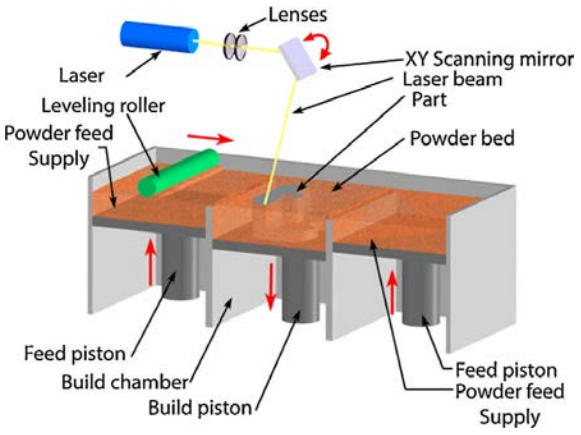

(b) SLM system.

Figure 3.5: Conceptual design of additive manufacturing devices.

materials, even with a very high percentage of copper (e.g. in $CuSn_{10}$, copper is around 88 %), unfortunately the its properties are not carried on. This procedure is being investigated by the Consorzio RFX NBI design team: some Italian companies are in possession of additive manufacturing technologies for these materials and have been asked to produce some test components for accurate analysis of parameters as the chemical composition, mechanical strength, vacuum holding and porosity, thermal conductivity, specific heat and electric conductivity; and is also under extensive R&D. Some early values are presented in table 3.2.

Parameter	**Copper**	**$CuSn_{10}$**	**$CuNi_2SiCr$**
Thermal conductivity [$\frac{W}{m\,K}$]	400	20.98	84.56
Specific heat [$\frac{J}{kg\,K}$]	385	377	397
Yield strength [MPa]	200	386	225

Table 3.2: Main parameters for grid material candidates, at reference temperature 20°C. [14]

A first look shows the sheer difference between materials: aside of a better overall

mechanical strength, the thermal conductivity performance drops dramatically, down to 1/20 of pure copper for $CuSn_{10}$. This value is key in determining the final working temperature of the acceleration grids during a NBI pulse: similarly to electric circuits, the lower the conductivity, the lower is the power flow through the grid from the deposited heat to the cooling system, and increasing thus the temperature. Temperature dictates then thermal expansion, translating into tensile stress and cycles of life for each component: this is why in this thesis only temperature can be evaluated in the simulations as a first solution; future other works then will be strong of this analysis and proceed further down the chain of effects with more ease.

Chapter 4

FEM verification of cooling designs

SUMMARY - When developing high performance cooling systems for NBI devices the use of Finite Element codes is key to the verification of the quality of the choices made on the drawing table before prototyping. This topic has been researched before, and the next section will be dedicated to the application and confrontation of existing design choices in the case of DTT, through the use of a novel method of simulation of the heat loads.

4.1 Introduction

As has been stated before, the Neutral Beam Injectors are very complex systems, with the beam source being the most critical component: its incorrect design can largely affect the performance of the whole injection system. Reaching inside the source itself, the most delicate part is definitely the acceleration grid system: other than being able to cope with extremely high voltages, these grids must withstand all of the power loads caused by internal loss mechanisms while respecting a number of criteria for optics, stress and temperature. This, given the research nature of DTT, must hold true also for all the foreseen operating scenarios, from the less demanding to the full nominal pulse discharge. These requirements have one thing all in common: to respect them, there is the need to dissipate the impinging power load, hence the cooling circuit grid design comes into view. The task is not easy as it may seem, since great part of the grid is already occupied by apertures and grooves, severely limiting the possibilities for coolant distribution. All things considered, this is hardly a new, untrodden field of research: the problem has existed since NBIs were devised, but only recently with the ITER full-scale injector MITICA researchers have taken the line a little further, devising channels for heat loads in the order of magnitude of 1 MW/m^2. Namely, the works of Ph.D. graduate G. Gambetta [19] showed and tested interesting improvements to the design choices for MITICA.

The chapter is dedicated to the whole numerical simulation process, starting from geometry and design data, up to finally obtain crucial work parameters such as surface grid temperature and cooling channel pressure drop. In particular, this objective will be pursued by applying the designs obtained by precedent works and comparing the results. The codes used will be the commercial FEM code COMSOL® Multiphysics for the analysis and MATLAB® for data and logfile post-processing.
COMSOL is a very interesting and versatile FEM code, able to add and link together many different physics sets with relative ease, either in stationary or time-varying conditions; and recently is adding more and more support for problems related to particle physics, making it a more than appropriate choice to tackle the appointed task.

4.2 Problem formulation

The specific case of simulation of cooling systems requires a particular set of physics, different than those used for particle tracing in electromagnetic fields illustrated before, namely heat transfer in solids coupled with one of the many possible formulations available for turbulent flow in fluid mechanics.
Heat transfer follows the well-known Fourier equation for thermal fluxes and the heat balance condition, in stationary conditions:

$$\begin{aligned} \mathbf{q} &= -\lambda \nabla T \\ \rho C_p \mathbf{u} \cdot \nabla T + \nabla \cdot \mathbf{q} &= Q \end{aligned} \tag{4.1}$$

where $\mathbf{q}$ is the heat flux; λ, ρ and C_p the material thermal conductibility, density and heat capacity; $\mathbf{u}$ the velocity vector of translational motion (if present) and Q is representative of all possible heat sources in the system.
As far as turbulent flow is concerned, the equations describing the phenomenon are far too complex to be quickly reported in this paper in simple formulas; all of the possible approximations though derive from the same set of equations, the Navier-Stokes equations for single-phase, non-isothermal flow. These can be solved in a given domain with due approximation for fluid velocity field, density, pressure and turbulence parameters; the code finally allows the possibility to link the thermal outflow from channel boundaries into the fluid domain, making the validation of cooling systems possible through FEM simulation. In the particular case of this thesis, all of the hydrodynamics simulations have been carried using the so-called $k-\epsilon$ turbulence model, a pretty common model choice for industrial-like applications and appropriate for the fully-developed turbulent flow present in the grid cooling channels.
The input of the next set of simulations will be:

- The surface heat load profile caused by stray electrons and neutral particles impinging on the acceleration grids, evaluated through a new method, directly

into COMSOL, with respect to other evaluations obtained instead through dedicated codes like EAMCC;

- Prescribed inlet fluid velocity and initial temperature, as well as outlet pressure;
- Channel and grid designed geometries.

The main output of these simulations will be the three-dimensional temperature map on the grid geometry, obtained in stationary conditions, on which many considerations can be made. More information on the matter of requirements is reported in section 4.5.

4.3 Grid geometry

The first step in every FEM analysis is the definition of the working geometry: a single DTT NBI source grid is expected to be around 1000 mm high, 1000 mm wide, divided into four subsources' segments of 400 mm $\times$ 400 mm for alignment and source geometry, and 17 mm thick. The apertures in each amount to 640, 160 for each subsource, disposed on a 5 + 5 by 16 array.

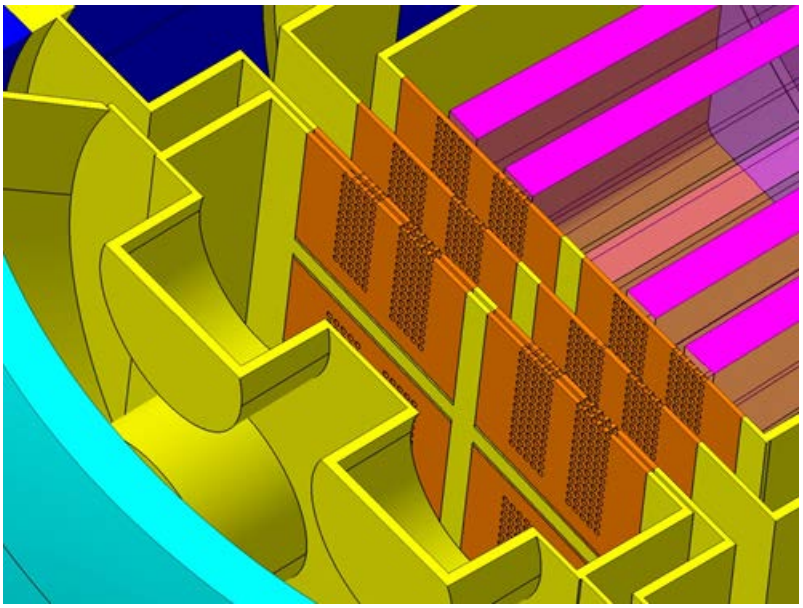

Figure 4.1: Focus of the DTT NBI grid, on horizontal cross-section. [14]

As said, the grids are heated by thermal losses, so a proper active cooling system is needed. Each channel will have to follow the shape dictated by optics geometry and the embedded electron suppression magnets used to deflect the co-extracted electrons onto the grids. The definitive design of the beam source foresees a total of 4 separate grids:

- Plasma Grid (PG): this grid has the task of separating the plasma source from the accelerator itself, and is charged to the lowest potential available. Its backside is designed to convey the ions generated by surface and volume production outside, and to create an appropriate meniscus to focus appropriately the beam to the next acceleration stage. Apertures have a 7 mm radius, and the grid itself is 9 mm thick, thinner than the others, due to optics requirements.

- Extraction Grid (EG): this grid is set in close proximity to the PG (at 6 mm distance) and charged at a difference of potential from the Plasma Grid ranging between 8000 and 10000 V. This is key to extract the correct value of current, and also for granting an optimal converging electrostatic lens. The shape of the aperture is conical, to create an asymmetric converging electrostatic lens, with a radius of 6.5 mm upstream increasing to 8.5 at the exit. Another key function of these grids is hosting the electron suppression and beam correcting magnets, housed in grid-like array embedded into the EG, with various thicknesses.

- Acceleration Grid (AG): this grid provides roughly half of the acceleration potential, together with the successive grid, and as such is placed farther in with respect to the EG (88 mm) for adequate voltage holding. The apertures are circular, of 8 mm radius, and they usually host within magnets for suppression of secondary electrons, generated along the beam path. This is not though the only available design, other have been proposed featuring tweaks and design choices to improve optics.

- Grounded Grid (GG): this is the last grid of the set, charged to ground potential and separating the rest of the injector beamline from the source assembly. In this thesis it is structurally similar to the AG, but other designs tend to hollow the grid itself, favoring an improved pumping inside the accelerator instead of controlling the optics accurately.

All of the correct geometric quotes used in the construction of the grid model have been kept the same as in the MITICA experiment [20], which has been proven to be an effective structural choice: the only differences are the total acceleration potential, which in MITICA is 1 MeV instead of the 400 keV needed in DTT; also keeping the liberty of changing the cooling channels' geometry. This is easily solved by removal of the two acceleration stages denominated AG2 and AG3 in figure 4.2.

As far as the cooling system is concerned, there is the possibility to run the channels either horizontally or vertically along the grid compound, but it is easier to run the channels in the horizontal direction, since the number of apertures is lower. Another possible choice to make is how channels will enter and exit the grid, either with a simple crossing of the grid reconnecting to two side common manifolds or either make the channel curve back on a lower available channel, hence entering and exiting on the same side of the grid: all depends on the space and pressure drop available from the designed pumping system.

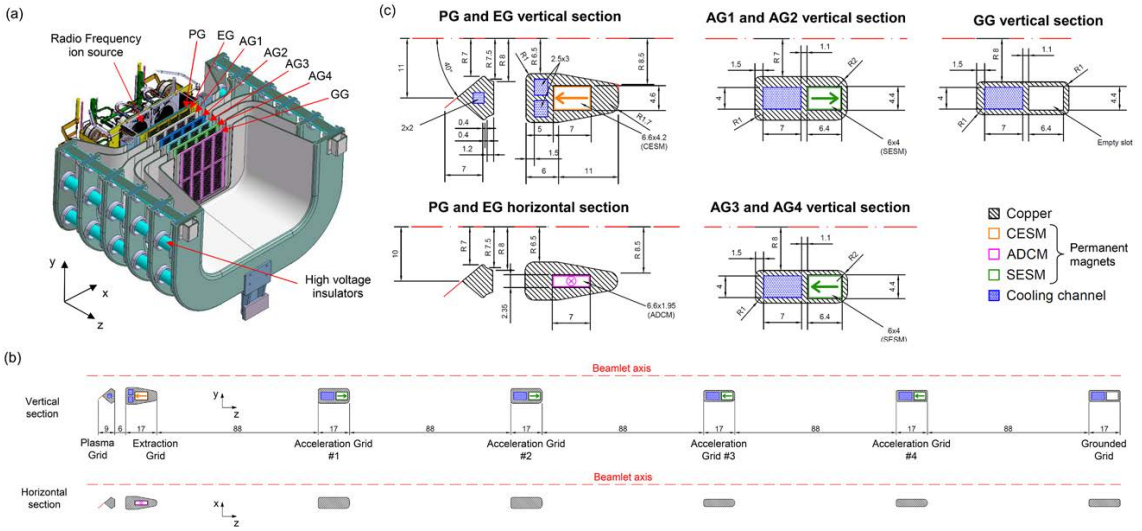

Figure 4.2: Design of the MITICA extractor/accelerator system. (a) horizontal section of the beam source; (b) vertical and horizontal sections in the aperture area; (c) detail view of the most relevant sections. [20]

4.4 Heat load profile

In this type of analysis covering how effectively a cooling system can be, the fundamental input parameter that is needed would be the heat load profile that needs to be countered. This section will veer off the main topic of the design of the cooling channels, describing instead the novel procedure adopted in obtaining this key map of values in the chosen FEM code. Naturally it is not necessary to obtain in detail the complete heat flux map, but by exploiting the symmetries of the grids the field of analysis can be restricted to a Unit Channel Prototype (UCP) as can be seen in figure 4.3.

4.4.1 Beam optic simulation

In order to capture the phenomenon accurately with as less border effect as possible, the smallest section of the grid containing an UCP unit has been selected for the analysis, meaning a 2 by 2 beamlet array, with the cooling channel in the center. Once obtained the geometry, the first step to obtain the heat load profile is to carry out a time-dependent FEM analysis combining electrostatic, magnetostatic and particle tracing physics, called Bidirectionally Coupled Particle Tracing in COMSOL. This type of analysis solves iteratively first the electromagnetic field and the effect of particle space-charge on them, successively computes the trajectories in said environment, and repeats the field calculation again, until convergence is satisfying. From this analysis, using the nominal current density on each of the apertures, it is possible to derive the ion trajectories of in the accelerator.

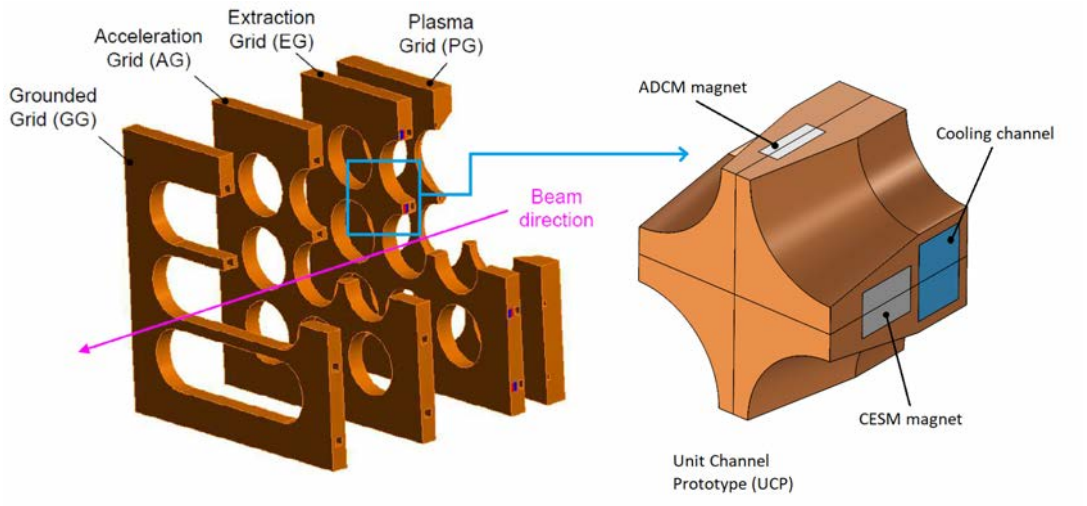

Figure 4.3: Example of an EG UCP section. It is evident how the symmetry is respected, and how it compares to the full grid.

Parameter	**Unit**	**Value**
J_0	[A/m^2]	293
Aperture area	[mm^2]	157.4
No. of particles	[-]	4×10000
Initial kinetic energy	[eV]	3
Extraction Grid voltage	[V]	10000
Time step	[ns]	5
End simulation	[ns]	200
No. of iterations	[-]	5

Table 4.1: Main simulation parameters in the stripping losses evaluation.

At this point COMSOL allows for adding a very interesting phenomenon to the model: by inputting an estimated density profile and cross-section curves, there is the possibility to simulate the probability of collisions for each of the particles used into the model, de facto being able of simulating the effect of the stripping mechanisms described in section 2.9.2. The first step is to hypothesize for a plausible background gas density inside the accelerator: this is not an easy task, since values like vacuum conductance are hard to estimate and many sources of background gas are present, like gas streaming out of the plasma source or neutral particles created by the stripping process itself. A good first approximation in this sense is a linearly decreasing density profile, starting by an estimated value of 0.2 Pa in pressure and lowering to about 1/5 of the original value at the mouth of the accelerator (see

figure 4.4). More accurate evaluations can be obtained with dedicated codes such as AVOCADO. The next step is inputting the cross section curves, but not before converting them in function of the length of the accelerator, thanks to the linear dependency of potential energy to the longitudinal coordinate: this makes them easier to use in the simulation context. The program now can compute the probability of each particle to collide, and also can release a new particle in its place (in our case, a D^0 or a D^+) and record the position of the event in a logfile. This will be important for the next passage, where the separate heat load effect of neutral impinging particles and both co-extracted and secondary electrons will be evaluated separately, and the position of the collision event will be the input for both of them.

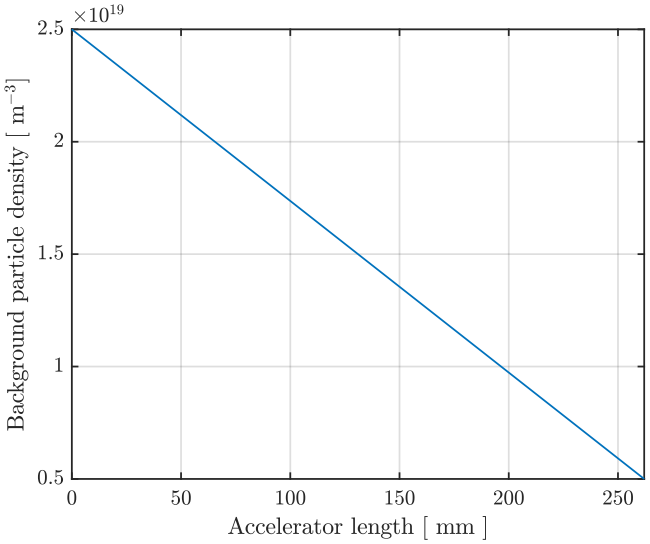

(a) Background density profile.

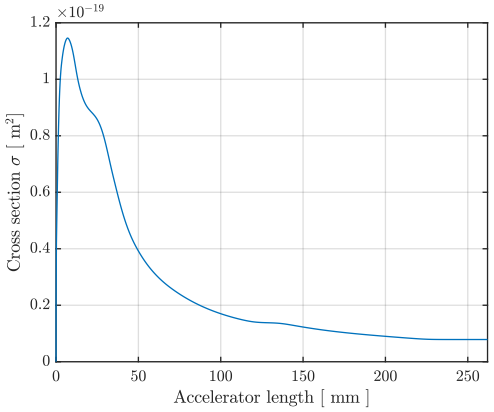

(b) Single stripping cross-section.

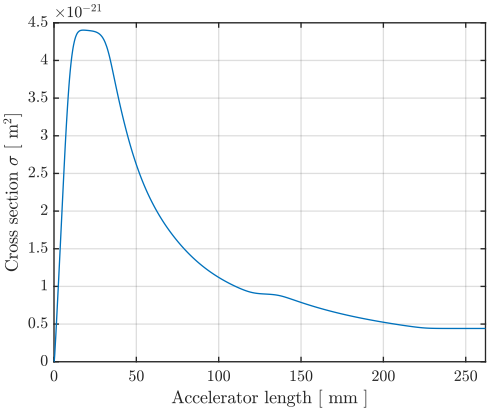

(c) Double stripping cross-section.

Figure 4.4: Input data for the collision simulation [12].

The results of the simulation can be seen in the figure 4.5.
Given the sheer difference in order of magnitude of the cross-section, the single stripping reaction is predominant; especially between the Extraction Grid and Acceleration Grid, where both density and cross-section reach their peak, the stripped particles are particularly present. There are a number of back-streaming ions that are able to reach the opposite side of the model: these are the D^+ ions, that feel an acceleration opposite than all of the other ions. They contribute to the heating of the plasma source, and as such effective cooling must be devised.

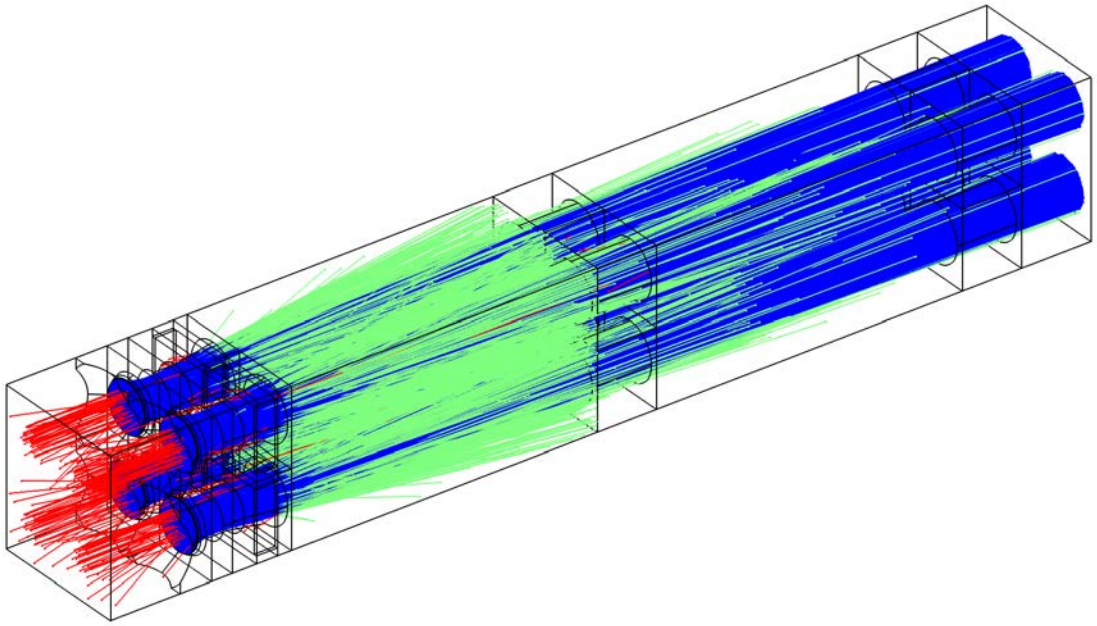

Figure 4.5: Result of the stripping simulation on the DTT NBI. In blue are the negative ions, in green the neutral particles and in red the positive ions.

4.4.2 Heat flux simulation

The heat flux map is obtained through two separate particle tracing analysis: one for electrons and one for neutrals. In both cases, the logfile obtained in the previous simulation will be the input: COMSOL allows for particle release from prescribed coordinates, at a specified current or velocity. In the electron case, another important source of particle would be the beam inlet itself, that in the worst of cases would allow for an electron current to be extracted of the same order of magnitude of the negative ions; whereas for the secondary electrons their current is estimated by averaging the Γ function between each couple of electrodes (reported in 4.2). Neutral particles instead can just use the value of speed that the progenitor negative ion had reached until the collision event (also stored in the logfile).

	PG-EG	**EG-AG**	**AG-GG**	**GG-ext**	**Total %**
Single stripping	7.42 %	5.33 %	1.13 %	0.92 %	14.8 %
Double stripping	0.26 %	0.35 %	0.07 %	0.005 %	0.685 %

Table 4.2: Averaged stripping losses percentages per acceleration sector.

The FEM code upon a wall collision thermalizes the particle speed and adds the contribution to a local accumulated variable Q_p, that averages the power deposited on each grid element thus obtaining the desired heat map flux. This brings about another problem: given the finite number of particles and the large dimensions of mesh elements, it is important to struck a balance between too large or too small elements. If the element is too large, the average will lose meaning, not accurately representing the spatial distribution of heat fluxes; if the element is too small on the other hand the average will account only for single particles that happened to land in that specific zone, leading to a flux map mostly empty but with a number of extremely high "hot-spots". Finally, for these analysis the number of iterations of the coupled particle tracing has been kept at 1, meaning that no iteration is carried out: this is because of the hypothesis that electrons carry a small space-charge, not able to significantly modify the fields they are in; whereas for neutral particles the reason is obvious. The particle trajectories and the obtained heat flux maps can be observed in figures 4.6 and 4.7, in their respective cases.

From these simulations is possible to observe how the heat load concentrates preferentially along the aperture perimeters: due to the high speed, as soon as these particles are created, they immediately tend to impinge in the proximity of the beam, in an annular symmetry, distributing somewhat the heat fluxes. What is not distributed instead are the heat fluxes due to co-extracted electrons from the beam source: they are strongly focused to the side of the apertures, in an alternating pattern, following the magnetic field imposed by the embedded magnets.
In fact, it is in the Extraction Grid that, under the preceding hypotheses, both the maximum heat flux peak (around 13 MW/m^2) and the maximum power loss to disperse (around 370 W per unit beamlet) are found. This fact allows for an ulterior simplification of the problem: by analyzing the most critical of the grids, all of the other ones will surely fall under the first one criteria and evaluated parameters: from now on, the only grid that will be needed to be modeled will be the Extraction Grid.

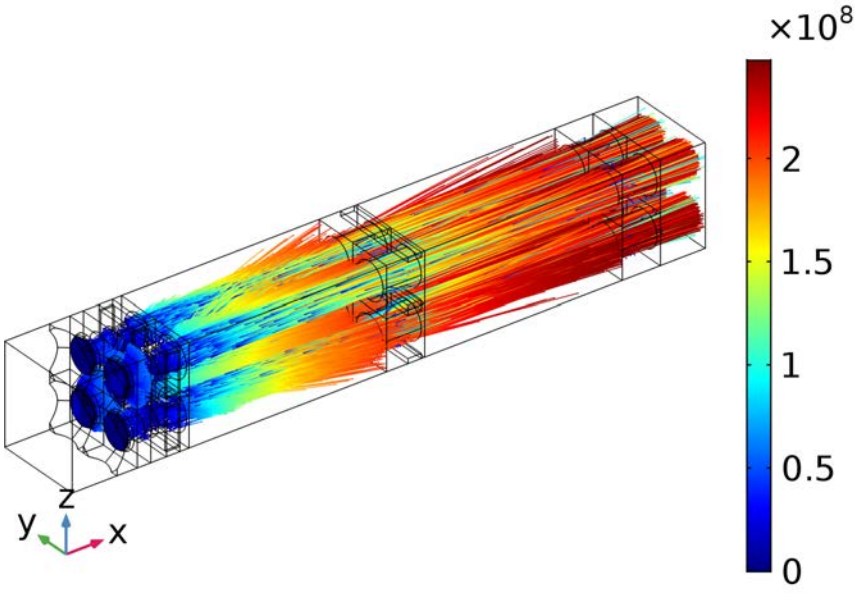

(a) Particle tracing solution; velocity map of the particles (m/s).

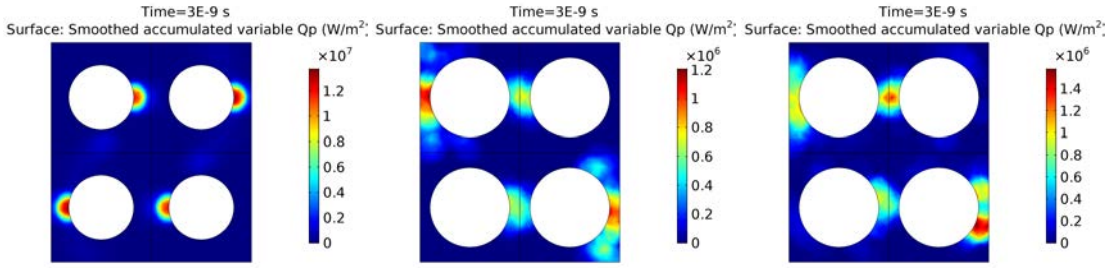

(b) EG heat flux map. (c) AG heat flux map. (d) GG heat flux map.

Figure 4.6: Heat flux map simulation for co-extracted and secondary electrons.

4.5 Grid design requirements

Due the pulsed nature of the test Tokamak, the usage of the NBI and hence of the acceleration grids will be pulsed as well. To guarantee a high component lifespan in a cycling application, there are a number of thermal and mechanical conditions to be respected:

- Peak temperature on the grids: should be as low as possible. In the case of electrodeposited copper, this temperature should stay under 300°C, since any over-temperature would worsen its thermo-mechanical properties.
- Peak stress on the grids: as low as possible, and generally satisfying the set of regulations established for mechanical characteristics for vessel components (ITER's Structural Design Criteria for In-Vessel Components, SDC-IC).
- Fatigue life: SDC-IC indicates a value of around 50000 beam on/off cycles.

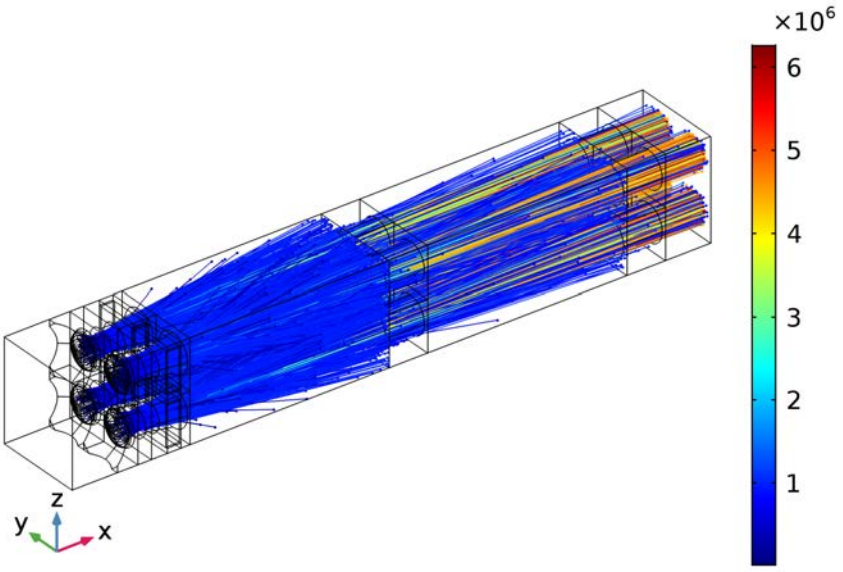

(a) Particle tracing solution; velocity map of the particles (m/s).

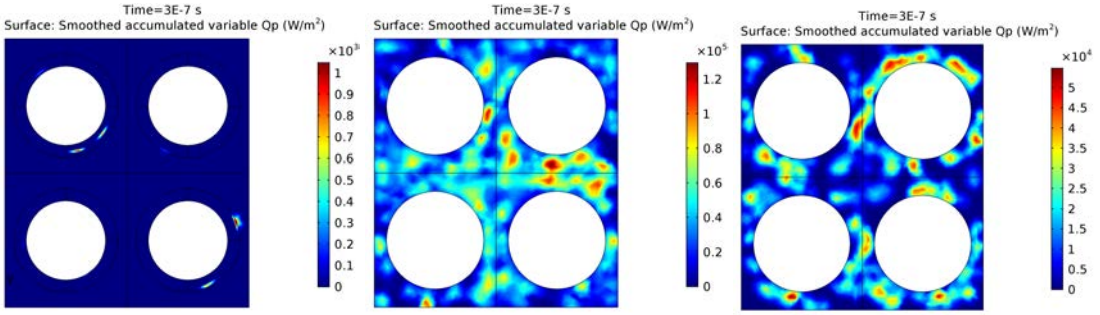

(b) EG heat flux map. (c) AG heat flux map. (d) GG heat flux map.

Figure 4.7: Heat flux map simulation for neutral particles.

- Grid alignment between all the grids in all of the operating ranges, and always lower than 0.2 mm.

Thermal fatigue is defined as the progressive damage and eventual rupture of a component due to cyclic stresses caused by the succession of heating and cooling phases where thermal expansion is partially or completely blocked: this field of material science is far from completely understood, but some experimental laws exist, showing a connection between the peak strain reached and the number of cycles to failure. Hence it is not hard to connect this fact to the direct correlation of strain (and grid alignment, by extension) to temperature: this suggests that the threefold requirement could be in principle reduced to a single one, to minimize temperature field and gradients, through identification of a cooling design solution able to perform the heat transfer from grid to coolant as efficiently as possible.
Another important set of requirements revolves around the most critical component of

a cooling system, the coolant fluid itself: the elevated voltage difference with respect the ground potential of the grids forces the designed coolant to be capable to guarantee electrical insulation between components, even in the most critical of situations. The coolant designed to accomplish the task is ultrapure water: such special water, treated in a local plant to eliminate all impurities that could increase its electrical conductivity, would possess good cooling capabilities, the desired electrical insulation and even good compatibility in neutron-activated environments, at the price of a costly purification plant, imposed by the regulations in the matter. One aspect that must be investigated further would have to be the electrochemical behavior of such a coolant in the designed cooling system, and also the influence of corrosion/erosion processes on the grid life-cycle. Finally, a set of designing constraints to keep into consideration when working on channel geometry:

- Pressure drop constraint: the design must limit its hydraulic losses, avoiding excessive curvature and narrow channels. The limit can be set similar as the one adopted in MITICA of 6 bar along a whole horizontal section.
- Structural requirements: in order to have an acceptably long cycle life and robustness even in such grueling operating conditions, each channel design has to account for at least a minimum gap of 1.5 mm from heated upstream surfaces and 1 mm from all other boundaries.
- Velocity constraint: even if erosion mechanisms have not yet been fully explored, water velocity has been set close to the maximum reached in the most recent solution, 10 m/s.
- Geometrical constraints: as well as the beamlet apertures, space must be accounted for the deflection magnets embedded, for each of their respective sizes.
- Technological limits: depending on the chosen method of manufacturing, there are different gaps and sizes that can be effectively created during the construction process: for example, in the electrodeposition process, the minimum diameter is linked to the size of the utensil of the milling machine.
- Design flexibility: designs should be able to be implemented on all of the different electrostatic grids without significant change from each other; it is also recommended to prefer cooling channels designs which guarantee the vertical and horizontal symmetry of the electrostatic grid, in order to avoid any possible error during the mounting phases.

4.5.1 Non-thermal stress relieving design guidelines

The importance of controlling accurately the temperature field and gradient in order to guarantee an optimal performance and life cycle for an NBI component has been

cleared in the previous paragraphs, but it is not the only solution to the problem. Fatigue strength and strain can be reduced through:

- Geometrical devices: this denominates all of those changes applied to the grid without modifying functional aspects of the body and limiting the concentration of stress in excessively solicited areas. This is done for example by filleting sharp edges or by diverting the flows of stress thanks to additional slots in the structure.
- Residual surface stresses: based on the assumption that a component under cyclic operation has a longer life if it is exposed to lower maximum stresses, it would be possible to create a compressive preload near critical regions. This integrated load would sum itself to the thermal expansion induced stress, decreasing the maximum reached. There are various methods to achieve this condition, all based on plastic deformation of the surface, that induces a negative elastic deformation persisting in time.
- Thermal treatments: these constitute a procedure able to create surface compressive residual stresses that in some cases can even double the fatigue strength. These methods consist of treatments of surface hardening as nitrurization, cementification, etc. Particular attention must be paid to the fact that these surfaces residual stresses can be very intense, and it could occur that at a certain depth, tensile stresses arise leading to reduced fatigue life expectancy.

Earlier studies on the matter concentrated on the first set of devices, introducing into the non-heated parts of the electrostatic grids a number of Stress Relieving Slits (SRS) in the horizontal axis [20]. These would be limited to a part of the thickness, in order to leave a thin layer of material on the upside of the grid to prevent influence of bad optics on particles, and also to prevent further apertures through which additional heat load could travel.

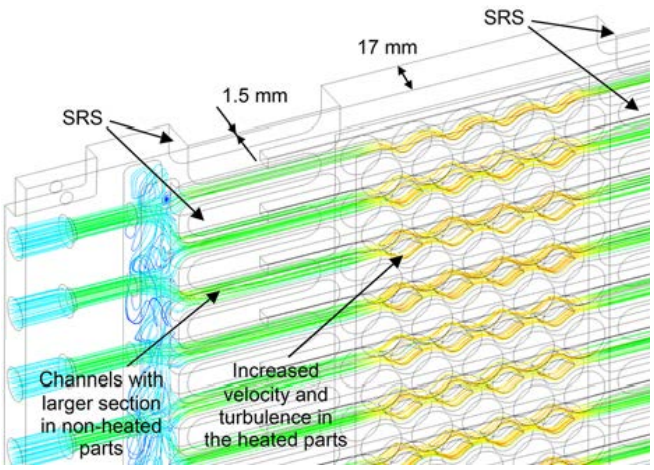

Figure 4.8: Application of Stress Relieving Slits on an NBI grid of MITICA. [20]

4.6 Cooling designs description

This section will describe the channel design choices made in this thesis, both based on the MITICA test-bed cooling channel design for the NBI accelerating grids as well as some other examples of improved geometries developed in previous R&D works, as mentioned in the introduction. Differently from how this kind of simulation has usually been carried up to now, through the usage of many discipline-specific codes and adapting each output into the next input, this paper will follow through the simulation effort all on a single, multi-purpose FEM code. This has its advantages mainly in ease of simulation and time, whereas losing in aspects of accuracy and convergence.
A good cooling channel design tends to approach the channel walls to the heat load footprint, to reduce the termal conducting resistance, and also increases the laminar heat transfer coefficient through the introduction of turbulence due to streamline curvature in the most critical areas. Another important aspect to be considered is keeping a high average hydraulic diameter, in order to limit pressure losses and make the channel system compatible with the pumping systems available. These aspect have led the designers to explore some distinct classes of possible solutions, reported as follows:

1. Single Straight Channels: these were the original cooling solution for the accelerating grids of the injector. Their strong points are the simplicity of construction and the low pressure drop that characterize each section, but its shape hardly follows the heat load footprint, leading to poor conduction of the deposited power and increase of temperature. It is still an interesting case for simulation, thanks to the possibility of comparing the experimental results with analytical formulas from literature.

2. Solutions increasing average wall surface by addition of sub-channels: to this family of solutions belongs the one currently adopted in the MITICA experiment, the Nozzle Island Cooling Enhancement (NICE) [20], as well as other more complex examples from the works of G. Gambetta [19]. In correspondence of where the heat load concentrates, these channels double and bend outwards, in order to better follow the footprint: the overall bend amplitude range from the 12 mm of the NICE solution to the 17 mm of the most driven designs. The solutions considered in this thesis are the NICE, the NICE Upgrade and Criss-Cross designs, a schematic of which is reported in figure 4.9.

3. Solutions increasing average wall surface by variation of the channel height: this family of solutions comprises both single or double channel designs, in which the increase in height to follow the heat load is compensated by a reduction in depth of the channel. The double channel design was suggested in order to increase the wall surface and reroute correctly the water flux towards the heated regions, at the cost though of higher pressure drops; both will be considered.

4. Solutions relying on additional turbulence injection: this family of designs is only reported as a special mention, but will not be simulated here, given their impact on computation time. On top of an existing cooling channel design, a special addition of small circular indentations, orthogonal to the water flow of about 0.25 mm radius can be applied, increasing the local turbulence and heat transfer coefficient. A similar example is the JET NBI hypervapotron design, able to withstand heat loads of 30 MW/m^{-2} (figure 4.10).

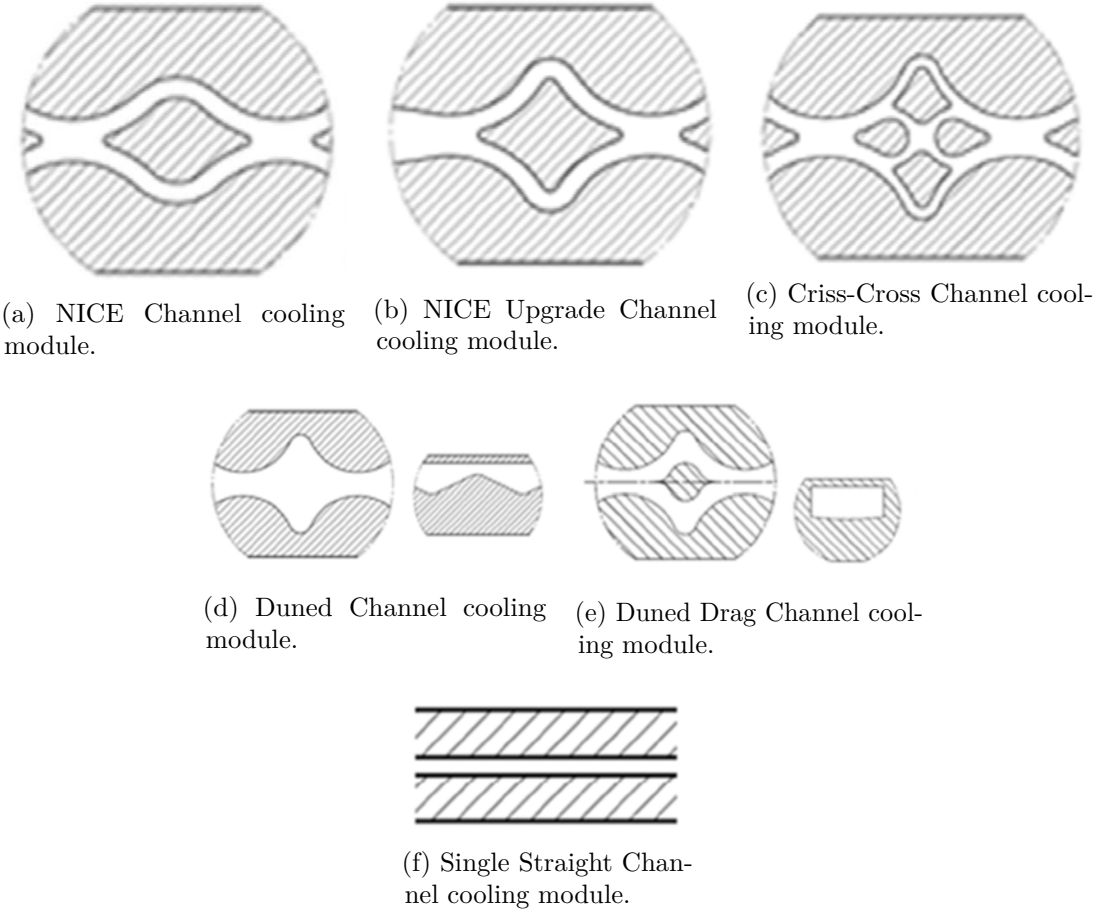

(a) NICE Channel cooling module.

(b) NICE Upgrade Channel cooling module.

(c) Criss-Cross Channel cooling module.

(d) Duned Channel cooling module.

(e) Duned Drag Channel cooling module.

(f) Single Straight Channel cooling module.

Figure 4.9: Conceptual designs considered for simulation.[19, 20]

It should be noted now that the pre-existent work of optimization on the channel geometries was carried out, similarly to how has been stated here, only onto the highest loaded grid; but in MITICA's case this role befell on a different grid than the Extraction Grid: this means that the same exact geometry cannot be used again without modification, due to the different space available and the flared shape of the beamlet aperture. Given this inconvenience, an effort on "translation" of the designs has been carried out, whose philosophy is reported:

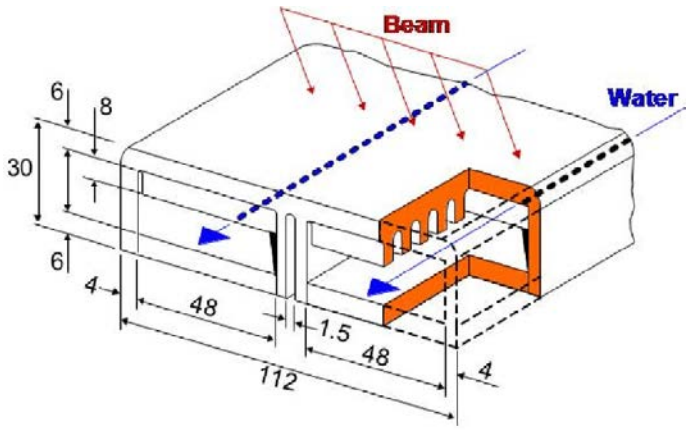

Figure 4.10: Example schematics of a JET hypervapotron section. The fins are evident in the figure, as well as their position.

- The total inlet channel size of 7 × 4 mm is respected, proper of the section dedicated to the cooling, but instead of horizontally the channel is set vertically, to respect the restrictions on minimum distances from other surfaces: this leads to a relative increase of the vertical size of the channels to maintain the volume flow constant.
- The total bend amplitude for each case is respected, since it is somehow the most important parameter to be taken into account when considering heat conduction and equivalent thermal resistance: this plus the previous point result though in smaller central island section, to allow reconnection of the two channels.
- The ratio between the inlet cross-section and the top-bend height of the channel is maintained, as well as the 1 mm fillet radius of the island blade towards the incoming flux of water; the other edges have been filleted as to reduce the pressure drop.

The resulting geometries closely resemble the ones reported in the papers, but are overall more lenient in terms of channel curvature, in order to face the problem of excessive pressure drop due to narrow channels. The profiles are reported in figure 4.11. After all of the inputs and boundary conditions are set, each model is solved for steady-state CFD and Heat Transfer.

4.7 Simulation results

The six designed cooling modules have thus been simulated, obtaining a number of important parameters, such as maximum temperature, pressure drop and max water velocity. The following bar plots report the most significant results (figures 4.12,

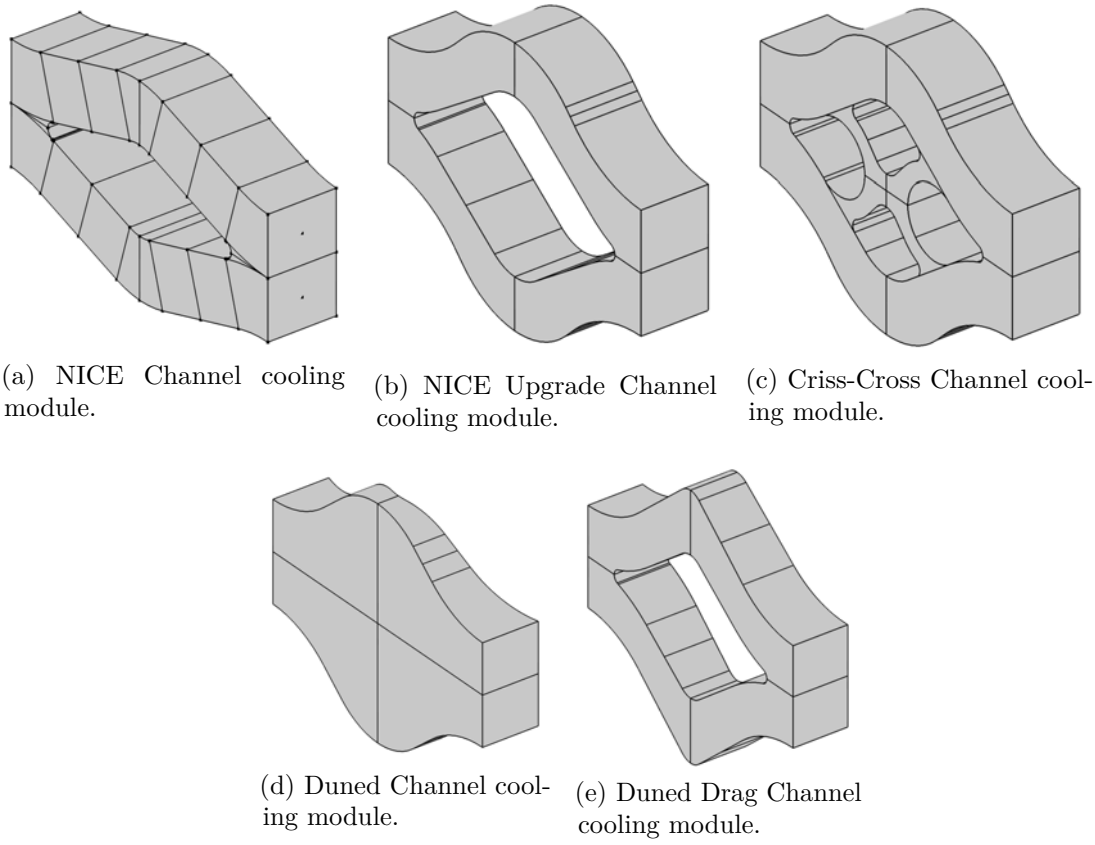

(a) NICE Channel cooling module.

(b) NICE Upgrade Channel cooling module.

(c) Criss-Cross Channel cooling module.

(d) Duned Channel cooling module.

(e) Duned Drag Channel cooling module.

Figure 4.11: Extraction Grid cooling designs adopted for simulation.

4.13, 4.14, 4.15). A table resuming the results is reported at tables 4.3, 4.4, 4.5, 4.6. To comment the results, it can be shown that the maximum pressure drop for each channel does not overcome the imposed limit of 0.35 bar per beamlet unit. This value is estimated starting from the specified limit of 6 bar over a single grid section and equally distributed between the 10 apertures, and then accounting for the additional due to the connection channels and the feeding and collecting manifolds at the sides of the grids, down to the value specified.
The temperature difference from model to model is not so relevant, and ranges in the tenths of degrees, with the straight channel performing the worst, as expected. Part of the reason for this behavior can be attributed to the extreme heat load condition, that whatever the cooling design, due to the limited space of where the exchange must take place, there is no real difference between each model, at most only equivalence if the channel has not some design faults. In any case the temperature, considered all the potential inaccuracies in obtaining the heat loads, does not seem to exceed the imposed limits. The notable difference stands in the water velocity, ranging from 9.5 to a maximum of 20 m/s, potentially influencing the erosion mechanisms on the fastest passages in the channel.

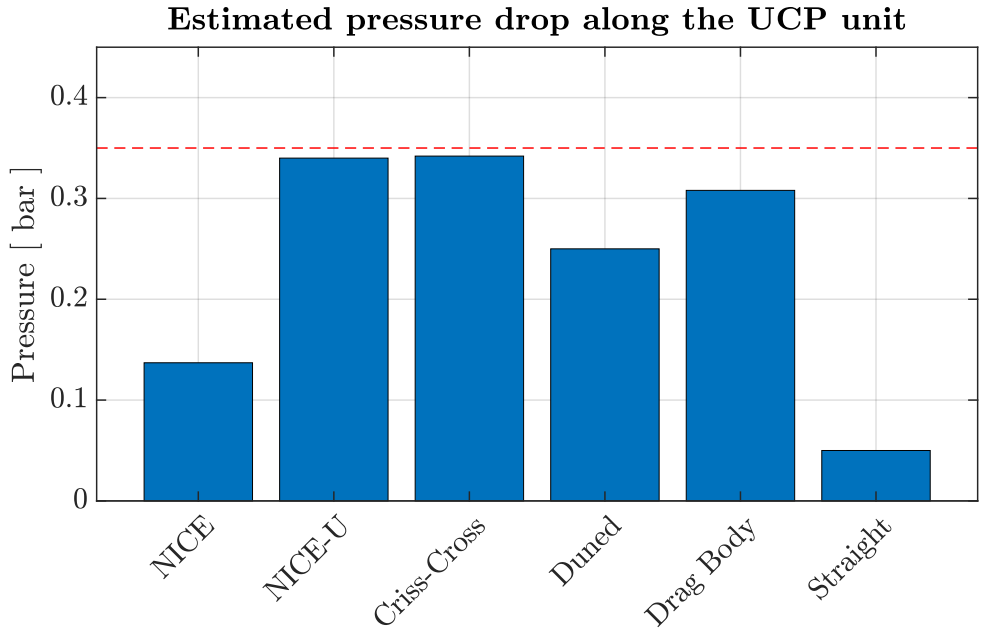

Figure 4.12: UCP pressure drop between inlet and outlet. The red dashed line indicates the maximum pressure drop allowed in a MITICA-like cooling circuit.

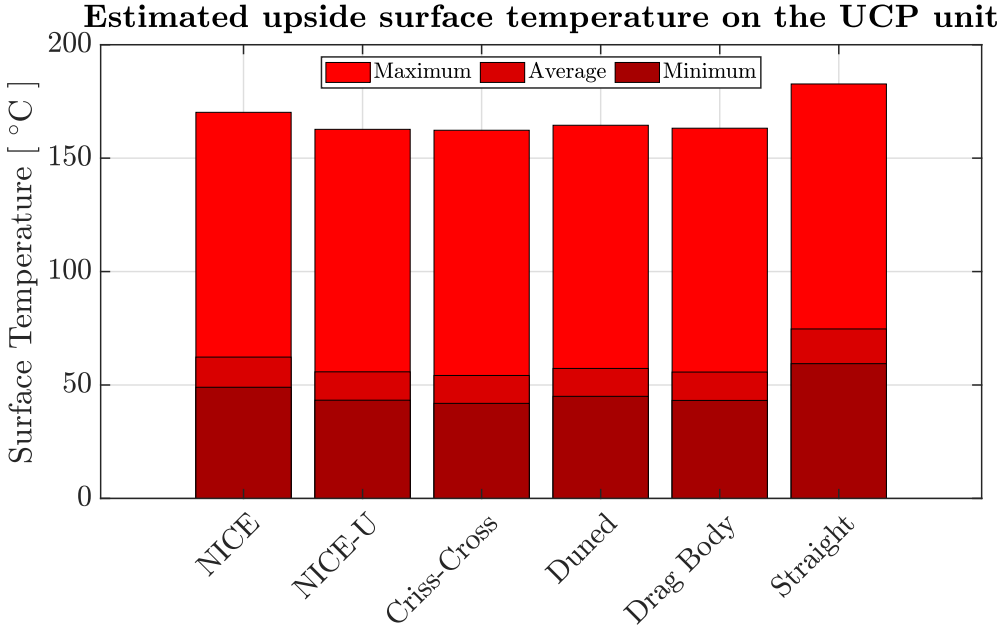

Figure 4.13: UCP surface temperature on the upstream side.

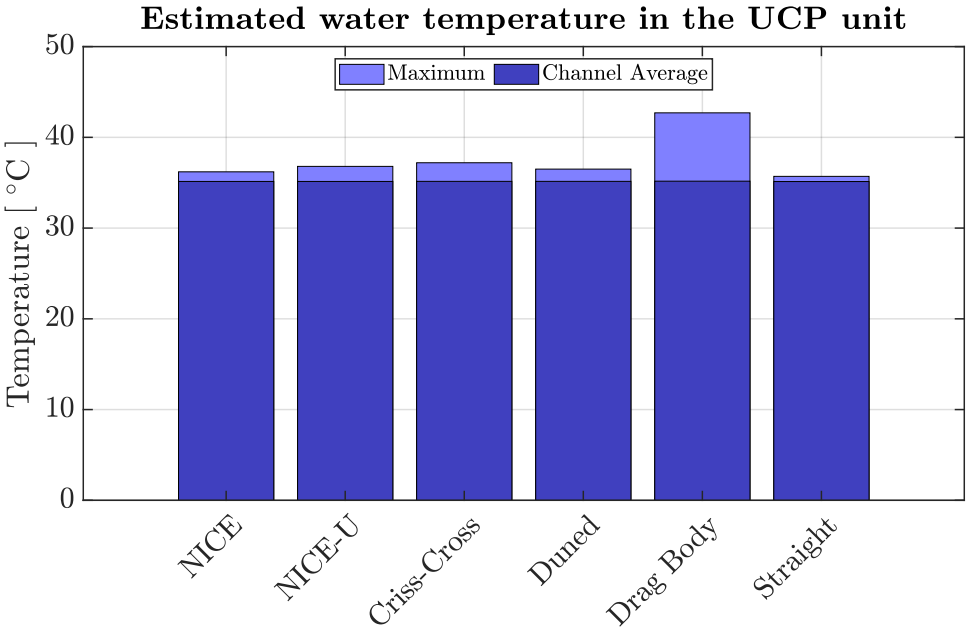

Figure 4.14: UCP water temperature inside the channel.

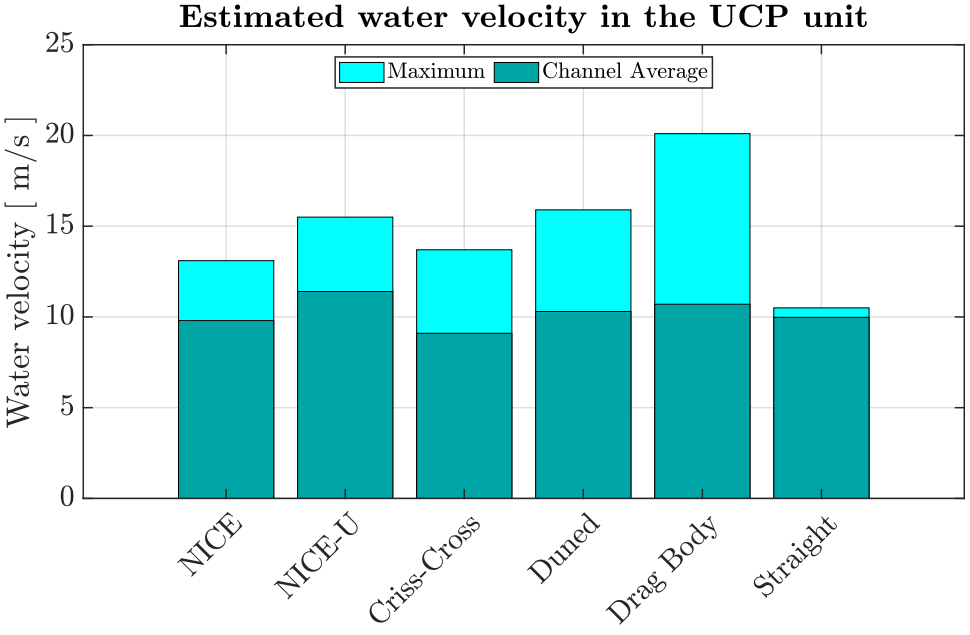

Figure 4.15: UCP water velocity inside the channel.

	Pressure [bar]
NICE	0.137
NICE - Upgrade	0.340
Criss - Cross	0.342
Duned	0.250
Duned Drag	0.308
Straight	0.050

Table 4.3: Results for the cooling modules on pressure drop.

	Max surf. T [°C]	**Avg surf. T [°C]**	**Min surf. T [°C]**
NICE	170.2	62.3	49.0
NICE - Upgrade	162.7	55.8	43.3
Criss - Cross	162.3	54.2	41.9
Duned	164.5	57.3	45.0
Duned Drag	163.2	55.7	43.2
Straight	182.7	74.7	59.4

Table 4.4: Results for the cooling modules on upside surface temperature.

	Max water T [°C]	**Avg water T [°C]**
NICE	36.2	35.14
NICE - Upgrade	36.8	35.14
Criss - Cross	37.2	35.15
Duned	36.5	35.15
Duned Drag	42.7	35.17
Straight	35.7	35.13

Table 4.5: Results for the cooling modules on water temperature.

	Max water velocity [m/s]	**Avg water velocity [m/s]**
NICE	13.1	9.8
NICE - Upgrade	15.5	11.4
Criss - Cross	13.7	9.1
Duned	15.9	10.3
Duned Drag	20.1	10.7
Straight	10.5	9.98

Table 4.6: Results for the cooling modules on water velocity.

Chapter 5

Optimizing design choices and applications

SUMMARY - The DTT NBI beam source, even if the present solutions already allow for the desired performances, due to the newly proposed possibility of obtaining the acceleration grids through additive manufacturing and different, less thermally performing materials, will have to improve its cooling channel system. This chapter is dedicated to the functional optimization work done in the thesis framework, in order to enhance as much as possible the cooling of the acceleration grids.

5.1 Introduction

The problem of cooling channel design is hardly untrodden: from when the need arose for high-performing embedded cooling in fusion technology, many efforts have been spent on the matter, each one proposing a different tweak on the geometry and optimizing the dimensions to the highest performance. The design proposals reported in the previous chapter, even in their original geometry, have already been extensively examined in dedicated research campaigns for MITICA, both numerically and experimentally; each of them yielded a solution that respected all of the pressure drop and temperature requirements, as well as the mechanical aspects of total stress, elongation and cycle life, prescribed in the SDC-IC regulation.
The difference with DTT is not only on the scale of NBI acceleration and power needed (hence the power to dissipate), but also on the continuous quest for economic convenience, especially in devices like this one, where special attention is paid to the overall budget (for a total 500 M€, according to the interim report [14]), and numerous proposal have surfaced in that merit, such as the possibility of additive manufacturing for the accelerating grids. The materials that can be processed in such a way though are still limited, as explained in the section before, and all with worse thermic characteristic than electrodeposited copper, so innovation is required

in order to increase the cooling. On a separate note, since this site is bound to be a cutting-edge example of how future reactors may be built and work, new ideas are always welcome if they manage to lower the performances needed from the auxiliary systems. In specific, speaking about the neutral beam source prospected to work in the DTT NBI unit, it will be designed by a dedicated team within Consorzio RFX, that already has many years of experience on the matter with experiments like SPIDER and MITICA, and also pre-conceptual works on DEMO NBIs.
This section is dedicated to functionally optimize the cooling aspect of the beam source, pursuing a double-faced solution pertaining the proposal of a combination of methods, a modified electron suppression system and new acceleration grid overall geometry and cooling channels. Since the most critical aspects of a cooling system of this kind are the temperature (from a mechanical point of view) and the pressure drop (from an hydraulic performance aspect), both separate aspects will be tackled with their respective addressed solution, then examined together. Unfortunately, this thesis does not cover any optimization routines for the work produced, but it will be a solid stepping stone for future improvements.

5.2 Slanted Grid design

This concepts constitutes a possible alternative to the already well-known and examined square grid array of apertures machined into the accelerating grids, being both simple to manufacture and fairly effective in ion extraction and co-extracted electron suppression, thanks to the dedicated magnets working effectively in strengthening each other and create an uniform field just before the aperture (figure 5.1).
One of their faults though that interests the case at first hand is how the heat load footprint distributes between apertures: following the directions of the field lines, it can be seen that the magnetic deflection field alternates upwards and downwards (the z direction) that combined with the charged particle velocity along the accelerator (traditionally, the x direction) in the Lorentz law results always in an alternating sideways deflection (along the y direction), in what is known as the Criss-Cross Deflection Effect (figure 5.2). This means that these particles impinge in the narrow space in between two apertures, and it is not easily accessible from the horizontal direction with cooling channels; this lead to the present designs, some of which have been simulated in this thesis, which try to approach as much as possible the heat load footprint without causing excessive pressure drop. The idea behind the Slanted Grid design lies within the intention of making these hot-spots accessible to channels running along the y direction by rotating each beamlet (deflection magnets included) increased in dimensions to a square of 22×22 mm by $45°$, and also modifying the array of beamlets to guarantee a solution both more compact and similar to the one actually available in both height, length and number of apertures.
This can be done by allowing alternating rows of N and $N-1$ apertures, as shown in figure 5.3: since the square geometry allows for 80 (5 by 16) apertures for total

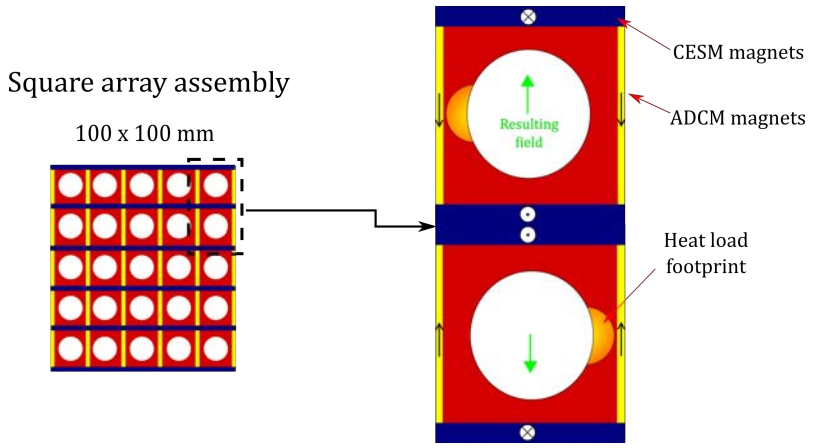

Figure 5.1: Figure reporting an example of a 5 by 5 square array; the configuration is similar to the pre-conceptual work on the DEMO NBI beam source [3] and the MITICA accelerator [20].

dimensions of 100 × 352 mm, a quick calculation for the rotated configuration yields that the best fit would have to be 12 rows of 4 beamlets alternated to 11 rows of 3, for a total of 81 for section and a maximum size of about 125 × 373 mm. Said array can be made compatible also with the existing grid support shapes by using the additional space left on the sides of each section, up to the total of 400 × 450 of typical grid module dimensions.
The advantages of such a configuration can be many:

- The heat loads are now accessible from the y direction with channels in a zone not as narrow as the space between two apertures, allowing for a more direct contact with the coolant fluid, potentially reducing the thermal resistance; they appear now "slanted", with respect to the horizontal edges.

- The magnetic configuration results virtually untouched with respect the square grid, only rotated, maintaining its strength.

- From the optics point of view, this configuration is more chaotic, but since the requirement on divergence at the exit of the accelerator is more critical in the horizontal direction (y), the rotation of the beamlet may decrease the previous value of offset of a factor $\sqrt{2}$ inferior.

- The alternated array of beamlets in combination of the rotation of the units create the perfect housing for channels that can completely embrace each separate beamlet and respect the grid requirements of minimum 1 mm space between surfaces, while filling the available space as much as possible.

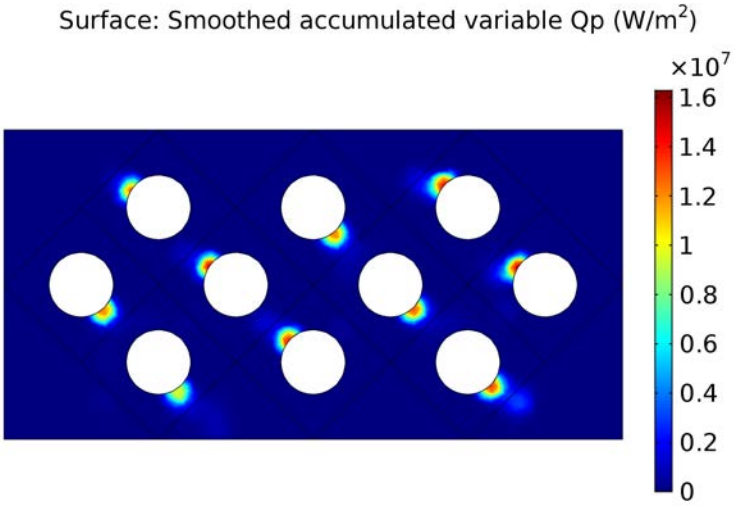

Figure 5.2: Example of Criss-Cross Deflection Effect. The heat loads follow the deflection imposed by the magnets, in an alternating fashion.

5.2.1 Enveloping Channels

The adoption of a slanted grid geometry as presented in the previous section allows for a very compact tiling of cooling channels inside the grids. By taking inspiration from the NICE concept, the nozzle island becomes where the aperture itself is located, "enveloping" completely the beamlet with its split channels and subject to the most direct heat load possible, directly under the surface. This peculiarity, combined with the alternating rows, allows for a channel to be largest when the others confining are smaller, and vice versa. A proof of concept UCP design can be appreciated in figure 5.4. As can be seen, the channels are still very large in every zone, even in the heated regions, leading to a potentially reduced cooling effect due to absence of increased turbulence (making it more akin to a straight channel than everything else). This is due only to the design being a proof-of-concept prototype, without excessive work in the hydrodynamics of the flow, in order to evaluate broadly the absence of basic mistakes and the magnitude of the interested parameters. Future developments could be focused around the increase of turbulence in the most critical zones through increasing curvature, reduction of channel height or insertion of hypervapotron-like devices. The simulation has been repeated with the same boundary conditions of the previous FEM verification of cooling channels to evaluate the performance and compare them to the other design choices available.

5.2.2 Simulation results

In order to accurately simulate the heat load generated in this configuration to account for border effects, a 3 by 3 beamlet model centered on the simulated one has been developed, and all the steps described in chapter 4 have been repeated.

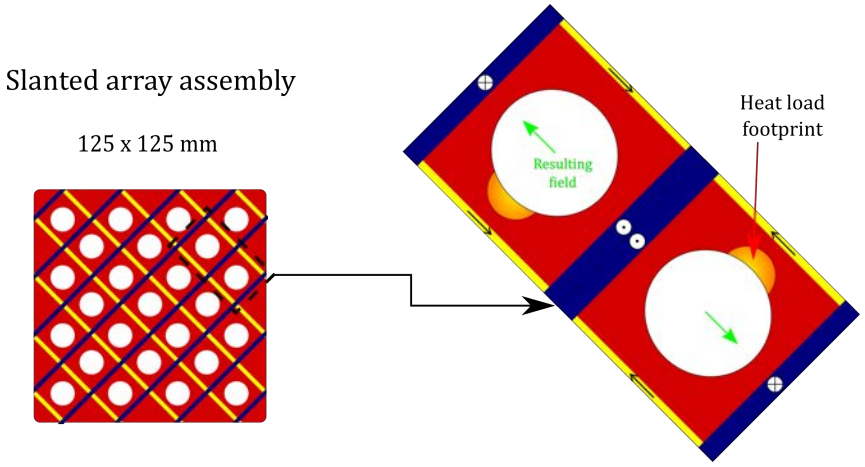

Figure 5.3: Example of a slanted grid configuration, in a 25-beamlet subset. The position of the magnets is reported, as well as the position of the heat footprint on single unit.

The heat load has then been applied to the corresponding UCP model, obtaining the results in table 5.1, where the performance is compared to the NICE-Upgrade concept results, similar in terms of curvature. The results are in line with those

Parameter	**Unit**	**Enveloped Ch.**	**NICE-U Ch.**
Pressure drop	[bar]	0.255	0.340
Maximum surface temp.	[°C]	177.9	162.7
Average surface temp.	[°C]	53.2	55.8
Minimum surface temp.	[°C]	38.1	43.3
Maximum water temp.	[°C]	37.2	36.8
Average water temp.	[°C]	35.16	35.14
Maximum water velocity	[m/s]	13.7	15.5
Average water velocity	[m/s]	10.0	11.4

Table 5.1: Table which sums up the results of the Enveloped Channel simulation, compared to the NICE-U solution.

obtained from similar geometries, mainly for average parameters. Difference arises in the pressure drop: the enveloped channel has a rather low hydraulic loss compared to the NICE-U solution, but has an higher surface temperature. Both of these values can be explained with the lack of increased turbulence in the former, whereas the latter shines. Even so, the cooling without any optimization is fairly solid and should deserve a better investigation on its geometry, under a more various range of working operations. For example, given the low pressure drop, it could be possible to increase the flow velocity to improve cooling, or as said previously, modifying the design to

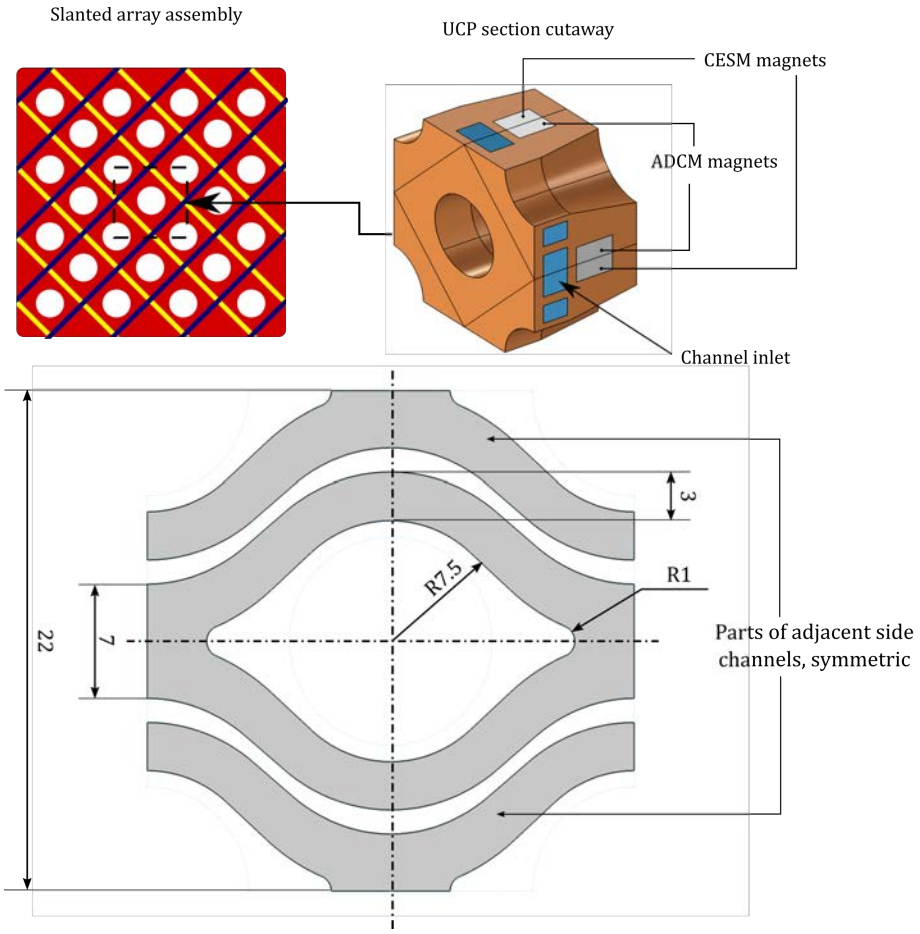

Figure 5.4: Extraction Grid cutaway, isolating the UCP and with a detail of the cooling channel geometry. As can be seen the inner channel is very close to the adjacent ones, ensuring the cooling.

create nozzles or swirls in the heated region.
This channel design may invite another important improvement: an increase in the maximum allowed pressure drop, due to the possibility of creating Single Channels along the grid with fewer Unit Channels. By taking a look at how earlier designs handle the connections between channels, it can be seen that for 5 plus 5 apertures, 4 plus 4 cooling units are needed in a straight channel, leading to the evaluated maximum drop limit of 0.35 bar; instead, due to how the enveloped channels are designed and to how the grid array is disposed, it is possible to cover 4 plus 3 apertures with 4 plus 3 cooling units, total seven instead of eight. In line of principle, this spared unit's worth of pressure drop can be redistributed among the others, increasing the value from 0.35 to $0.35 + 0.35/7 = 0.40$ bar. This increased limit can be either spent in more inlet velocity, increased turbulence or even in a less performing cooling system, to decrease expenses.

To close the section, a note on the possible flow paths: it could be possible to maintain a straight channel across the grid, similarly to how it has been done up to now (an example is shown in figure 4.8), with collecting manifolds at both sides; another solution would be to have both inlet and outlet on the same side of the grid, reducing the encumbrance of these channels between accelerating sections, shortening the connection channels, and making it possible to increase the cooling in specific parts without interesting the whole horizontal cutaway. An example for this possible configuration is reported in figure 5.5, also to better visualize the channel tiling and heat load footprint in the enveloped cooling/slanted grid.

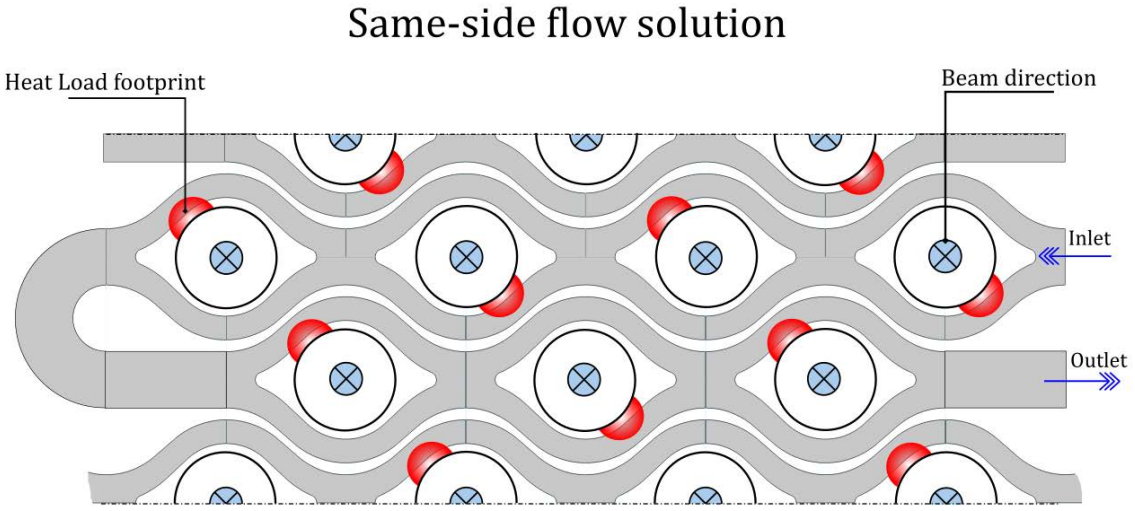

Figure 5.5: Conceptual design for cooling flow solution with both inlet and outlet on the same side.

5.3 ADCM-boosted deflection

For as much as the cooling effect of embedded channels can be optimized, increased and exploited, it is apparent that a limit of sorts shall be reached soon enough by those who research it, due to the limited size in which the heat exchange takes place. It also follows then that, other than following the cooling channel path, also the reduction of the heat load itself should be pursued. This thesis proposes a method based on the modification of the ADCM magnets role in the magnetic configuration on the Extraction Grid.
The magnetic configuration devoted to suppression of the co-extracted and secondary electrons has already been mentioned in previous chapters, as well as its function to generate a magnetic field as high as possible in the upstream section, and then somehow compensate for this field on the opposite side, in order to maintain the integral of **B** along x as small as possible and by consequence also the deflection felt

by the ion beam at the exit. The studies on this matter are numerous; to cite one there is the work on the pre-conceptual NBI beam source for DEMO [3], which set the optimal size for each magnet to obtain a close compensation of the ion deflection effect.
This is indeed a good innovation, able to compensate those 3.5 mrad of deflection and canceling its overall effect; but there is also to say that those deflection values are a small value with respect to those caused by space-charge repulsion of negative particles, and that a number of heavier correction systems have been devised (the kerb system [3] or the built-in deflector [21]). This may lead to the possibility of discard the role of ADCM magnets as a simple correction device, and instead use them to strengthen the upstream magnetic field: the modification will reduce the Larmor radius of electrons and ions, potentially making the former impinge on a far wider area, totally rebound them back into the Plasma Grid or even into the apertures themselves.
The only fact to take in account is to evaluate how much to change the ADCM size to obtain a satisfying deflection of the electrons while not deviating excessively the ion beam. In order to have a quick estimation, a select range of thicknesses will be considered, from 1 mm up to 4 mm; the same range explored in the DEMO NBI paper for correction of deflection purposes, since they have already been deemed worthy cases of analysis. Having fixed the range, two separate parametric optics simulations will then be run:

1. A co-extracted electron optics simulation, analogous to the ones made to obtain the heat load footprint and described in chapter 4: banally enough, there is the need to evaluate the impact of magnet thickness on heat load peak and total deposited power. Given the difference in magnitude, only the heat load from electrons is evaluated to simplify the procedure, without significant loss of meaning.

2. An ion beam optics simulation, devoted to trajectory and deflection calculation on a single beam model.

Between all of the cases there is the need to search for the one value of thickness that allows a great decrease of the deposited heat on the EG, without causing excessive distortion on the trajectory of the ions.

5.3.1 Co-extracted electrons simulation results

In order to be able to verify each heat load on the previously created UCP model, the heat load simulation is carried in the same 3 by 3 beamlet block. The result of the simulations is reported in table 5.2, and an useful visualization of the trajectories and the heat load can be appreciated in figures 5.6 and 5.8.

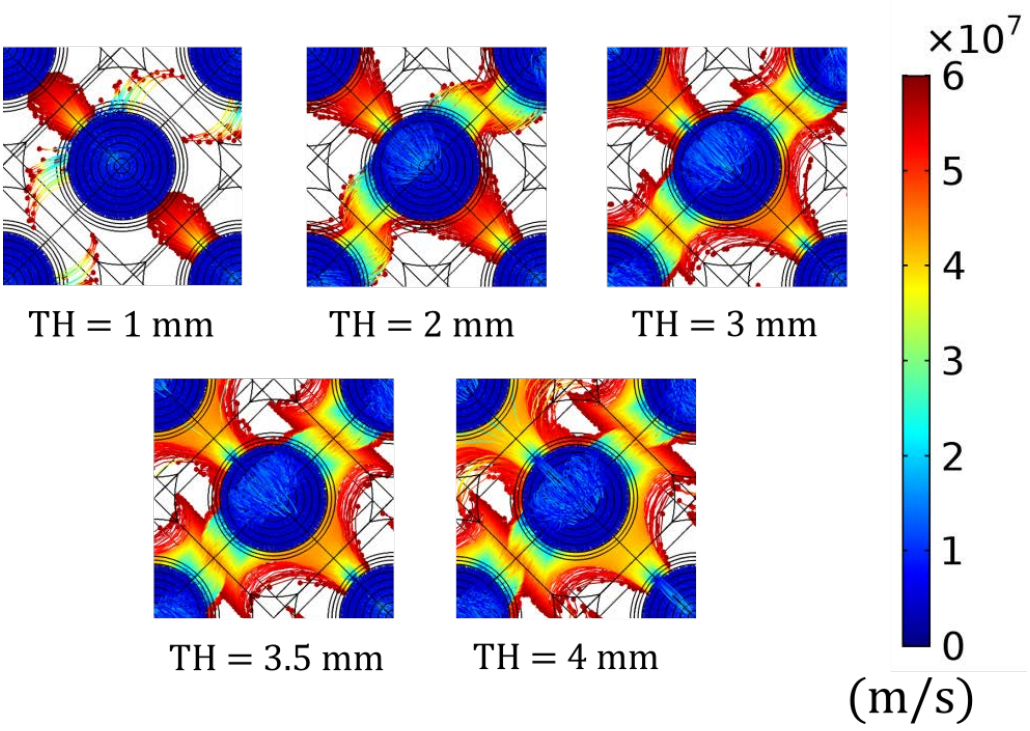

Figure 5.6: Particle trajectories for the various ADCM thicknesses. To note how the particle scatter more wide as the magnetic field strength increases.

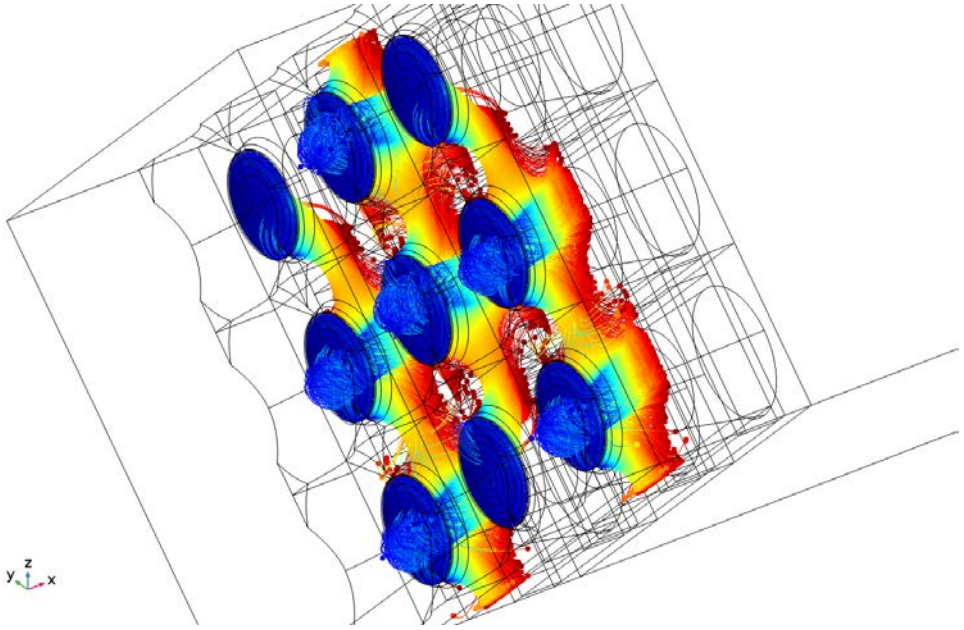

Figure 5.7: Isometric view of the co-extracted particle trajectories for TH = 4 mm.

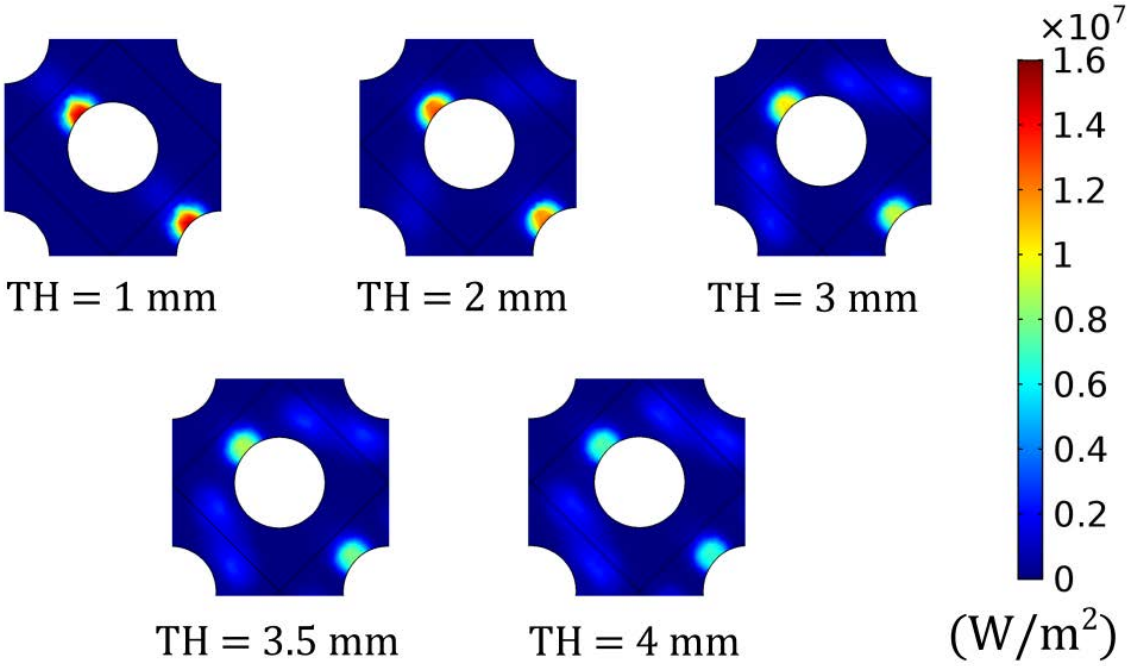

Figure 5.8: Heat load surface power for the various ADCM thicknesses.

ADCM TH	Peak density	Power/beamlet	Equiv. surface ratio
1 mm	15.5 MW/m^{-2}	402 W	0.92
2 mm	13.7 MW/m^{-2}	371 W	1
3 mm	11.2 MW/m^{-2}	329 W	1.13
3.5 mm	9.3 MW/m^{-2}	310 W	1.20
4 mm	7.5 MW/m^{-2}	294 W	1.26

Table 5.2: Table which sums up the results of the heat load simulation, in function of the ADCM thickness.

The solutions obtained are quite self-explanatory: as the thickness of the magnets increases, the electron disperse wider and with a more accentuated curvature, covering a far greater area and decreasing the peak loads considerably. Table 5.2 holds another interesting quantity, the equivalent surface ratio, obtained as the power per beamlet divided by the reference solution value (in this case, the 2 mm ADCM): since the power input is the same, this quantity can be visualized as how much the impact area seen by the incident particles increases as they scatter. The area appears to increase almost linearly with the magnet thickness; and heat load peaks appear almost halved with respect to the reference solution, leading to most favorable thermal working conditions.

5.3.2 Ion beam optics simulation

The aim of this simulation is not of heat load estimation but purely optical and limited to the effect that the ADCM magnets have on the negative ion beam. To this end a single beamlet model is sufficient, where the magnet thickness is parameterized; successively the data on trajectory can be exported and analyzed to obtain data on average trajectory and deflection. Since the system is indifferent to rotation, the module has been kept horizontal, to simplify the post-processing calculation; in fact, with this hypothesis the exit deflection can be obtained as:

$$\theta_{yz} = \frac{\sum_i^n \arctan \frac{v_{y,i}}{v_{z,i}}}{n} \tag{5.1}$$

where $v_{y,i}$ and $v_{z,i}$ are the velocity components of the i-th particle in the plane orthogonal to the direction of acceleration, and mediated over the n particles used in the simulation. In a similar fashion the positions of each particle can be mediated for every instant of the time-dependent analysis, obtaining the average trajectory of the beam.
The model used and the solutions obtained are reported in figure 5.9, with the total deflections copied into table 5.3 for easier consultation. The obtained results are

ADCM TH	**Exit deflection [mrad]**
1 mm	-1.27
2 mm	0.66
3 mm	1.86
3.5 mm	2.53
4 mm	3.75

Table 5.3: Table which sums up the results of the ion optics simulation, in function of the ADCM thickness. A negative value means an under-compensation of the CCDE phenomenon, where the ion beam stays deflected as in the no-ADCM case.

in perfect accord with the analysis performed for the pre-conceptual DEMO NBI beam source, confirming the ideal value of 2 mm ADCM thickness for good deflection compensation (equal to the choice made in the other papers), while other values stack up to a maximum of 3.75 mrad. This value is relatively high, but still smaller than the deflections caused by ill-focused electrostatic lenses and particle space-charge, that given the inferior acceleration voltage with respect to DEMO and consequently shorter accelerator, are bound to be inferior too. To conclude, the idea of using ADCM to strengthen the upside magnetic field still needs extensive validation in terms of optics, but should definitely be kept into consideration as a device to lighten the heat loads especially on the Extraction Grid.

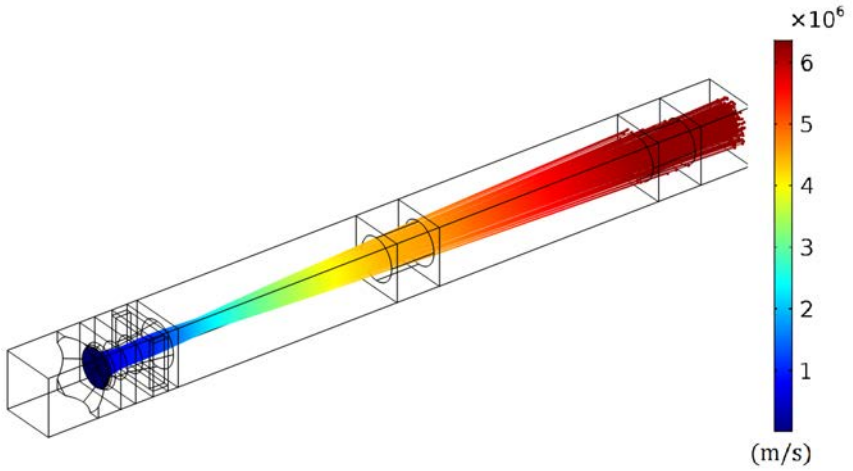

(a) Particle tracing solution; velocity map of the ion particles.

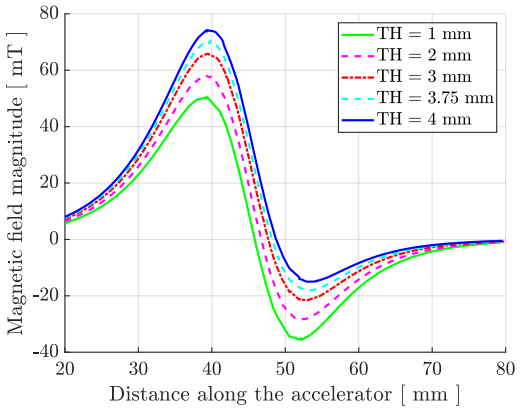

(b) Magnetic field intensity at the center.

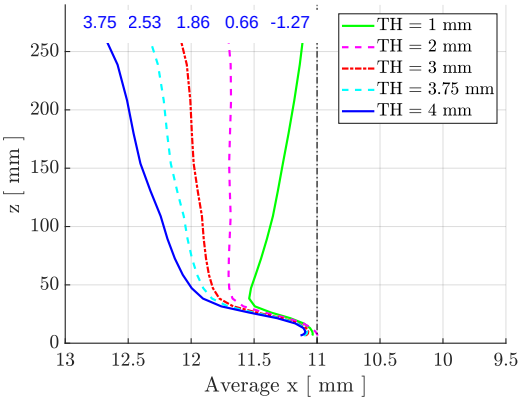

(c) Deflection map for the parametric simulation.

Figure 5.9: Parametric simulation for ion optics. The numbers in blue report the beamlet deflection at the exit in mrad.

5.4 Application on the copper cooling module

After analyzing separately each possible enhancement for the Extraction Grid thermic behavior, it is interesting to combine them to ascertain their effectiveness with respect to the other solutions obtained with more orthodox approaches. For the final analysis an UCP unit has been adopted with the Slanted Grid design and the Enveloping Channels concepts for the mechanic and thermo-hydraulic point of view, whereas for the input heat load the 4 mm thickness ADCM case has been chosen, to portray the best possible situation available, putting secondary optics issues aside for the moment. The analysis has been carried thus with the same procedure as described in chapter 4; results are reported both visually in figure 5.10 and in tabled format (table 5.4). The solution obtained is very interesting: aside from the hydraulic quantities

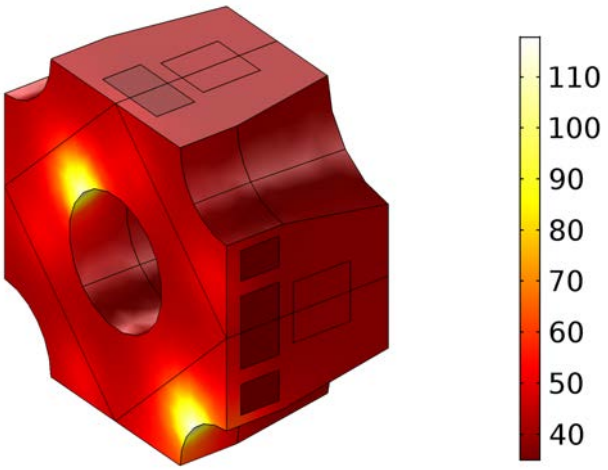

(a) Temperature map of the UCP unit (°C).

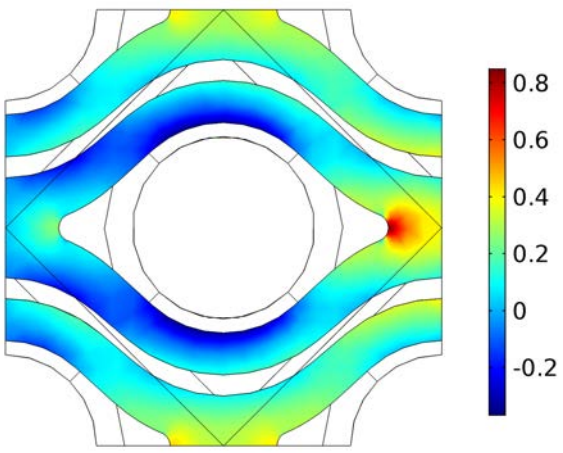

(b) Pressure map in the water volume (bar).

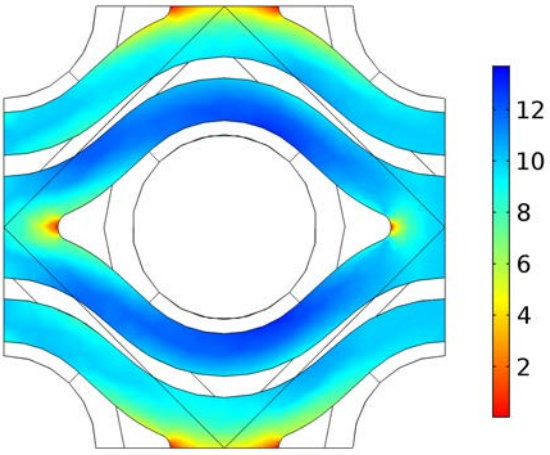

(c) Velocity magnitude in the water volume (m/s).

Figure 5.10: Thermo-hydraulic simulation for enhanced cooling solutions.

that have not been interested by change since the introduction of the Enveloping Channels, key parameters like the peak upside surface temperature is fairly decreased (about 50 °C), due to the heavy scattering action of the boosted ADCM magnets and the resulting reduced heat load. This result, even admitting all of the possible detriments of such a design (complexity, increased particle chaos, heavier correction, etc.), is extremely interesting, especially in vision of more economic NBI assemblies and/or less thermally performing materials, given how a small modification in the magnetic system could lead to this degree of performance. Still, many other problems may be lurking beneath the simple models built for the thesis, and may surface only during manufacturing or testing of prototypes, and also the numeric values may be subject to variation once transposed into reality; this is all the more reason to keep up the numeric effort in future works and obtain a definitive answer.

Parameter	Unit	Value
Pressure	[bar]	0.255
Max. surf. temperature	[°C]	114.0
Avg. surf. temperature	[°C]	49.7
Min. surf. temperature	[°C]	40.6
Max. water temperature	[°C]	36.4
Avg. water temperature	[°C]	35.12
Max. water velocity	[m/s]	13.7
Avg. water velocity	[m/s]	10.0

Table 5.4: Key parameters obtained in the simulation for enhanced cooling solutions.

5.5 Application on the printed cooling module

This last section is dedicated to the application of the previous enhancements to the more interesting case for DTT, the printed bronze grid that is being researched as a cheaper alternative to the electrodeposited copper grid. The objective is still to obtain temperatures lower than 300 °C, but this time with a material that has a far lower thermal conductivity, as shown in section 3.3.3. The material chosen for this last set of analyses is the $CuNi_2SiCr$ printed bronze, for its relatively high conductivity (1/5 of pure copper, instead of 1/20 for the $CuSn_{10}$ bronze).
However, there is no guarantee that the simple application of the enhancements will be enough to grant the desired temperature, so there is the need to have some parameters (namely some boundary conditions or geometry) change accordingly. The choice has fallen on the thickness between channel and grid surfaces (1.5 mm in the nominal case), that at this early point in development could be reduced up to 0.5 mm, as long as the thickness is verified to be sufficient to contain the pressure without excessive deformation; secondly the inlet velocity can be increased up to around 2 times the nominal value of 10 m/s, hypothesizing future cooling systems able to guarantee pressure drops of even tens of bar, instead of the 6 bar of current devices, and ignoring for the moment the possibility of material erosion due to speed. The two modifications will be applied together in a rough parametric sweep, devoted to sense how the cooling is affected by their combination and to provide an indication of the direction to take in future analyses for 3D-printed acceleration grids for DTT.

5.5.1 Parametric simulation results

As explained before, the parametric simulation considered as variables the distance of cooling channels from the surface and the inlet velocity for the channel, under the usage of a multiplying parameter n over the nominal value of 10 m/s. The value of thermic conductivity for the appointed printed bronze ranges around 84.56 W m^{-1} K^{-1}, with similar structural characteristics with respect to copper. Table 5.5 contains

the various combinations of the control parameters, complete with the respective temperature and pressure drop results obtained for each.

n \ d	1.5 mm	1 mm	0.5 mm
1	321.6 °C 0.260 bar	316.0 °C 0.254 bar	312.6 °C 0.240 bar
1.5	304.1 °C 0.582 bar	294.1 °C 0.571 bar	284.7 °C 0.538 bar
2	293.1 °C 1.04 bar	280.3 °C 1.02 bar	267.4 °C 0.963 bar
2.5	285.3 °C 1.64 bar	270.6 °C 1.61 bar	255.2 °C 1.52 bar

Table 5.5: Key values obtained in the parametric simulation for enhanced cooling in the printed bronze UCP.

The results of this analysis are fairly interesting:

- Considering the nominal speed and only translating the cooling channels (first row of the table), the temperature seems to decrease rather slowly even pushing to the limit of 0.5 mm of thickness: this is probably due to a mismatch between incoming power flow and coolant fluid velocity, that results to be too reduced in these first configurations to promptly remove heat and reduce effectively the surface temperature. This statement can be verified in the successive analyses at higher coolant velocities, that in relation to the nominal 1.5 mm depth manifest a steeper decrease in temperature as the channels are closer to the surface.

- Another behavior that can be observed is that, by getting closer the cooling channels to the surface, thus increasing the temperature of the coolant in the channels, the pressure drop appears to decrease: this is linked to the local reduction of density in the part of the channel that is more heated, that results in an overall inferior pressure difference.

- Considering instead the variation of the parameter n, it is easy to see that its influence is greater in terms of temperature decrease than the modification of surface depth, but comes at the cost of higher pressure drops: strictly speaking, pressure drop increases roughly with the square of the velocity. Imagining a future cooling system able to supply at inlet a difference of 10 bar, for each UCP in the enveloped configuration could be spared a total of about 1.40 bar each; this fact suggest a maximum for the parameter n of about 2 to not exceed said value.

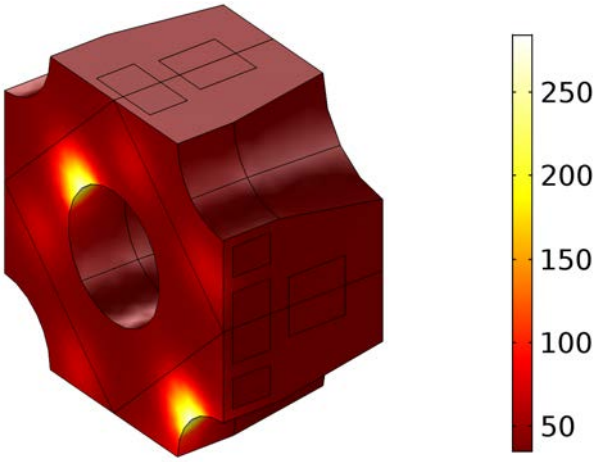

(a) Temperature map of the bronze UCP unit (°C).

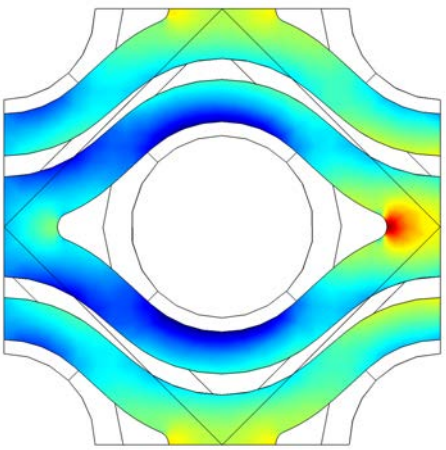

(b) Pressure map in the water volume (bar).

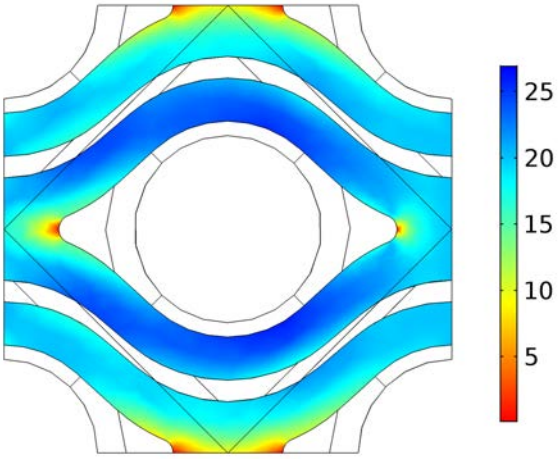

(c) Velocity magnitude in the water volume (m/s).

Figure 5.11: Thermo-hydraulic simulation for one of the printed bronze enhanced cooling solutions: $d = 1$ mm and $n = 2$.

The good news is the possibility of reaching temperatures lower than the 300 °C even in these unfavorable material and working conditions through the use of the enhancements previously described and parameter modification: for example, considering a 1 mm depth and a 20 m/s inlet velocity, the temperature ranges in the 280 °C and around the 1 bar of pressure drop per each UCP unit, 7 bar total, in a not so unreasonable upgrade from the actual systems. This is a very interesting result for a future application of additive manufacturing in NBIs for DTT, since it shows that under definite conditions the thermic requirements can be respected even in the worst of operative situations.

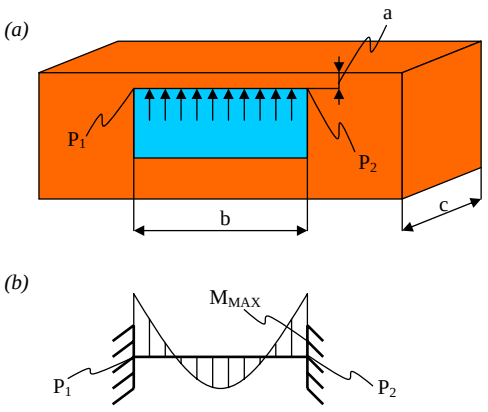

Figure 5.12: Simplified model to calculate the stress due to the water pressure: (a) Main dimensions and critical points; (b) Bending moment along the bronze layer.

5.5.2 Channels deformation verification

The decision of reducing the depth of the channels come at the cost of the increased possibility for excessive deformation of the grid surface due to the pressure of the coolant inside the channels. A simple solid mechanics simulation can be carried out to roughly evaluate the deformation caused by the system internal pressure load.
From an analytical point of view, the maximum stress on the bronze layer is approximately proportional to the square of the channel width, as can be seen from the simplified model in figure 5.12. The maximum bending moment and bending stress can be evaluated from the internal pressure and the geometrical parameters:

$$M_{MAX} = p \cdot c \cdot \frac{b^2}{12} \tag{5.2}$$

$$\sigma_{MAX} = \frac{M_{MAX}}{J} \cdot \frac{a}{2} = \frac{p \cdot c \cdot \frac{b^2}{12}}{\frac{1}{12} \cdot a^3 \cdot c} \cdot \frac{a}{2} = \frac{1}{2} \cdot \frac{p \cdot b^2}{a^2} \tag{5.3}$$

where p is the pressure inside the tube, a is the bronze layer that covers the tube, b is the tube width, c is the tube length, M_{MAX} is the maximum momentum due to the internal pressure, σ_{MAX} is the maximum stress due to the internal pressure and J is the area moment of inertia. This formula describes how wider channels are expected to have greater stresses, as well as the influence of the bronze layer.
These parameters are directly linked to the overall deformation strain observed on the loaded object: in this case, for the sake of simplicity, 20 bar of pressure will be applied equally on every surface of the channel, without accounting the contribution given by the CFD module. This value roughly represents the average value of pressure at which the NBI cooling systems usually work and can be used to determine the deformation of the channels at the variation of the parameter a.
As for the boundary specifications, a zero displacement condition has been placed

on all the sides, restraining the displacement in a not realistic way on the borders, but rather accurately in the center. Figure 5.13 shows the results of the parametric analysis carried out for this verification. The results mirror somewhat accurately

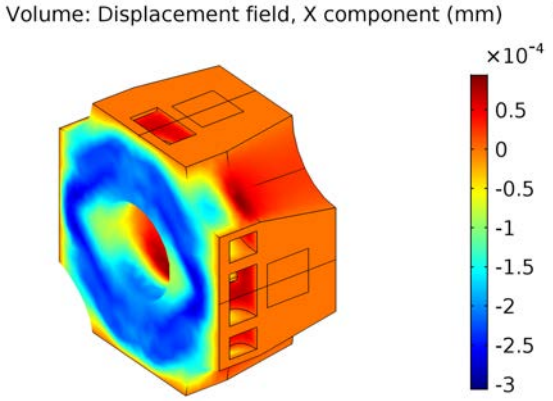

(a) Result with $a = 1.5$ mm.

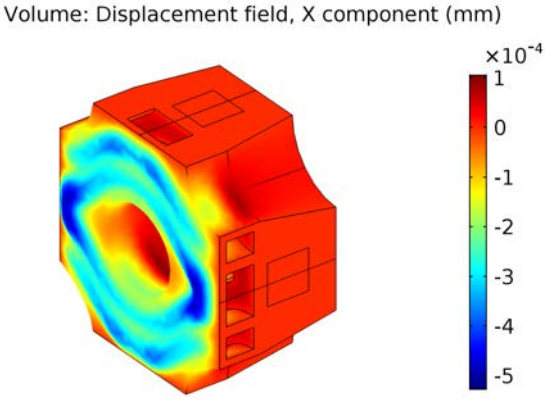

(b) Result with $a = 1$ mm.

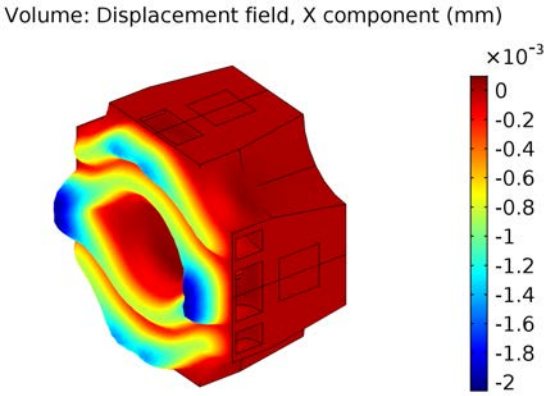

(c) Result with $a = 0.5$ mm.

Figure 5.13: Solid Mechanics simulation for one of the printed bronze channels, at the variation of bronze layer thickness a.

the behavior expected from the various models: the x-component of the strain (the most evident of the three) increases with the decrease of the bronze layer; also the deformation is more visible where the channels split to embrace the aperture, since they are there wider.
These deformations are rather small, but what must also be considered is the stress σ, that can be quite elevated in the corners and angles of the configurations (i.e. especially where the channels split) and easily reach even about half of the yield strength of the material. This may not cause immediate rupture of the bronze layer, but could cause a shorter cycle life due to fatigue; it is important then to leave enough material layer to lower this type of load and guarantee a longer life to the component.

Chapter 6

Conclusion

In this thesis, starting from specifics of geometry and boundary conditions proper of past works done in the field of Neutral Beam Injector simulation and experimentation, a DTT-like NBI system has been modeled in the COMSOL® environment.
In particular, a novel procedure to evaluate thermal loads in the accelerator has been proposed, using cross-section curves, particle tracing and wall-linked accumulated variables, contained all included in the COMSOL code; the results obtained being close to those evaluated through other methods.
This procedure has then been the input for a thermic analysis of the grids, from which evaluate the temperature field obtained in different cooling conditions and geometries inspired by other research efforts on the matter. Key parameters like pressure drop and water velocity have then been evaluated for comparison.
Finally, some new proposals have seen the light, such as the Slanted Grid design, where the square array symmetry is exchanged for a 45 °one; the Enveloping Channels, able to completely embrace each beamlet aperture and reduce the distance from applied heat loads; and the ADCM-boosted deflection, where some magnetic components have been re-imagined to help in decreasing the deposited power density. Each has been analyzed numerically and then applied together in a theoretical grid section, obtaining a potential significant increase in performance from both the maximum temperature and pressure drop point of view. To top it off, the enhanced configurations have been applied to the case of the printed $CuNi_2SiCr$ bronze, one of the materials under investigation for possible use for the acceleration grids in DTT NBI, showing the possibility to obtain temperatures lower than 300 °C even with reduced thermal conductivity.
The possible followup analysis are almost endless: from continuing the optimization effort on the geometry for the cooling channels, to analyze the complex resulting optics of a Slanted Grid and devising a correction device strong enough to keep deflection in check, continuing to the enhancement of the heat load modeling, obtaining smoother and comprehensive power density maps to apply; without even mentioning the whole mechanical stress and strain evaluation, that constitutes a problem in itself.
For now, this thesis should provide enough food for thought on the matter of thermo-

hydraulic design of acceleration grid's embedded cooling channels, as well as further investigation into the use of the versatile COMSOL environment in more and more simulation projects, thanks to its most recent additions that made these kind of analysis possible.
There is also the hope that somewhere in this thesis some concept could help other researchers and myself in my future career in the field, all in order to bring humanity a little step closer to make fusion reality.

Chapter 7

Acknowledgements

For this short thesis, I would like to give a great thanks instead to Eng. Piero Agostinetti, always present and willing to put up with my slowness and behavior, even reading the draft of this very paper during its vacation: I am in great luck to have him as supervisor, and all the guided visits around the Consorzio RFX only increased my interest in matters of fusion.
Next, I would like to thank deeply prof. Piergiorgio Sonato, for giving me the opportunity to double down on the experience of writing my own thesis in a stimulating place such as the Consorzio, and also for the extremely interesting notions taught in its Industrial Plasma Applications course during the Master's Degree, that at some time in my life I would hope to get back to and possibly master (MHD planes, I am looking at you). Together with the professor I thank also all of the patient and helpful people that I met at the RFX, supplying me with material to work on.
Last but not least, my thanks goes to prof. Paolo Bettini, who held the Thermonuclear Fusion course at the Master's Degree: even if not at all exhaustive, the lessons have been eye-opening nonetheless on the matter; also his availability for helping those who wanted to get into the Ph.D. has been precious.
I hope to carry on at least a fraction of what you taught me into my next, new experience as a Ph.D. student, and to treasure what experiences I had. Here is to the future!

Bibliography

[1] *BP Statistical Review of World Energy.* 68th Edition (2019).

[2] Kikuchi M., Lackner K., Tran M. Q. *Fusion Physics.* International Atomic Energy Agency, Vienna (2012).

[3] P. Sonato, et al. *Conceptual design of the beam source for the DEMO Neutral Beam Injectors.* New J. Phys. 18 (2016) 125002.

[4] J. Pamela. *The physics of production, acceleration and neutralization of large negative ion beams.* Plasma Phys. Control. Fusion 37 (1995) 325-336.

[5] R.S. Hemsworth, D. Boilson, H.P.L. de Esch, A. Krylov, P. Massmann and L. Svensson. *Some lessons from long pulse operation of negative ion sources and accelerators.* Nucl. Fusion 46 (2006) 239-249.

[6] M. Hanada, M. Kashiwagi, T. Inoue, K. Watanabe, and T. Imai. *Experimental comparison between plasma and gas neutralization of high-energy negative ion beams.* Rev. Sci. Inst. 75 (2004) 1813-1815.

[7] Y. Ikeda, N. Umeda, N. Akino, N. Ebisawa, L.Grisham, M. Hanada, A. Honda, T. Inoue, M. Kawai, M. Kazawa, K. Kikuchi, M. Komata, K. Mogaki, K. Noto, F. Okano, T. Ohga, K. Oshima, T. Takenouchi, Y. Tanai, K. Usui, H. Yamazaki and T. Yamamoto. *Present status of the negative ion based NBI system for long pulse operation on JT-60U.* Nucl. Fusion 46 (2006) 211-219.

[8] W. Kraus, P. McNeely, P. Franzen, A. Entscheva, M. Bandyopadhyay, B. Heinemann, R. Riedl, E. Speth and R. Wilhelm. *Development of large RF driven negative ion sources for neutral beam injection.* Fusion Eng. Des. 66-68 (2003) 491-495.

[9] H. P. L. de Esch. *TW4-THHN-IITF2 Final Report - Deliverable 3.1.4.4 Electrons in SINGAP.* EFDA report (2006).

[10] A. Simonin, J. Bucalossi, C. Desgranges, M. Fumelli, P. Massmann and J. Pamela. *Cadarache, 1 MeV negative ion accelerator development for application in thermonuclear fusion research.* Proceedings of the Particle Accelerator Conference, 1997.

[11] H.P.L. de Esch, R.S. Hemsworth and P. Massmann. *SINGAP: the European concept for negative ion acceleration in the ITER neutral injectors.* Rev. Sci. Inst. 73 (2002) 1045.

[12] Barnett C. F. *Collisions of H, H_2, He, and Li atoms and ions with atoms and molecules.* Technical Report No. ORNL-6086, Oak Ridge National Laboratory (1990).

[13] F. Romanelli et al. *Fusion electricity - a roadmap to the realization of fusion energy (EFDA).* http://eurofusion.org/wpcms/wp-content/uploads/2013/01/JG12.356-web.pdf (2012)

[14] R. Albanese and F. Crisanti et al. *Divertor Tokamak Test facility Interim Design Report.* ENEA, ISBN: 978-88-8286-378-4 (2019).

[15] A. Kojima et al. *Progress in long-pulse production of powerful negative ion beams for JT-60SA and ITER.* Nucl. Fusion 55 (2015) 063006.

[16] B. Heinemann et al. *Latest achievements of the negative ion beam test facility ELISE.* Fusion Eng. Des. (2018), Fusion Eng. Des., 136 (2018) 569.

[17] P. Agostinetti, et al. *Manufacturing and testing of grid prototypes for the ITER neutral beam injectors.* IEEE Trans. Plasma Sci. 42 (2014) 628.

[18] L. Murr et al. *Metal Fabrication by Additive Manufacturing Using Laser and Electron Beam Melting Technologies.* Journal of Materials Science and Technology -Shenyang- (2012).

[19] G. Gambetta. *Development, optimization and testing of high performance cooling systems for fusion devices.* Università degli Studi di Padova (CRF), XXX Ph.D. cycle (2015).

[20] P. Agostinetti, et al. *Detailed design optimization of the MITICA negative ion accelerator in view of the ITER NBI.* Nucl. Fusion 56 (2016) 016015.

[21] F. Veronese. *Functional optimization of the electrostatic accelerator for the DEMO neutral beam injector.* Università degli Studi di Padova, Bachelor Thesis (2017).

CONSORZIO RFX

Ricerca Formazione Innovazione

UNIVERSITÀ DEGLI STUDI DI PADOVA

Dipartimento di Ingegneria Industriale

Corso di Laurea Magistrale in Ingegneria dell'Energia Elettrica

TESI DI LAUREA MAGISTRALE IN
INGEGNERIA DELL'ENERGIA ELETTRICA

Multiparametric optimization of DTT NBI beam source

RELATORE: Prof. Piergiorgio Sonato

CORRELATORE: Dott. Ing. Piero Agostinetti
(Consorzio RFX)

LAUREANDO: Fabio Veronese

ANNO ACCADEMICO 2018-19